CONSTITUTIVE MODELING OF ALUMINUM FOAM AND FINITE ELEMENT IMPLEMENTATION FOR CRASH SIMULATIONS

by

Jing Bi

A dissertation submitted to the faculty of
The University of North Carolina at Charlotte
in partial fulfillment of the requirements
for the degree of Doctor of Philosophy in
Mechanical Engineering

Charlotte

2012

Approved by:

_____
Dr. Howie Fang

_____
Dr. Ronald E. Smelser

_____
Dr. Harish P. Cherukuri

_____
Dr. David C. Weggel

_____
Dr. Russell G. Keanini

_____
Dr. Don Chen

ABSTRACT

JING BI. Constitutive modeling of aluminum foam and finite element implementation for crash simulations. (Under the direction of DR. HOWIE FANG)

In the past decades metallic foams have been increasingly used as filler materials in crashworthiness applications due to their relatively low cost and high capacity of energy absorption. Due to the destructive nature of crashes, studies on the performance of metallic foams using physical testing have been limited to examining the crushing force histories and/or folding patterns that are insufficient for crashworthiness designs. For this reason, numerical simulations, particularly nonlinear finite element (FE) analyses, play an important role in designing crashworthy foam-filled structures. An effective and numerically stable model is needed for modeling metallic foams that are porous and encounter large nonlinear deformations in crashes.

In this study a new constitutive model for metallic foams is developed to overcome the deficiency of existing models in commercial FE codes such as LS-DYNA. The new constitutive model accounts for volume changes under hydrostatic compression and combines the hydrostatic pressure and von Mises stress into one yield function. The change of the compressibility of the metallic foam is handled in the constitutive model by allowing for shape changes of the yield surface in the hydrostatic pressure-von Mises stress space. The backward Euler method is adopted to integrate the constitutive equations to achieve numerical accuracy and stability. The new foam model is verified and validated by existing experimental data before used in FE simulations of crushing of foam-filled columns that have square and hexagonal cross-sections.

ACKNOWLEDGEMENTS

I am grateful to many people who helped, supported and guided me in the development of this dissertation and throughout my five years at UNC Charlotte. Their words of inspiration and encouragement gave me the determination to fulfill my research goals.

I would like to thank my graduate advisor, Dr. Fang, for believing in me and giving me advice and guidance during the course of my research work. I would also like to thank my committee members, Dr. Smelser, Dr. Cherukuri, Dr. Weggel, Dr. Keanini, and Dr. Chen, for their valuable reviews, comments and advice on my dissertation.

I would like to thank my parents for their continued support throughout my university career. My appreciation also goes to my beloved husband, Meng Shen, for his help and support of my graduate study.

TABLE OF CONTENTS

LIST OF TABLES

LIST OF FIGURES

LIST OF SYMBOLS

f	Yield function
g	Flow potential
I_1	First stress invariant
J_2	Second stress invariant
$\hat{\sigma}$	Equivalent stress
σ_y	Yield stress
σ_e	Von Mises effective stress
σ_m	Mean stress
σ'	Deviatoric stress
σ^{tr}	Trial stress
$\sigma^{tr'}$	Deviatoric of the trial stress
H	Hardening modulus
ε	Total strain
ε^e	Elastic strain
ε^p	Plastic strain
ε^p_{eff}	Effective plastic strain
$\dot{\hat{\varepsilon}}$	Equivalent plastic strain-rate
$\dot{\varepsilon}_e$	Work rate conjugate of the von Mises stress (von Mises plastic strain-rate)
$\dot{\varepsilon}_m$	Work rate conjugate of the hydrostatic pressure (volumetric plastic strain-rate)

ρ_f	Density of foam
ρ_{f0}	Density of base material
E	Young's modulus
K	Bulk modulus
G	Shear modulus
ν	Poisson's ratio
ν^p	Plastic Poisson's ratio
SEA	Specific energy absorption
MCF	Mean crushing force
δ_{ij}	Kronecker delta

CHAPTER 1: INTRODUCTION

The work on crashworthiness can be traced back to the 1940s in the field of military aviation. In the 1950s, the U.S. Army investigated helicopter crashes to improve crashworthiness and reduce fatalities. The term “crashworthiness” refers to the ability of a structure to protect the occupants in a crash event. The goal of vehicular crashworthiness design is to let certain structural components absorb as much kinetic energy as possible so as to decrease the dynamic forces and accelerations exerted on the occupants while maintaining a sufficient survival space for the occupants. To achieve this goal, the energy absorbing structures are typically designed to deform in a controlled manner by creating initial imperfections to trigger the desired deformation pattern.

Head-on collisions, run-off-road collisions, rear-end collisions, side collisions and rollovers are the most commonly seen vehicular crashes that often result in property damage, injury, and death. They are typically unpredictable and when they cannot be avoided, it relies on vehicular crashworthiness to reduce the injury and fatality. The deformation characteristics of a crashing vehicle are of interest to many researchers and a straight forward way of analysis is by means of full-scale crash testing. In the U.S., all new vehicle designs must be tested to pass the safety standards of Federal Motor Vehicle Safety Standards and Regulations (FMVSS 1998), such as offset-frontal impacts, side impacts and roof crash. FIGURE 1.1 shows an offset-frontal impact test of a 2007 Ford

FIGURE 1.1: Offset-frontal impact test of a 2007 Ford Fusion (IIHS 2010)

Fusion (IIHS 2010). The vehicular crashworthiness is rated by its performance in these tests.

1.1 Finite Element Simulation of Crashes

Full-scale crash tests are expensive and time consuming. Due to the destructive nature of the crash testing and the limitations of data-acquisition techniques, many parameters related to crashworthiness cannot be directly measured in an experiment, e.g., the energy absorption and the time history of deformation. In addition, the test specimens cannot be reused after a crash; this imposes a significant challenge to full-scale crash testing. Consequently, full-scale crash tests are mainly used for safety evaluation and validations; they are not appropriate for design exploration and optimization purposes.

Thanks to the rapid development of computer hardware and associated technologies in the late 20^{th} century, nonlinear finite element (FE) simulation has now become an important design tool for automotive, aerospace, and other industries. A number of commercial codes are now available such as LS-DYNA (LSTC 2010), Abaqus (Abaqus 2007), PAM-CRASH (ESI 2008), and ANSYS (ANSYS 2004). Although there

are some initial costs to develop and validate an FE model, the subsequent simulation work provides a fast, cost effective, and powerful means for crashworthiness designs.

In 1981, Pifko and Winter (1981) performed the first crash simulation of a vehicle frontal impact and an aircraft crash. They showed that FE simulations could be effectively used in the design process. Restricted by the computing power at the time, only half of the vehicle was modeled using 504 elements (triangular membrane, link, beam and nonlinear spring elements), with a total of 663 degrees of freedom. Dissipative nonlinear springs were used to model the front end of the vehicle to obtain the crushing behavior. In 1983, Haug et al. (1983) carried out a quasi-static FE analysis of a vehicle-pillar impact using PAM-CRASH to investigate the application of commercial FE codes to industrial crashworthiness studies. Argyris et al. (1986) simulated the frontal impact of a car's frontal structure into a rigid wall at 13.4 *m/s*, excluding the engine, transmission and other internal parts. In this model, they considered material hardening and strain-rate effects (from 0.05 to 10.0 s^{-1}) for the standard and high-strength steel components. However, the inaccuracies in time integrations and descriptions of the mechanical behavior of the materials contributed to the inaccuracies in the resulting stress distributions.

Due to limited computing capabilities such as CPU speed, memory and data storage, these early analyses did not include contact calculations or folding/buckling of sheet metal structures. Nevertheless, these pioneering crash simulations included several features of FE analysis (FEA) that are still being used today, for instance, time integration combined with shell elements and plane stress elasto-plasticity.

Since the late 1980s, the rapid evolution of computer hardware and super computers has promoted the usage of explicit FE codes in crash analysis as well as the development of vehicle models, from the early 259-node rough model (Pifko and Winter 1981) to the more detailed models (Thacker et al. 1998, NCAC 2008). For example, Thacker et al. (1998) developed an FE model of a 1997 Honda Accord that included all major components with 40 types of materials. This FE model included 177 parts that were meshed into 88,000 elements with 93,400 nodes.

In the past decade, more and more researchers adopted full-scale crash simulations to aid the design and safety evaluations of modern vehicles. Williams et al. (2000) investigated the overall vehicle response and component interactions using nonlinear FEA. They used component-level experimental data to guide the work of vehicle modeling. For example, the front tires were modeled in details to describe their compression and recovery characteristics reflected in the dynamic tire testing. However, no full-scale experimental crash tests were performed to validate the accuracy of the predictions given by the FE simulations.

Full-scale FE simulations were used in many impact scenarios such as side impacts, rear impacts and rollovers as seen in the work of Fang et al. (2005b), Mao et al. (2005), and Gursel and Nane (2010). Using the results of full-scale simulations of an offset-frontal and a side impact, Fang et al. (2005b) performed optimization of 21 components in the vehicle to maximize energy absorption while minimizing the weight. Mao et al. (2005) carried out the first full-scale FE simulations of dynamic roof crushing tests. The study revealed that 30% of the roof strength came from the bonded windshield and that the roof strength was a function of the roll and pitch angles. The conclusions of

this study provided a guideline for choosing the worst-case roll angles for the safety specifications on vehicle rollover. Gursel and Nane (2010) simulated the frontal, offset-frontal and side impacts of a Ford Taurus and a Dodge Intrepid and showed good agreement between the experimentally recorded accelerations and FE simulation results. They also performed sensitivity analyses of the energy absorption in relation to the door thickness.

In recent years, FE simulations have been applied to highway safety analyses and roadside barrier designs. Using full-scale FE simulations, El-Tawil et al. (2005) investigated the safety performance of a bridge pier impacted by large-sized utility vehicles (a 14-*kN* Chevy truck and a 66-*kN* Ford truck). Elmarakbi et al. (2006) simulated the process of a vehicle impacting a traffic pole and proposed a pole reinforcement design in order to minimize vehicular deformations and to reduce occupant injuries. Different types of roadside barrier systems were evaluated using FE simulations as can be found in the work of Borovinsek et al. (2007), Ulker and Rahman (2008), and Bi et al. (2010b).

Borovinsek et al. (2007) used results of FE crash simulations in the evaluation of different safety barrier reinforcements to determine the best barrier design. This work was also validated using data from physical crash tests. Ulker and Rahman (2008) utilized FE simulations to develop design guidelines for a portable concrete barrier system. In their sensitivity analysis of pavement types (asphalt and concrete), impact speeds and angles, and barrier lengths, they showed that the barrier had less traverse displacement on concrete pavement and that the total barrier length needed to be at least 61 *m* to stabilize the traverse displacement. Bi et al. (2010b) evaluated the safety performance of highway cable median barriers installed on a sloped median using full-

scale FE simulations. Six cable barrier designs with different cable heights were evaluated under vehicular impacts at different angles and speeds. The simulation results showed that the post yielding provided more retention to the cables than hook-bolt yielding and that cable heights were critical to cable-vehicle engagements.

1.2 Aluminum Foam-filled Thin-walled Columns

Thin-walled columns are widely adopted crashworthy structures; they are commonly seen as the rails and other crushing members of a vehicle. These columns enhance the occupant safety in vehicular collisions by deforming progressively and absorbing a large amount of kinetic energy. Moreover, given the concern of today's automotive industry on fuel efficiency and environmental preservation, designing thin-walled columns is of special interest for their light weight and low manufacturing cost.

Proper designs of the crushing columns could reduce the impact forces on the rest of the vehicular body and the occupants, and thus enhance the safety of the vehicle. A preferred crushing column is one that absorbs a large amount of energy, is light weight (related to fuel efficiency and manufacturing cost), and retains a sufficient level of stiffness. Thin-walled columns are typically subject to loading conditions including axial loading, oblique loading (loading in the direction at an angle to the axial direction), and pure bending. Under axial loading conditions, the column undergoes successive buckling and folding, and thus absorbs a large amount of kinetic energy. Under pure bending conditions, the deformation of the member is governed by global buckling or bending in which the column absorbs less energy compared to the axial loading condition. In an actual crash event, a crushing column often undergoes a combination of pure bending and axial loading conditions.

Due to the complexity of the crash mechanism, designing crashworthy structures using the experimental approach creates significant challenges. To this end, many researchers adopted analytical models and/or numerical simulations that could be combined with optimization methods to conduct crashworthiness designs.

The first analytical model to predict the mean crushing force (MCF) and the absorbed energy of thin-walled, cylindrical columns was established in the work of Alexander (1960). Other theoretical models were subsequently derived to predict the deformation modes of thin-walled structures in axial crushing (Abramovicz and Jones 1984; Abramovicz and Wierzbicki 1989; White and Jones 1999). Numerical analyses and experiments were also conducted to verify these analytical models, many of which were based on the plastic-hinge concept and assumed a single complete folding within a constant length (Santosa et al. 2000; Chen and Wierzbicki 2001; Zhao and Abdennadher 2004; Song et al. 2005).

Metallic foams are cellular materials with air-filled pores. These pores can be interconnected (open-cell foam) or insulated (closed-cell foam). The porosity of metallic foams typically ranges from 5 to 40 pores per inch. One example of the cellular structure of aluminum foam is shown in FIGURE 1.2. Due to its many favorable properties such as low weight, high gas permeability and high thermal conductivity, metallic foams become the attractive materials to automotive, aerospace, military, and other industrial applications (Banhart 2001). Examples of its applications include heat exchangers, catalyst surfaces, energy absorbers, sandwich panels, air oil separators, aircraft wing structures, and fuel tank baffles.

One of the important applications of metallic foams is as a filler material in

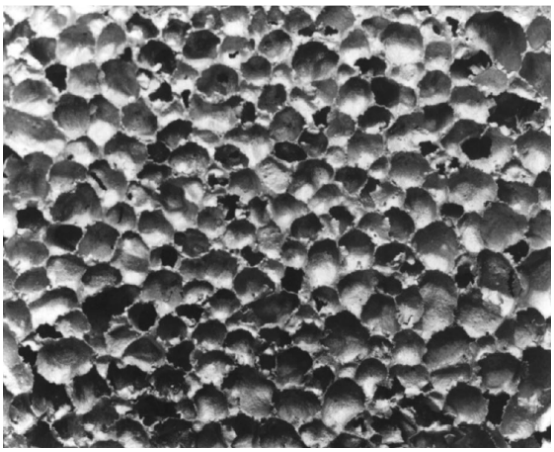

FIGURE 1.2: Cellular structure of an aluminum foam sample
(Baumeister et al. 1997)

extruded metal columns to increase the energy absorption under impact or blast loading. Aluminum foam has been extensively studied and shown to have good energy absorption under both quasi-static and dynamic loading conditions (Miyoshi et al. 1999; Kanahashi et al. 2000; Paul and Ramamurty 2000; Lopatnikov et al. 2003, 2004; Tan et al. 2005a, 2005b).

Aluminum foam is one of the commonly used crashing foams and exhibits different behaviors under compressive, tensile and shear loadings. Under quasi-static compression, the deformations of aluminum foams can be divided into three regions: elastic, quasi-plateau and densification regions (Lopatnikov et al. 2003). Elastic deformation occurs first at very low stress and strain levels. Buckling and plastic collapses of foam cells take place in the quasi-plateau region followed by densification of the foam as its density approaches to that of its constituent material (Lopatnikov et al. 2003). Unlike its constituent material (i.e., the aluminum), the density of a deforming foam keeps changing in each of the three regions with the progress of the deformations.

Several researchers studied the bending mechanism of foam-filled columns. In the

work of Kim et al. (2002), a plastic-hinge model was employed to optimize the energy absorption of an "S" frame with a square cross-section and filled with aluminum foam. Due to localized plastic deformations around the hinges, the specific energy absorption (SEA) of the "S" frame was found to be much lower than those of straight columns under axial loading. In the work of Zarei and Kroger (2008a, 2008b), the bending behavior of foam-filled beams was studied and optimization was performed on square, foam-filled tubes to find efficient and lightweight crush absorbers for maximum energy absorption.

The axial crushing mechanism of foam-filled columns was first studied in the work of Seitzberger et al. (2000), who performed physical experiments to analyze the crushing forces and energy absorption of steel columns with square, hexagonal, and octagonal cross-sections filled with aluminum foam. The study showed that the foam-filled columns had significant improvement on crushing forces over empty tubes, and that the SEAs could be increased by as much as 60%. Zhao and Abdennadher (2004) studied the behavior of square, brass columns filled with aluminum foam under axial impact. The study utilized both physical experiments and FE simulations to verify the enhancement on column strength by filling in aluminum foam. Song et al. (2005) showed that a foam-filled column had larger energy absorption than the sum of energy absorption of the foam and tube when crushed separately. This observation was the same as that in the work by Chen and Wierzbicki (2001): the foam functioned as an elastic-plastic foundation to the walls of the tubular structures, which accordingly reduced the folding wavelength and thus increased the crushing resistance as well as the energy absorption. In addition to the above observation, they also pointed out that multi-cell structures had increased SEAs over single-cell structures due to the corner effect. When multiple cells (or tubes) were

connected together and formed a multi-cell structure, the corners of each cell were then supported by walls of surrounding cells. The crushing resistance was enhanced by forming a multi-cell structure; this was also shown in the work of Hou et al. (2007) in which multi-cell columns were shown to have higher efficiency of energy absorption than single-cell columns.

With the advancement in high performance computing and parallel algorithms, FEA has been increasingly used by researchers to perform in design optimization of foam-filled thin-walled columns. For example, Mamalis et al. (2008) used LS-DYNA (LSTC 2010) to simulate the crushing process of foam-filled, thin-walled rectangular columns. However, designing crashworthy structures still imposes significant challenges due to the high computational cost and numerical instabilities of the crash simulations and the large number of analyses required by an optimization process. To perform optimization involving expensive simulations, many researchers employed the response surface methodology (RSM) to reduce the computational cost of crash analysis using whole vehicle or component models (Avalle et al. 2002; Kurtaran et al. 2002; Fang et al. 2005b). The RSM was successfully combined with the FE analysis in a number of studies on crashworthiness optimization of various columns (Yamazaki and Han 1998, 2000; Eby et al. 2002; Lee et al. 2002; Lanzi et al. 2004; Xiang et al. 2006) and other structures (Redhe et al. 2004; Fang et al. 2005a).

In the work by Hou et al. (2007), crashworthiness optimization was performed on hexagonal thin-walled columns with single- and triple-cell configurations. The SEA was optimized with a constraint on the maximum peak load. It was observed that the triple-cell configuration outperformed the single-cell configuration, and that the side-connected

configuration outperformed the vertex-connected configuration in terms of the SEA. Liu (2008) presented the optimum design of straight octagonal and curved hexagonal thin-walled tubes with the maximum crushing force as a design constraint. These works focused on the optimization of tubular geometries and did not include foams in the designs. Recently, dual-cell hexagonal columns with honeycomb cores (Zhang et al. 2008), foam-filled square tubes (Hou et al. 2009) and foam-filled hexagonal tubes (Bi et al. 2010a) were studied and optimized for maximum energy absorption.

Due to the complicated geometries of foams, they are typically modeled by solid elements in FEA using bulk material properties. The large volume and large deformation of metallic foams often cause numerical challenges in crash simulations, specifically, in solving the constitutive equations, which largely influence the accuracy and stability of these analyses. A stable and efficient constitutive model for foams is a necessity for the effective employment of FE simulations in designing foam-filled crushing components.

1.3 Constitutive Modeling of Metallic Foams

In FE simulations metallic foams are modeled as continuum solids with bulk properties that are used in the constitutive equations to produce the deformation characteristics of the material. The reliability of an FE crash simulation of a foam-filled column largely depends on the accuracy and effectiveness of the constitutive models of both the outer metal tube and the inner foam filler.

Constitutive modeling of metals has been comprehensively studied in the past. All commercial FE codes provide a number of material models for metals, most of which are based on the von Mises yield criterion. Some models include strain-rate effects and failures, for example, material types 19 and 81 in LS-DYNA (LSTC 2010). Pressure

dependent models applicable to metals were introduced by Gurson (1977), Chu and Needleman (1980), and Tvergaard and Needleman (1984). The Gurson dilatational plastic model was implemented as material type 120 in LS-DYNA (LSTC 2010).

Among the material models in commercial codes such as LS-DYNA, the power law, Cowper/Symonds and piecewise linear plasticity models are the most frequently used in crash analyses. Rabbani et al. (2009) studied the reliability of these three models for use on aluminum, high strength steel and mild steel materials. It was shown that both the power law model and the piecewise linear plasticity model provided good agreement with experiment data of uniaxial tensile tests. The piecewise linear plasticity model, however, requires users to provide stress-strain curves to obtain accurate predictions. The Cowper/Symonds model was shown to extremely overestimate the stresses at high strain-rates (135 s^{-1}).

The effects of hydrostatic pressure on material yielding are neglected in the above mentioned models based on the conclusions drawn by Bridgman (1947) and Hill (1950). However, some later experimental work (Spitzig 1975, 1976, 1984; Richmond 1980) indicated that yielding was not completely pressure independent, even for metals. Recently, the experimental work by Allen (2000, 2002) and Wilson (2002) showed a significant effect of hydrostatic pressure on the yielding of various metals.

The deformation characteristics of metallic foams are different from that of pure metals. One difficulty of modeling the metallic foam as a bulk continuum is that the observed yielding of the foam involves different mechanisms such as plastic yielding, buckling and fracture of cell walls, due to the inhomogeneous nature of the material. The inhomogeneity of metallic foams was investigated in the work of Daxner et al. (1999),

Gradinger and Rammerstorfer (1999), Meguid et al. (2002) and Reyes et al. (2004). Daxner et al. (1999) found that the foam's inhomogeneity led to stress localizations, decreased plateau stresses and efficiency of energy absorption. The same conclusion was drawn in the work of Gradinger and Rammerstorfer (1999) that the inhomogeneity could decrease the efficiency of energy absorption. Gradinger and Rammerstorfer also found that the variation in cell sizes, cell wall thicknesses and other micro-geometrical parameters could lead to a variation in foam density that lowered the plateau stresses and thus the level of energy absorption. Meguid et al. (2002) developed an FE model of multiple cells using shell elements including a random variation of foam density. The general trend of the nominal stresses of this model was found to match the nominal stress-strain curve from experimental data. The model with uniform density distribution showed unrealistic oscillations of the plateau stresses. Reyes et al. (2004) used a statistical variation of foam density in their constitutive model in which the initial density of each element was given with a normal probability (Gaussian) distribution. However, it was concluded that this variation of foam density did not help increase the accuracy of simulation results, namely the force-displacement curves.

The large strain and strain-rate (characteristic strain-rates are around $10^3\ s^{-1}$ for dynamic loadings) experienced by foam elements in crash simulations are also challenges to the incremental stress update. Moreover, the classical J_2 flow theory is no longer effective due to the existence of the plastic volumetric flow (Dunne and Petrinic 2005). Hydrostatic pressure yielding must be included in the constitutive model of foams.

Over the years, various constitutive models of metallic foams have been developed and can be found in literature. These models can be divided into two major

types. The first type uses the stress components or the principal stresses to determine the yielding of the foam. These models include the ones developed by Shaw and Sata (1966), Triantafillou et al. (1990) and Schreyer et al. (1994). Shaw and Sata (1966) used a yield function in which the maximum value of the three principal stresses was compared to the predefined yield stress. Due to the difficulties with experimental scatter and the lack of tensile loading data, the yield surface in the principal stress space was not established. Triantafillou et al. (1990) suggested that the yield function be formulated such that when a certain stress component reached the yield stress, the material became plastic. The authors, however, did not specifically define this function. Schreyer et al. (1994) used a spherical yield surface in the principal stress space to account for the strain hardening of metallic foams.

The second type of model uses the first and second stress invariants of the stress tensor that correspond to the hydrostatic pressure and the von Mises stress to determine the yielding of the foam. Drucker and Prager (1952) first proposed this type of constitutive model. Subsequent models are found in the work by Gurson (1977), Ragab and Saleh (1999), Wen et al. (2005) and Monchiet et al. (2008). However, the yield functions in these models include first or lower order terms of the hydrostatic pressure and the von Mises stress.

Yield functions including second order terms in the hydrostatic and von Mises stresses include those proposed by Gibson et al. (1989), Zhang et al. (1997), Miller (2000), Deshpande and Fleck (2000) and Doyoyo and Wierzbicki (2003).

The yield function proposed by Miller (2000) incorporated a polynomial of stress invariants into the yield function. A first-order term was adopted in von Mises stress.

Both the first- and second-order terms were adopted for the hydrostatic pressure. In order to account for strain hardening, the predefined uniaxial yield stress was scaled by the volumetric strain and formulated into the yield function. In the work by Doyoyo and Wierzbicki (2003), the yield function was composed of a first-order term in the von Mises stress and both the first- and second-order term in the hydrostatic pressure.

The models proposed by Zhang et al. (1997) and Deshpande and Fleck (2000) consisted of second-order terms in both the von Mises stress and hydrostatic pressure. The yield surfaces in these two models were elliptic in the hydrostatic pressure-von Mises stress space. In the work of Deshpande and Fleck (2000), two constitutive models were proposed: the self-similar evolution model in which the yield surface expanded with material hardening, and the differential hardening model in which both the size and shape of the yield surface would change with material hardening. It was found that the differential hardening model predicted the stress-strain responses to a high level of accuracy and outperformed the self-similar evolution model. However, the differential hardening model was too complicated to warrant its practical usage.

There are a number of material models of metallic foams available in LS-DYNA; however, Hanssen et al. (2002) found that none of them could predict, with sufficient accuracy, the behavior of different experimental validation data. Moreover, these models cannot effectively account for the change of compressibility during the crushing process in which the density of the metallic foam increases with accumulation of plastic strains and thus reducing the foam's compressibility. Since these models were implemented into the commercial package, they cannot be modified to include the above mentioned capability such as modeling the change of material's compressibility during hardening.

In this dissertation a new constitutive model was developed for metallic foams by adopting an elliptic yield surface whose shape and size can both be changed with material hardening. To include the change of material compressibility, a function was derived to explicitly express the compressibility in terms of the volumetric plastic strains. This new constitutive model was implemented into LS-DYNA as a user material subroutine. The implicit integration method proposed by Aravas (1987) was used to carry out numerical integrations of the constitutive equations. The new model was validated using uniaxial and diagonal loading tests before being applied to crash simulations of foam-filled columns.

In the remaining chapters of this dissertation, a brief introduction of contact theory and modeling is first presented. General aspects of constitutive modeling and six built-in foam models in LS-DYNA are then described. The formulation and functionality of the new foam model are subsequently introduced. Following the verification and validation of the new constitutive model, crash simulations of foam-filled columns using the new foam model are presented and compared to those using LS-DYNA built-in models. Finally, the work of this dissertation is summarized and some conclusions are drawn based on analysis of the simulation results.

CHAPTER 2: CONTACT THEORY AND MODELING

Contact problems exist in many engineering systems. Modeling contacts imposes substantial numerical challenges and computational costs. Contact surfaces are usually unknown prior to loading and may constantly change after loading. Also, the forces and displacements on these surfaces are unknown and need to be calculated during the entire course of contacts. In crash simulations, there are a large number of contacts due to the large displacements and deformations of the components. Contacts need to be properly detected and handled among contacting components to avoid unrealistic penetrations, which would significantly reduce the accuracy of numerical simulations. This chapter gives some basic strategies that are used in FE analysis to simulate contacts.

2.1 Contact Methods and Formulations

The penalty method is commonly used in both explicit and implicit FE codes for contact treatment. In this method, imagined normal interface springs are placed between all penetrating nodes, and the forces in the springs are calculated based on the levels of penetration. The stiffness of these springs is called the contact stiffness, which depends on the contacting materials and geometric properties. When a penetration between two contacting surfaces is detected, contact forces are calculated and applied to the penetrating nodes to separate them from the penetrated surfaces. Contact forces are assembled into the system of governing equations (Laursen 2003) given by

$$\mathbf{M}\ddot{\mathbf{d}}(t) + \mathbf{F}^{\text{int}}(\mathbf{d}(t)) + \mathbf{F}^{\text{c}}(\mathbf{d}(t)) = \mathbf{F}^{\text{ext}}(t) \tag{2.1}$$

where t is the time, $\mathbf{M}$ is the mass matrix, $\mathbf{F}^{int}$ is the vector of internal forces, $\mathbf{F}^{c}$ is the vector of contact forces, $\mathbf{F}^{ext}$ is the vector of external forces, $\mathbf{d}(t)$ is the displacement vector at the given time instant, and $\ddot{\mathbf{d}}(t)$ is the acceleration vector. Equation (2.1) is typically highly nonlinear for contact problems. For example, the internal forces have a nonlinear relationship with displacements due to material nonlinearities; the contact force is a nonlinear function of displacements due to the nonlinearities of the contact interfaces. To obtain the numerical solution of Eq. (2.1), the contact forces are first calculated using the contact stiffness $\mathbf{K}^{c}$ whose relationship with the contact force is given by

$$\mathbf{K}^{c}(\mathbf{d}) = \frac{\partial}{\partial \mathbf{d}} \mathbf{F}^{c}(\mathbf{d}) \tag{2.2}$$

In the FE implementations of contact treatment, there are different formulations for calculating the contact stiffness. The rest of this section explains three commonly used formulations.

2.1.1 Standard Penalty Formulation

In a contact problem, each of the two contacting interfaces is discretized into a group of segments, with one interface denoted as “slave” and the other as “master”. In FEA, a segment is typically represented by a shell or solid element on the contact surface (FIGURE 2.1). In a contact analysis, a search is carried out for each slave node to find the nearest node on the master surface. Elements sharing this node (on the master surface) are used to determine the normal projections of the master surface. At each time-step a penetration check is performed to determine if any node on the slave surface has penetrated through the master surface. If a penetration is detected, a repulsive contact

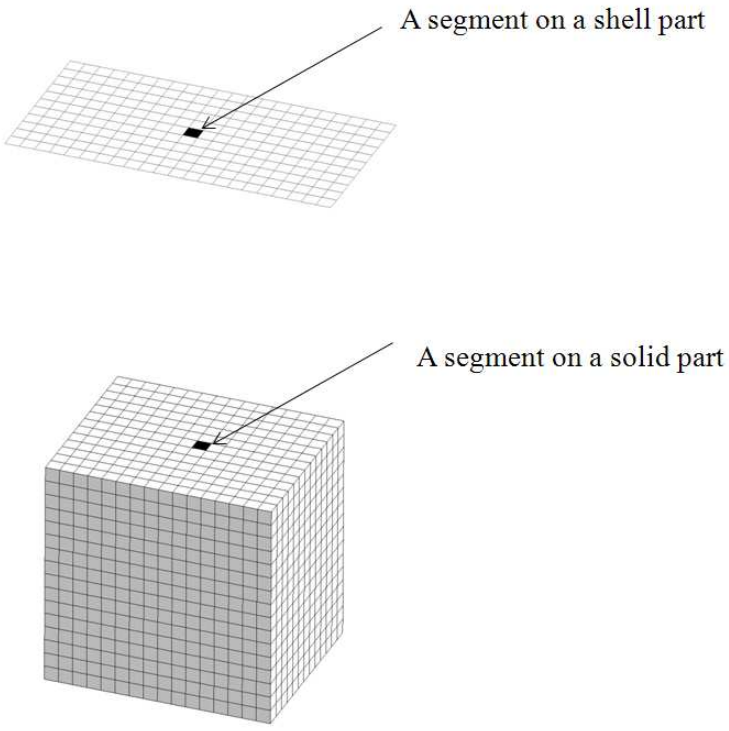

FIGURE 2.1: Segments defined on a shell/solid part

force is applied to separate the contacting surfaces and eliminate the penetration. The contact force is proportional to the penetration depth and is calculated by

$$\mathbf{f}_c = -l \times k_i \times \mathbf{n}_i \tag{2.3}$$

where l is the penetration depth, k_i is the contact stiffness of the i-th segment, and $\mathbf{n}_i$ is the normal vector of the i-th segment on the master surface at the contact location. For shell elements the contact stiffness k_i is defined by

$$k_i = \frac{S_i K_i A_i}{\max(diagonal\ length\ of\ shell)} \tag{2.4}$$

where S_i is a scale factor (rangeing from 0 – 1 with a default value of 0.1 in LS-DYNA), K_i is the bulk modulus of the element, and A_i is the area of the shell element. For solid elements the contact stiffness k_i is defined by

$$k_i = \frac{S_i K_i A_i^2}{V_i} \tag{2.5}$$

where V_i is the volume of the element and A_i is the surface area that contains the *i*-th master segment (Hallquist 2006). The remaining variables have the same meaning as those in Eq. (2.4).

2.1.2 Soft-constraint Formulation

The soft-constraint formulation is intended for treating contacts between bodies with dissimilar material properties (e.g., metals and foams). In addition to the contact stiffness calculated by the standard penalty formulation, an alternative stiffness is calculated based on the stability of a local spring-mass system, as given by

$$k_{cs} = 0.5 \cdot SSC \cdot m^* \cdot (\frac{1}{\Delta t_c}) \tag{2.6}$$

where SSC is a scale factor, m^* is a function of the masses of the slave and master nodes, Δt_c is the current time-step. The stiffness calculated by Eq. (2.6) is compared to that calculated by the standard penalty formulation, e.g., Eq. (2.4) or (2.5), and the larger of the two is used in calculating the contact force.

2.1.3 Segment-based Formulation

The segment-based formulation is another penalty method implemented in FE codes such as LS-DYNA. In this formulation the slave and master segments are used instead of the slave node and master segment. In the case of two 4-node segments coming

into contact, contact forces are applied to the eight nodes. This formulation distributes contact forces more evenly and sometimes can be effective for very "stubborn" contact problems (Hallquist 2006). In this formulation, an alternative stiffness is defined by

$$k_{cs} = 0.5 \cdot SSG \cdot \left\{ \begin{matrix} SFS \\ or \\ SFM \end{matrix} \right\} \cdot \left(\frac{m_1 m_2}{m_1 + m_2}\right) \cdot \left(\frac{1}{\Delta t_c}\right) \tag{2.7}$$

where SSG is the scale factor for sliding interface penalties, SFS is the scale factor on default slave penalty stiffness, SFM is the scale factor on default master penalty stiffness, m_1 and m_2 are masses of the slave and master segments, respectively. For shell elements, the segment mass is equal to the element mass; for solid elements, the segment mass is equal to half the element mass. This formulation differs from the soft-constraint formulation in how the time-step size is updated. The time-step is only updated when it is increased by more than 5%. Therefore, the time-step used in this formulation is usually constant.

2.2 Contact Modeling in LS-DYNA

In an FE model of a contact problem, components that are potentially in contact during the simulation need to be predefined in a group or groups, and the algorithm to handle each group of contacts needs to be specified. This is called contact definition for which there are a variety of contact types in LS-DYNA, each corresponding to a specific contact algorithm with a choice of the aforementioned formulations of contact stiffness. In this section, four commonly used contact types are introduced, ranging from simple to complex contact algorithms.

2.2.1 Nodes-to-Surface Contacts

The nodes-to-surface contact type is a simple one-way treatment of contacts between two different parts or two groups of parts, one being called the slave and the other the master. Both the master and slave parts need to be specified in the contact definition. At each time-step of a contact analysis, each node on the surfaces of slave parts is checked for penetration through the master surfaces, as schematically shown in FIGURE 2.2. If a penetration is detected, normal and tangential forces are applied between the slave node and the contacting surfaces. The magnitude of the normal force is proportional to the penetration depth. The magnitude of the tangential force is calculated through a Coulomb friction formulation if sliding along the contacting surfaces occurs. The coefficient of Coulomb friction is given by

$$\mu_c = FD + (FS - FD)e^{-DC|v_{rel}|} \tag{2.8}$$

where FD is the coefficient of dynamic friction, FS is the coefficient of static friction, DC is the exponential decay coeffcient, and v_{rel} is the relative velocity of the contacting surfaces.

Nodes-to-surface contacts are often used in problems where the master part is a rigid body and/or when the slave surface has a finer mesh than that of the master surface. This type of contact performs a one-way treatment of penetration check. In addition, the penetration check is only performed on slave nodes that are pointed by the normal vectors of the master surface. Therefore, this type of contact may not work well for contacts between highly deformable and/or geometrically complex parts, because penetrations may not be detected by the one-way treatment of contact. Consequently, this contact type

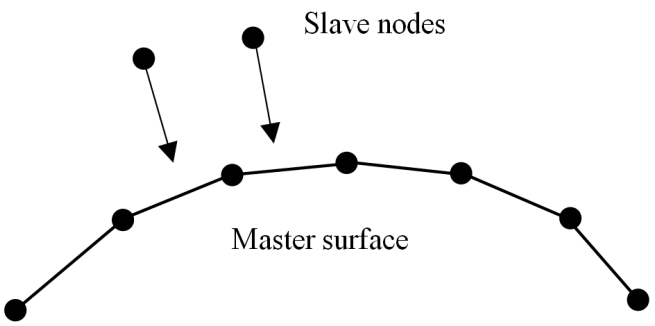

FIGURE 2.2: Nodes-to-surface contact

may be either inaccurate due to undetected contacts or numerically unstable due to large penetrations detected at a later stage.

A modification to the nodes-to-surface contact type is to use a two-way contact check and is given by the automatic-nodes-to-surface contact type. The two-way treatment is essentially the same as the one-way nodes-to-surface contact type except that it checks nodal penetrations on both sides of the master surface. The computational time of the automatic-nodes-to-surface contact type is approximately two times that of the one-way contact treatment (Hallquist 2006).

2.2.2 Surface-to-Surface Contacts

The surface-to-surface contact type is similar to the one-way node-to-surface contact type in which a slave and a master surface are specified. At each time-step of the contact analysis, each node on the slave surface is checked for penetration through the master surface (FIGURE 2.3). Unlike the nodes-to-surface contact type, however, the normal orientations of the slave surfaces in surface-to-surface contacts are also critical: penetrations will only be checked on nodes of the slave surfaces whose normal vectors are oriented towards the master surface.

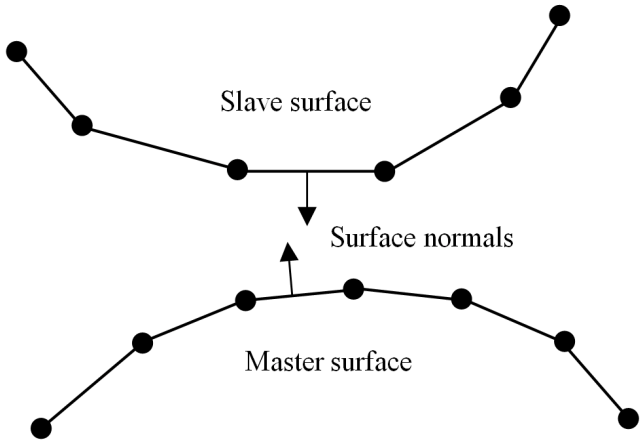

FIGURE 2.3: Surface-to-surface contact

Similar to the automatic-nodes-to-surface contacts, the automatic-surface-to-surface contact type also provides a two-way contact treatment. With the 'automatic' option, this contact type also checks nodes on the master surfaces for penetration through the slave surfaces. The automatic-surface-to-surface contact type provides a symmetric treatment, that is, defining the slave and master surfaces is arbitrary. It is a recommended contact type in analyses such as metal forming simulations that typically involve large deformations and unpredictable orientations of the deforming parts (Hallquist 2006).

2.2.3 Automatic-Single-Surface Contacts

The automatic-single-surface contact type is among the most widely used contact types in LS-DYNA. In this contact type, all the parts are defined as the slave (either a single part or a group of parts) and no master is specified. Penetrations between any two surfaces of all parts in the group are checked, including self-contacts that are between two surfaces of the same part (see FIGURE 2.4). The automatic-single-surface contact type makes it easy for defining contacts in applications involving large numbers of potentially contacting components. For example, in automotive crash simulations, the

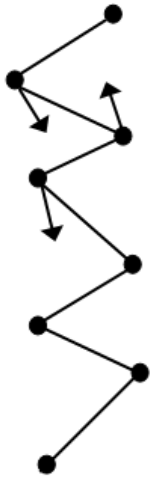

FIGURE 2.4: Automatic-single-surface contact

entire vehicle can be included in one definition of this single-surface contact where all the nodes and elements may interact.

The automatic-single-surface contact type implements a segment-based contact formulation in which segments instead of nodes are checked for penetrations through other segments and the contact forces are applied to the nodes of the corresponding segments. In addition, the contact stiffness is calculated in a slightly different way from the nodes-to-surface and surface-to-surface contact types (including those with the 'automatic' option) in which the contact stiffness is based on the properties of the master element. For segment-based contacts, however, the properties of elements of both slave and master segments are used for calculating the contact stiffness (Eq. 2.7).

2.2.4 Automatic-General Contacts

The automatic-general contact type is also a non-oriented (penetration can be detected from either side of a shell element), segment-based contact. In the case of shell elements, contact surfaces are projected normally from the shell mid-plane at a distance

equal to one-half the shell thickness. The automatic-general contact is similar to the automatic-single-surface contact but has a major difference in the number of segments checked for penetration. In the automatic-general contact type, three contact segments are used for each slave node instead of two segments in the automatic-single-surface contact by default. The automatic-general contact type also has a higher frequency of contact search to identify and track possible master segments for the given slave nodes. The contact search is performed at an interval of every ten time-steps, which is ten times the frequency of the automatic-single-surface contact. The automatic-general contact type is usually more stable than other contact types and is recommended for complicated impact/interaction scenarios such as high-speed impact, buckling and folding applications, with the cost of significantly increased computational time (Hallquist 2006).

The automatic-general contact type can also be used on beam-to-beam, beam-to-shell-edge and shell-edge-to-edge contacts. In these situations, contacts are checked along the entire length of the beam elements or the exterior edges of the shell elements, rather than only checked at the nodes. At the exterior edge of a shell surface, the contact surface wraps around the shell edge with a radius equal to one-half the shell thickness thus forming a continuous contact surface. In addition, the ‘interior’ option of the automatic-general contact (i.e., automatic-general-interior) will initiate contact checking on the interior edges of shell elements. FIGURE 2.5 illustrates the definitions of exterior and interior edges: an exterior edge is one that belongs to only one element, whereas an interior edge is shared by two or more elements. Using the ‘interior’ option will typically incur additional computational cost, but this may be necessary for certain applications

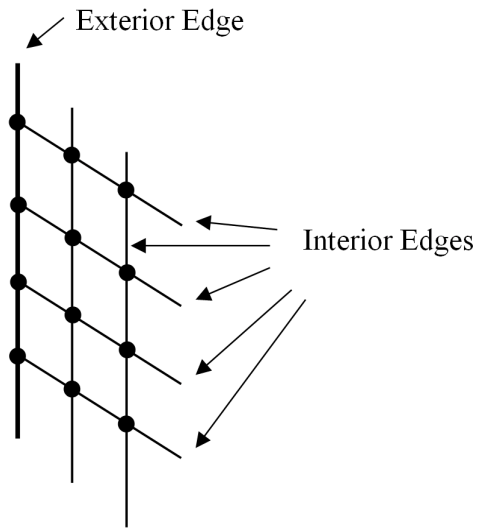

FIGURE 2.5: Exterior and interior edges

such as those with sharp corners protruding from contact surfaces due to large deformations, commonly seen in crash simulations.

Due to the searching algorithm and the high frequency of contact checking, the automatic-general contact type has an extremely high computational cost. It is therefore only recommended for use in situations where edge-to-edge and/or beam-to-beam contacts are anticipated.

CHAPTER 3: CONSTITUTIVE MODELING OF METALLIC FOAMS

Constitutive modeling is the mathematical description of how a material responds to various external loading conditions. A constitutive model is typically formulated in terms of one or more stress-strain relationships. Constitutive modeling has been a key research area in solid mechanics due to its complexity and significance in engineering applications. It covers research topics in elasticity, plasticity, thermoplasticity, creep theory, nonlinear FE method and integration of elastoplastic constitutive equations.

Plasticity theory deals with the calculation of internal stresses and strains of a body that is permanently deformed when external forces are applied. Plastic deformations are dependent on the loading paths and are calculated incrementally. Classical plasticity theory is based on polycrystalline materials whose plastic deformation is shown to be governed by the crystal slip from mechanical tests of single-crystal metals. Unlike the elastic deformation in which the interatomic bonds are stretched, the interatomic bonds may break and reform during plastic deformation, resulting in one layer of atoms displacing permanently relative to their neighboring atoms. The crystal slip suggests that the plastic deformation originates from a shear yielding process.

Bridgman (1947) conducted a series of tensile tests on smooth aluminum, copper, bronze and steel bars under external hydrostatic pressures up to 3,100 MPa. He found no significant change in the yield stress, and the volume change was negligible under high plastic strain. He concluded that the pressure dependency of metals on yielding was

negligible and thus metals could be treated as incompressible during plastic flows. His argument led to two major assumptions in classical plasticity theory: (1) volume does not change under hydrostatic pressure (the incompressibility condition); (2) yielding is not affected by hydrostatic pressure. A third assumption made in the classical plasticity theory is that, in a polycrystalline material, plastic yielding is an isotropic process. These three assumptions are the cornerstone of classical plasticity theory.

The rest of this section gives an overview of the fundamentals of constitutive modeling based on classical plasticity theory.

3.1 Preliminaries

Consider a right-handed rectangular coordinate system; the second-order stress tensor $\boldsymbol{\sigma}$ can be expressed in the matrix form

$$\boldsymbol{\sigma} = \begin{bmatrix} \sigma_x & \tau_{xy} & \tau_{xz} \\ \tau_{yx} & \sigma_y & \tau_{yz} \\ \tau_{zx} & \tau_{zy} & \sigma_z \end{bmatrix} \tag{3.1}$$

The mean stress σ_m, also known as the hydrostatic pressure, is given by

$$\sigma_m = \frac{\sigma_x + \sigma_y + \sigma_z}{3} \tag{3.2}$$

The deviatoric stress tensor $\boldsymbol{\sigma}'$ can be expressed in matrix form

$$\boldsymbol{\sigma}' = \begin{bmatrix} \sigma_x - \sigma_m & \tau_{xy} & \tau_{xz} \\ \tau_{yx} & \sigma_y - \sigma_m & \tau_{yz} \\ \tau_{zx} & \tau_{zy} & \sigma_z - \sigma_m \end{bmatrix} = \begin{bmatrix} \sigma'_x & \tau_{xy} & \tau_{xz} \\ \tau_{yx} & \sigma'_y & \tau_{yz} \\ \tau_{zx} & \tau_{zy} & \sigma'_z \end{bmatrix} \tag{3.3}$$

or in the suffix notation

$$\sigma'_{ij} = \sigma_{ij} - \sigma_m \delta_{ij} = \sigma_{ij} - \frac{1}{3}\sigma_{kk}\delta_{ij} \tag{3.4}$$

where δ_{ij} is the Kronecker delta whose value is unity when $i = j$ and zero when $i \neq j$.

3.2 Yield Criteria and Hardening Rules

The von Mises yield function is defined as

$$f = \sigma_e - \sigma_y \tag{3.5}$$

where σ_e is the von Mises stress given by

$$\sigma_e = \sqrt{\frac{3}{2}\sigma_{ij}^{'}\sigma_{ij}^{'}} \tag{3.6}$$

The yield criterion is stated as

$$\begin{cases} f < 0 : \text{Elastic deformation} \\ f = 0 : \text{Plastic deformation} \end{cases} \tag{3.7}$$

where equation $f = 0$ represents a cylindrical surface in the principal stress space, called the yield surface as illustrated in FIGURE 3.1. The material does not yield as long as the von Mises stress stays within the cylinder no matter how large the hydrostatic pressure is.

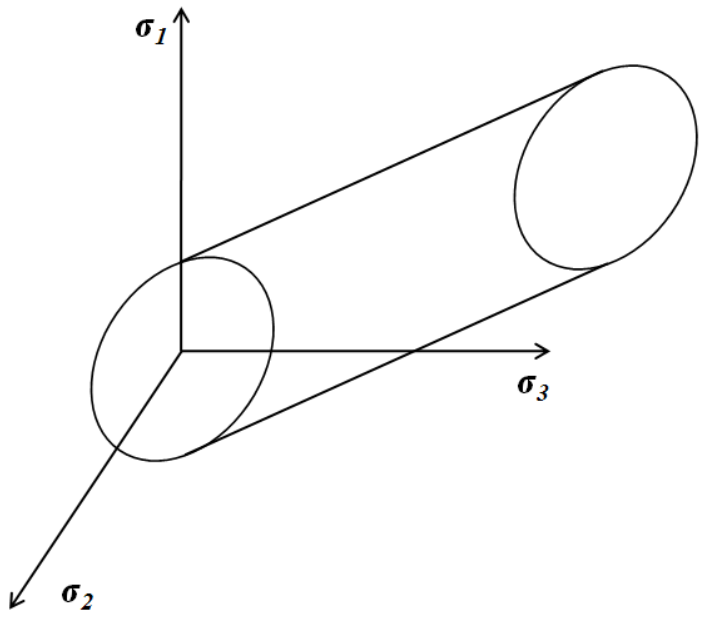

FIGURE 3.1: Yield surface in the principal stress space

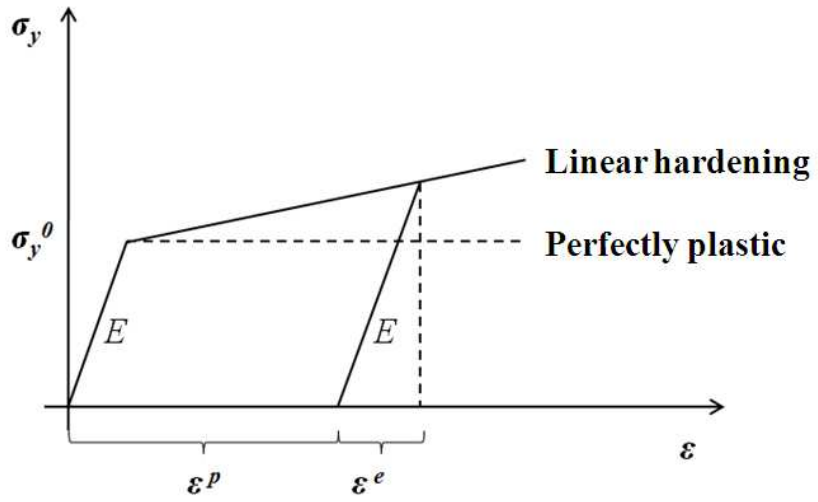

FIGURE 3.2: Stress-strain relationship and decomposition of strains

Strain hardening refers to the increase of yield stress with increase in plastic strain. FIGURE 3.2 shows an idealized stress-strain curve of a uniaxial tensile test in which the material has a linear strain hardening in the plastic region. Under uniaxial tensile stress, the material deforms elastically at first. When the initial yield stress σ_y^0 is reached, the plastic deformation starts. After unloading from a point in the plastic region, the material recovers the elastic portion of the deformation ε^e and gains an increased yield stress (the stress value at the unloading point). The remaining strain or permanent deformation is the effective plastic strain represented by ε^p in FIGURE 3.2. During a loading process, the total strain can be additively decomposed into two portions expressed by

$$\varepsilon = \varepsilon^e + \varepsilon^p \tag{3.8}$$

The stress can therefore be written as

$$\sigma = E\varepsilon^e = E(\varepsilon - \varepsilon^p) \tag{3.9}$$

For linear hardening, as illustrated in FIGURE 3.2, the hardening rule can be written as

$$\sigma_y = \sigma_y^0 + H(\varepsilon_{eff}^p) \tag{3.10}$$

where H is the increase over initial yield stress due to strain hardening and is a function of the amount of effective plastic strain. For nonlinear hardening, a function can be proposed to represent the plastic stress-strain relationship with parameters determined by material test data. Alternatively, a piecewise-linear stress-strain curve can be provided to approximate the nonlinear hardening curve.

3.2.1 The Flow Rule

Once a material yields, the plastic flow follows. In crystalline solids, the plastic flow involves the change of shape of the material due to dislocation motion by the movement of individual atoms. The plastic flow theory states that the increment of plastic strain is in the normal direction of the yield surface at the loading point; this is known as the normality flow condition as illustrated in the two-dimensional principal stress space in FIGURE 3.3.

The normality condition can be expressed in terms of the yield function as

$$d\boldsymbol{\varepsilon}^p = d\lambda \frac{\partial f}{\partial \boldsymbol{\sigma}} \tag{3.11}$$

where $d\boldsymbol{\varepsilon}^p$ is the plastic strain increment, where $\frac{\partial f}{\partial \boldsymbol{\sigma}}$ is the normal vector of the yield surface at the initial stress state, and $d\lambda$ is the plastic multiplier to be determined.

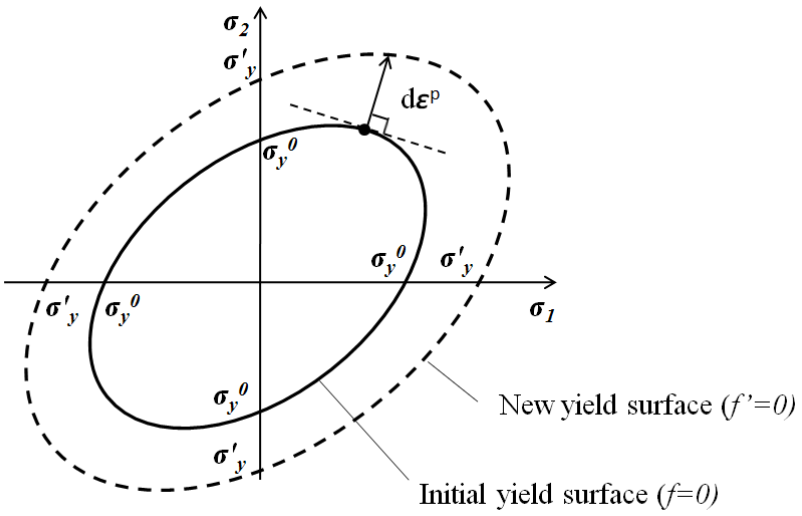

FIGURE 3.3: Plastic flow in a two-dimensional principal stress space

For the von Mises yield criterion, The von Mises stress can be written in terms of the six stress components as

$$\sigma_e = \left\{ \frac{3}{2} \left[(\sigma_{11} - \sigma_m)^2 + (\sigma_{22} - \sigma_m)^2 + (\sigma_{33} - \sigma_m)^2 + \sigma_{12}{}^2 + \sigma_{13}{}^2 + \sigma_{23}{}^2 \right] \right\}^{1/2} \tag{3.12}$$

and the normal vector of the yield surface can be written as

$$\frac{\partial f}{\partial \sigma_{ij}} = \frac{3}{2} \frac{\sigma'_{ij}}{\sigma_e} \tag{3.13}$$

where σ'_{ij} is the deviatoric stress components. Thus, the increment of plastic strain can be written as

$$d\boldsymbol{\varepsilon}^p = d\lambda \frac{\partial f}{\partial \sigma_{ij}} = \frac{3}{2} d\lambda \frac{\sigma'_{ij}}{\sigma_e} \tag{3.14}$$

and the increment of the effective plastic strain is consequently

$$
\begin{aligned}
d\varepsilon_{eff}^{p} &= (\frac{2}{3} d\boldsymbol{\varepsilon}^{p} : d\boldsymbol{\varepsilon}^{p})^{1/2} \\
&= (\frac{2}{3}\frac{3}{2} d\lambda \frac{\boldsymbol{\sigma}'}{\sigma_e} : \frac{3}{2} d\lambda \frac{\boldsymbol{\sigma}'}{\sigma_e})^{1/2} \\
&= d\lambda \frac{(\frac{3}{2}\boldsymbol{\sigma}' : \boldsymbol{\sigma}')^{1/2}}{\sigma_e} \\
&= d\lambda
\end{aligned}
\tag{3.15}
$$

where $\boldsymbol{\sigma}'$ is the deviatoric stress tensor; and the contracted tensor product (A:B) is defined by

$$
\boldsymbol{A} : \boldsymbol{B} = \sum_{i=1}^{n} \sum_{j=1}^{n} A_{ij} B_{ij} \tag{3.16}
$$

Therefore, in von Mises criterion the value of the plastic multiplier equals the increment of the effective plastic strain; and the flow rule is rewritten as

$$
d\boldsymbol{\varepsilon}^{p} = \frac{3}{2} d\varepsilon_{eff}^{p} \frac{\boldsymbol{\sigma}'}{\sigma_e} \tag{3.17}
$$

The consistency condition is used to determine the plastic multiplier or the increment of the effective plastic strain. The consistency condition requires that the stress state stay on the yield surface during yielding. When strain hardening is considered, the stress state changes to a new, expanded yielded surface. The consistency condition is given by the following two equations:

$$
f(\boldsymbol{\sigma}, \varepsilon_{eff}^{p}) = 0 \tag{3.18}
$$

$$
f(\boldsymbol{\sigma} + d\boldsymbol{\sigma}, \varepsilon_{eff}^{p} + d\varepsilon_{eff}^{p}) = 0 \tag{3.19}
$$

Eq. (3.19) is expanded by the first-order Taylor series as

$$
f(\boldsymbol{\sigma} + d\boldsymbol{\sigma}, \varepsilon_{eff}^{p} + d\varepsilon_{eff}^{p}) = f(\boldsymbol{\sigma}, \varepsilon_{eff}^{p}) + \frac{\partial f}{\partial \boldsymbol{\sigma}} : d\boldsymbol{\sigma} + \frac{\partial f}{\partial \varepsilon_{eff}^{p}} d\varepsilon_{eff}^{p} \tag{3.20}
$$

From Eqs. (3.18) and (3.20), we have

$$\frac{\partial f}{\partial \boldsymbol{\sigma}} : d\boldsymbol{\sigma} + \frac{\partial f}{\partial \varepsilon_{eff}^{p}} d\varepsilon_{eff}^{p} = 0 \tag{3.21}$$

In the principal stress space, Eq. (3.21) can be written as

$$\frac{\partial f}{\partial \boldsymbol{\sigma}} \cdot d\boldsymbol{\sigma} + \frac{\partial f}{\partial \varepsilon_{eff}^{p}} d\varepsilon_{eff}^{p} = 0 \tag{3.22}$$

3.2.2 Implicit and Explicit Integrations of Constitutive Equations

Eq. (3.21) and the Hooke's law in the following incremental form where $\boldsymbol{C}$ is the fourth-order tensor of material constants,

$$d\boldsymbol{\sigma} = \boldsymbol{C} d\boldsymbol{\varepsilon}^{e} = \boldsymbol{C}(d\boldsymbol{\varepsilon} - d\boldsymbol{\varepsilon}^{p}) \tag{3.23}$$

are the constitutive equations that need to be solved to determine the effective plastic strain increment $d\varepsilon_{eff}^{p}$ - the same value as the plastic multiplier. Both explicit and implicit integration methods can be used to solve the constitutive equations. The following briefly presents an explicit and an implicit integration method used in plasticity.

(a) First-order forward Euler integration

The first-order forward Euler method is an explicit integration method. This method is efficient and easy to implement, but does not ensure the consistency condition at time instant $t+\Delta t$, where the stress is to be determined using the strain, tangent modulus and yield surface normal at time instant t. The stress state calculated by this method is not guaranteed to stay on the updated yield surface. Furthermore, this method is only conditionally stable due to the explicit scheme. The stability and accuracy of the method depend on the time-step size. First-order accuracy is achieved at each time step, and the final solution may deviate from the true one.

Using the first-order forward Euler method, Eqs. (3.17), (3.21) and (3.23) are combined and expressed as

$$\mathbf{n}\cdot\boldsymbol{C}(d\boldsymbol{\varepsilon}-d\lambda\mathbf{n})+\frac{\partial f}{\partial \varepsilon_{eff}^{p}}d\lambda=0 \tag{3.24}$$

where $\mathbf{n}=\dfrac{\partial f}{\partial \boldsymbol{\sigma}}=\dfrac{3}{2}\dfrac{\boldsymbol{\sigma}'}{\sigma_e}$. The plastic multiplier, $d\lambda$ is given by

$$d\lambda=\frac{\mathbf{n}\cdot\boldsymbol{C}d\boldsymbol{\varepsilon}}{\mathbf{n}\cdot\boldsymbol{C}\mathbf{n}-\dfrac{\partial f}{\partial \varepsilon_{eff}^{p}}} \tag{3.25}$$

where $\dfrac{\partial f}{\partial \varepsilon_{eff}^{p}}=h$ for linear hardening (h: hardening modulus).

At time instant t, the plastic multiplier, increment in the stress tensor and the yield stress are computed as follows:

$$d\lambda(t)=\frac{\mathbf{n}(t)\cdot\boldsymbol{C}d\boldsymbol{\varepsilon}(t)}{\mathbf{n}(t)\cdot\boldsymbol{C}\mathbf{n}(t)-h} \tag{3.26}$$

$$d\boldsymbol{\sigma}(t)=\boldsymbol{C}(d\boldsymbol{\varepsilon}(t)-d\lambda\mathbf{n}(t)) \tag{3.27}$$

$$d\sigma_y=h\cdot d\lambda(t) \tag{3.28}$$

The stresses and strains at $t+\Delta t$ are computed consequently by

$$\boldsymbol{\sigma}(t+\Delta t)=\boldsymbol{\sigma}(t)+d\boldsymbol{\sigma}(t) \tag{3.29}$$

$$\varepsilon_{eff}^{p}(t+\Delta t)=\varepsilon_{eff}^{p}(t)+d\varepsilon_{eff}^{p}(t) \tag{3.30}$$

$$\sigma_y(t+\Delta t)=\sigma_y(t)+d\sigma_y(t) \tag{3.31}$$

(b) Radial return method

The radial return method is an implicit integration method. In this method, an elastic trial strain increment is first used, and the correct stresses are obtained by scaling back to the updated yield surface. Its name comes from the fact that the von Mises yield surface is a circle in the deviatoric-plane (the deviatoric plane is a plane passing through the origin and is 60 degrees to all three axes in the principal stress space and is given by

$\sigma_1 + \sigma_2 + \sigma_3 = 0$) and the back scaling is always in the direction towards the center of the circle.

Hooke's law can be written in terms of the elastic strain tensor as

$$\boldsymbol{\sigma} = 2G\boldsymbol{\varepsilon}^e + (K - \frac{2}{3}G)tr(\boldsymbol{\varepsilon}^e)\boldsymbol{I} \tag{3.32}$$

The elastic strain tensor at the end of a time-step is further written as

$$\begin{aligned} \boldsymbol{\varepsilon}^e &= \boldsymbol{\varepsilon}_t^e + \Delta\boldsymbol{\varepsilon}^e \\ &= \boldsymbol{\varepsilon}_t^e + \Delta\boldsymbol{\varepsilon} - \Delta\boldsymbol{\varepsilon}^p \end{aligned} \tag{3.33}$$

where $\boldsymbol{\varepsilon}_t^e$ is the trial elastic strain. Substituting Eq. (3.33) into Eq. (3.32) and re-organizing assuming the incompressibility condition ($tr(\boldsymbol{\varepsilon}^p) = 0$), the following is obtained

$$\begin{aligned} \boldsymbol{\sigma} &= 2G(\boldsymbol{\varepsilon}_t^e + \Delta\boldsymbol{\varepsilon}) + (K - \frac{2}{3}G)tr(\boldsymbol{\varepsilon}_t^e + \Delta\boldsymbol{\varepsilon})\boldsymbol{I} - 2G\Delta\boldsymbol{\varepsilon}^p \\ &= \boldsymbol{\sigma}^{tr} - 2G\Delta\boldsymbol{\varepsilon}^p \end{aligned} \tag{3.34}$$

where $\boldsymbol{\sigma}^{tr}$ is the trial elastic stress and $-2G\Delta\boldsymbol{\varepsilon}^p$ is the plastic corrector based on the plastic strain increment. Substituting the plastic strain increment given by Eq. (3.17), Eq. (3.34) is written as

$$\boldsymbol{\sigma} = \boldsymbol{\sigma}^{tr} - 3G\Delta\varepsilon_{eff}^p \frac{\boldsymbol{\sigma}'}{\sigma_e} \tag{3.35}$$

The deviatoric of the trial stress is given by

$$\begin{aligned} \boldsymbol{\sigma}^{tr'} &= \boldsymbol{\sigma}^{tr} - \frac{1}{3}(\boldsymbol{\sigma}^{tr} : \boldsymbol{I})\boldsymbol{I} \\ &= \boldsymbol{\sigma}^{tr} - K\ tr(\boldsymbol{\varepsilon}_t^e + \Delta\boldsymbol{\varepsilon})\boldsymbol{I} \end{aligned} \tag{3.36}$$

where $\frac{1}{3}(\boldsymbol{\sigma}^{tr} : \boldsymbol{I})$ is the mean trial stress. Since the trace of the plastic strain increment is zero for incompressible plasticity ($tr(\Delta\boldsymbol{\varepsilon}^{p}) = 0$),

$$\begin{aligned}\boldsymbol{\sigma}^{tr'} &= \boldsymbol{\sigma}^{tr} - K\ tr(\boldsymbol{\varepsilon}_{t}^{e} + \Delta\boldsymbol{\varepsilon} - \Delta\boldsymbol{\varepsilon}^{p})\boldsymbol{I} \\ &= \boldsymbol{\sigma}^{tr} - K\ tr(\boldsymbol{\varepsilon}^{e})\boldsymbol{I} \\ &= \boldsymbol{\sigma}^{tr} - \frac{1}{3}(\boldsymbol{\sigma} : \boldsymbol{I})\boldsymbol{I}\end{aligned} \tag{3.37}$$

From Eq. (3.35), we have

$$\boldsymbol{\sigma}' + \frac{1}{3}(\boldsymbol{\sigma} : \boldsymbol{I})\boldsymbol{I} = \boldsymbol{\sigma}^{tr} - 3G\Delta\varepsilon_{eff}^{p}\frac{\boldsymbol{\sigma}'}{\sigma_{e}} \tag{3.38}$$

or

$$\boldsymbol{\sigma}^{tr} - \frac{1}{3}(\boldsymbol{\sigma} : \boldsymbol{I})\boldsymbol{I} = (1 + 3G\frac{\Delta\varepsilon_{eff}^{p}}{\sigma_{e}})\boldsymbol{\sigma}' \tag{3.39}$$

Therefore,

$$\boldsymbol{\sigma}^{tr'} = (1 + 3G\frac{\Delta\varepsilon_{eff}^{p}}{\sigma_{e}})\boldsymbol{\sigma}' \tag{3.40}$$

The trial value of the von Mises stress is then computed by

$$\begin{aligned}\sigma_{e}^{tr} &= \sqrt{\frac{3}{2}\boldsymbol{\sigma}^{tr'} : \boldsymbol{\sigma}^{tr'}} \\ &= (1 + 3G\frac{\Delta\varepsilon_{eff}^{p}}{\sigma_{e}})\sqrt{\frac{3}{2}\boldsymbol{\sigma}' : \boldsymbol{\sigma}'} \\ &= \sigma_{e} + 3G\Delta\varepsilon_{eff}^{p}\end{aligned} \tag{3.41}$$

The yield surface based on the trial values at time instant $t+\Delta t$ is given by

$$f = \boldsymbol{\sigma}_{e} - \sigma_{y} = \boldsymbol{\sigma}_{e}^{tr'} - 3G\Delta\varepsilon_{eff}^{p} - \sigma_{y} = 0 \tag{3.42}$$

Eq. (3.42) is a nonlinear equation in which $\Delta\varepsilon_{eff}^{p}$ is solved implicitly until equilibrium is reached.

3.3 LS-DYNA Built-in Material Models for Foams

LS-DYNA has several material models that can be used for foams. In this section, the yield criteria, evolution of the yield surface, and plastic flow rules of five models are introduced along with brief discussions of the capabilities of these models.

3.3.1 MAT 5: Soil and Crushable Foam Model

This model is recommended for use on soils and foams when confined within structural or geometric boundaries. The yield function of this model is given by

$$f = \sigma_e - \sqrt{3(a_0 + a_1 p + a_2 p^2)} = 0 \tag{3.43}$$

where σ_e is the von Mises stress, p is the mean stress/pressure, and a_0, a_1 and a_2 are material constants. As illustrated in FIGURE 3.4, if $a_1 = a_2 = 0$, the material will have no pressure dependency. In the principal stress space, the yield surface is a cylinder, which becomes a straight line in the pressure-von Mises stress space (a_0 = constant). If $a_2 = 0$, the yield surface is an inclined line in the pressure-von Mises stress space. If none of a_0, a_1 or a_2 is zero, the yield surface is a parabola in the pressure-von Mises stress space.

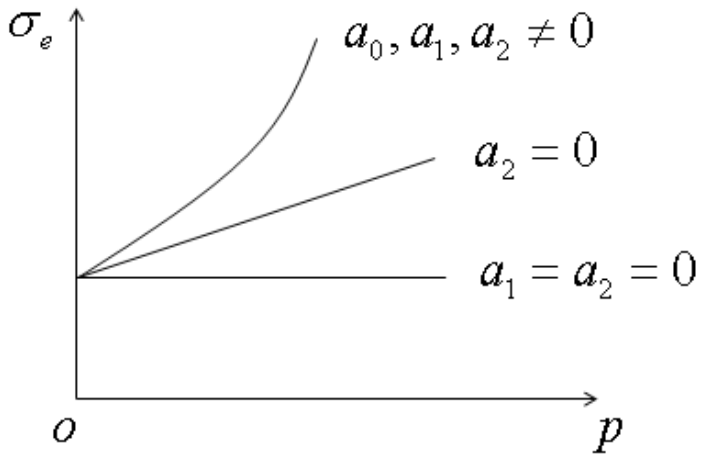

FIGURE 3.4: Yield surfaces in the hydrostatic pressure-von Mises stress space

The volumetric and deviatoric parts are considered separately in the formulation of this model. The yield function of the volumetric plasticity is given by

$$f_V = P - Y_P(\varepsilon_V) \tag{3.44}$$

where P is the current pressure and Y_p is the predefined volumetric yield stress. The deviatoric stress is computed afterwards using the aforementioned radial return method.

MAT 5 does not have the capability of handling material failure. A similar model to MAT 5 in LS-DYNA is MAT 14; it is the same as MAT 5 except that it allows defining a failure pressure beyond which an element loses its ability to carry tensile loads.

3.3.2 MAT 26: Anisotropic Honeycomb Model

This model is intended for use on anisotropic honeycomb and foam materials. Normal and shear behaviors are fully uncoupled and need to be defined separately. When an element's stresses are updated, the absolute value of each stress component is compared to the yield stress based on the following yield criterion:

$$f_{ij} = \left|\sigma_{ij}\right| - Y_{ij} = 0 \tag{3.45}$$

where the yield stresses Y_{ij} are predefined and provided by the user in piecewise linear curves of engineering volumetric strains

$$Y_{ij} = Y_{ij}^0 + H(\varepsilon_V) \tag{3.46}$$

Elastic-perfectly plastic behavior is assumed after full compaction when a predefined relative volume is reached. The von Mises stress is updated using the radial return method, and the mean stress is updated using the volumetric strain at time instant $t + \frac{1}{2}\Delta t$.

Similar to MAT 26, material model MAT 126 can also be used for honeycomb materials and crushable foams with anisotropic material properties. MAT 126 is essentially the same as MAT 26 except that strain hardening in MAT 126 depends on the associated engineering strain components ε_{ij}, thus

$$Y_{ij} = Y_{ij}^{0} + H(\varepsilon_{ij}) \tag{3.47}$$

The application of MAT 126 is restricted by the uncoupled consideration of the constitutive behaviors.

3.3.3 MAT 63: Isotropic Crushable Foam Model

Material yielding in this model is determined based on the principal stresses given as follows:

$$\sigma_{ij} = \begin{bmatrix} \sigma_1 & 0 & 0 \\ 0 & \sigma_2 & 0 \\ 0 & 0 & \sigma_3 \end{bmatrix} \tag{3.48}$$

Shaw and Sata (1966) suggested that the maximum principal stress be used to determine yielding with the yield function written as

$$f = \sigma_i^{\max} - Y = 0 \tag{3.49}$$

where the yield stress Y is defined in compression by

$$Y = Y^{0} + H(\varepsilon_V) \tag{3.50}$$

where the strain hardening $H(\varepsilon_V)$ is defined by the user with a piecewise stress-strain curve (either engineering volumetric strain or logarithmic/true volumetric strain). In tension no strain hardening is considered and the yield stress is defined by

$$Y = Y_t^{0} \tag{3.51}$$

After initial yielding in tension, the material is treated as perfectly plastic. Another assumption made in this material model is that Young's modulus is a constant and does not vary with deformation. Although this model is easy to formulate mathematically; numerical instabilities and inaccuracies have been observed in crash simulations when large deformations occur.

An extension of MAT 63 is the material model MAT 163, which considers strain-rate effects and includes both volumetric strain and strain-rate in the yield function

$$Y = Y^0 + H(\varepsilon_V, \dot{\varepsilon}_V) \tag{3.52}$$

A set of stress-strain curves needs to be defined for different strain-rates. The stress strain behavior is interpolated from the two bounding curves with the closest strain-rates.

3.3.4 MAT 75: Bilkhu/Dubois Foam Model

This is a pressure dependent model intended for use on isotropic crushable foams. The yield surface is an ellipse in the hydrostatic pressure-von Mises stress space, given as follows:

$$f = \left(\frac{p - \frac{1}{2}(p_c - p_t)}{a} \right)^2 + \left(\frac{\sigma_e}{b} \right)^2 - 1 = 0 \tag{3.53}$$

where a and b are the half lengths of the major and minor axes. A constant ratio is maintained between a and b during the expansion of the yield surface. The center of the ellipse is located at $\left(\frac{1}{2}(p_c - p_t), 0 \right)$, where p_c and p_t are the compressive and tensile yield hydrostatic pressures, respectively. Strain hardening is formulated by

$$p_c = p_c^0 + H_p(\varepsilon_V) \tag{3.54}$$

$$p_t = \frac{1}{10} p_c \tag{3.55}$$

$$Y = Y^0 + H(\varepsilon_V) \tag{3.56}$$

3.3.5 MAT 154: Deshpande and Fleck Foam Model

Similar to MAT 75, this material model is also pressure dependent and intended for use on isotropic metallic foams. Both the pressure and von Mises stress are used to determine yielding. The yield surface is an ellipse in the hydrostatic pressure-von Mises stress space where

$$f = \hat{\sigma} - Y = 0 \tag{3.57}$$

and $\hat{\sigma}$ is the equivalent stress defined as

$$\hat{\sigma} = \left[\frac{1}{1+(\alpha/3)^2} \left(\sigma_e^2 + \alpha^2 \sigma_m^2 \right) \right]^{\frac{1}{2}} \tag{3.58}$$

where σ_e is the von Mises stress given by Eq. (3.6) and σ_m is the mean stress given by Eq. (3.2). The yield function can then be expressed as

$$\frac{1}{1+(\alpha/3)^2} \left(\sigma_e^2 + \alpha^2 \sigma_m^2 \right) - Y^2 = 0 \tag{3.59}$$

or

$$\frac{(\frac{\sigma_e}{Y})^2}{(\sqrt{1+(\alpha/3)^2})^2} + \frac{(\frac{\sigma_m}{Y})^2}{(\frac{1}{\alpha}\sqrt{1+(\alpha/3)^2})^2} = 1 \tag{3.60}$$

The above equation shows that the uniaxial yield stress is equal to Y both in tension or compression; the hydrostatic yield stress is equal to $\frac{1}{\alpha}\sqrt{1+(\alpha/3)^2}\,Y$. FIGURE 3.5 shows the yield surfaces corresponding to different values of α, which is a shape

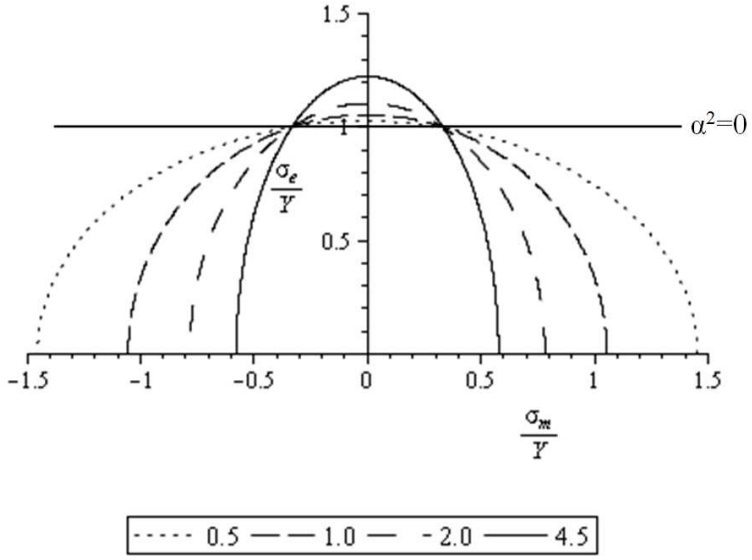

FIGURE 3.5: Yield surfaces with different values of α^2

factor defining the aspect ratio of the elliptic yield surface. For $\alpha = 0$, the yield criterion becomes the von Mises yield criterion defining the material as completely incompressible. When $\alpha^2 = 4.5$, the material is fully compressible. If the shape factor is chosen appropriately, the material behavior will match well to the experimental data (Deshpande and Fleck 2000).

If α remains constant, the yield surface during evolution will be geometrically self-similar; that is, the aspect ratio of the elliptic yield surface remains constant. The shape factor α can be related to the plastic Poisson's ratio ν^p under uniaxial compression in direction-3 as

$$\nu^p = -\frac{\dot{\varepsilon}^p_{11}}{\dot{\varepsilon}^p_{33}} = \frac{1/2 - (\alpha/3)^2}{1 + (\alpha/3)^2} \tag{3.61}$$

The shape factor and the aspect ratio of the yield surface can then be determined by measuring v^p. In this model, the plastic Poisson's ratio is kept constant due to the choice of a constant value of α during the process of plastic deformation.

3.3.6 MAT 193: Drucker-Prager Model

The Drucker-Prager yield criterion is commonly used on rock, concrete, polymer and foam materials. The Drucker-Prager yield surface is given by

$$f = \sqrt{J_2} + \alpha I_1 - k = 0 \tag{3.62}$$

where α and k are material constants, I_1 is the first stress invariant, and J_2 is the second stress invariant. In the principal stress space, the yield surface is a right-circular cone with its longitudinal axis equally inclined with respect to each principal stress axis and its apex in the tension octant (FIGURE 3.6). The drawback of this model is that the proposed yield surface does not represent well the yield surface of metallic foams.

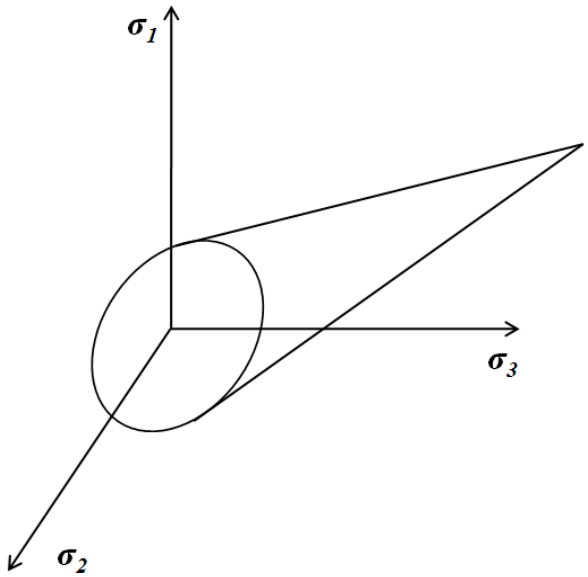

FIGURE 3.6: Drucker-Prager yield surface in the principal stress space

3.4 Constitutive Models for Foams

3.4.1 Deshpande and Fleck Models

Deshpande and Fleck (2000) developed two pressure-dependent foam models by investigating a range of axisymmetric compressive stress states of two types of aluminum foams, the Alporas and Duocel foams. They found that the yield surface could be represented by quadratic functions in the hydrostatic pressure-von Mises stress space. Based on experimental data, they proposed a self-similar hardening and a differential hardening model for metallic foams. In these two models the asymmetry in shape about the von Mises stress axis was neglected based on findings by Harte et al. (1999) and Gioux et al. (2000) that the tensile and compressive yield stresses were approximately the same in the experiments (FIGURE 3.7).

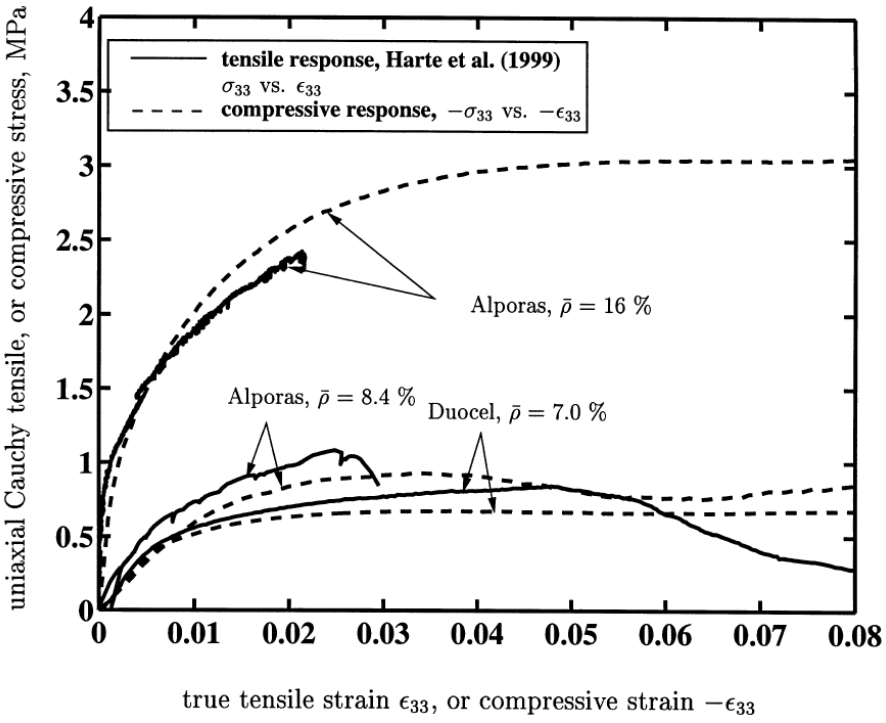

FIGURE 3.7: Comparison of stresses under uniaxial loading tests (Deshpande and Fleck 2000)

3.4.1.1 Self-similar hardening model

The yield function of the self-similar hardening model is given by Eq. (3.59) or (3.60). The initial yield surface could fit the experimental data well with a properly chosen value of the plastic Poisson's ratio or the shape factor α. This model adopts the associated flow rule that assumes the plastic strain-rate is normal to the yield surface. This is given by

$$\dot{\varepsilon}_{ij}^{p} = \frac{1}{H}\frac{\partial f}{\partial \sigma_{ij}}\frac{\partial f}{\partial \sigma_{kl}}\breve{\sigma}_{kl} \tag{3.63}$$

where $\dot{\varepsilon}_{ij}^{p}$ is the plastic strain-rate, H is the hardening modulus; $\breve{\sigma}_{kl}$ is the Jaumann stress rate, and f is the yield function. This model requires a proper choice of the plastic Poisson's ratio as defined in Eq. (3.61). Deshpande and Fleck suggested that this value be obtained from uniaxial compressive tests by compressing a specimen to 20~30% true strain. Experimental data showed a general trend of large plastic Poisson's ratios for the high density foams (Deshpande and Fleck 2000).

The plastic work rate conjugate to the equivalent strain-rate is defined as

$$\hat{\sigma}\dot{\hat{\varepsilon}} = \sigma_{ij}\dot{\varepsilon}_{ij}^{p} \tag{3.64}$$

where $\hat{\sigma}$ is the equivalent stress and $\dot{\hat{\varepsilon}}$ is the equivalent strain-rate. The plastic work rate conjugate pairs allow the computation of the equivalent strain-rate. The equivalent strain-rate can be explicitly expressed in terms of the von Mises strain-rate and the mean strain-rate as follows:

$$\dot{\hat{\varepsilon}}^{2} = \left[1+\left(\frac{\alpha}{3}\right)^{2}\right]\left(\dot{\varepsilon}_{e}^{2}+\frac{1}{\alpha^{2}}\dot{\varepsilon}_{m}^{2}\right) \tag{3.65}$$

where the von Mises strain-rate is expressed as

$$\dot{\varepsilon}_e = \sqrt{\frac{2}{3}\dot{\varepsilon}_{ij}^{'p}\dot{\varepsilon}_{ij}^{'p}} = \frac{\dot{\hat{\varepsilon}}}{\left[1+(\alpha/3)^2\right]}\frac{\sigma_e}{\hat{\sigma}} \tag{3.66}$$

and the mean strain-rate is expressed as

$$\dot{\varepsilon}_e = \dot{\varepsilon}_{kk}^{p} = \frac{\alpha^2\dot{\hat{\varepsilon}}}{\left[1+(\alpha/3)^2\right]}\frac{\sigma_m}{\hat{\sigma}} \tag{3.67}$$

The hardening modulus *H* can be determined from a series of experiments with hydrostatic and uniaxial compressive loading conditions that establish the hydrostatic and shear limits for the value of *H*. A simplified version of the self-similar model is to use the tangent modulus from a uniaxial compression test as the hardening modulus.

Acknowledging its merits of simplicity and ease of implementation, the self-similar hardening model does not predict material responses that are entirely consistent with experimental observations. For example, Gioux et al. (2000) found that, for low density Alporas foams, the predicted strength was lower than the measured values.

3.4.1.2 Differential hardening model

The differential hardening model was also proposed by Deshpande and Fleck (2000) in order to account for the non-similar evolution of the yield surface. In other words, this model allows the yield surface to change its shape in addition to its expansion during plastic deformation. With the hydrostatic and von Mises yield strengths evolving independently, the yield surface is defined as

$$f = \left(\frac{\sigma_e}{S}\right)^2 + \left(\frac{\sigma_m}{P}\right)^2 - 1 = 0 \tag{3.68}$$

where *S* is the von Mises yield strength and *P* is the hydrostatic yield strength. The hardening rule for this model is defined as

$$\begin{pmatrix} \dot{P} \\ \dot{S} \end{pmatrix} = \underset{\sim}{H} \begin{pmatrix} \dot{\varepsilon} \\ \dot{\gamma} \end{pmatrix} \tag{3.69}$$

where $\underset{\sim}{H}$ is the hardening matrix $\begin{pmatrix} h_{11} & h_{12} \\ h_{21} & h_{22} \end{pmatrix}$ that needs to be calibrated by material tests. In matrix $\underset{\sim}{H}$, h_{11} is the slope of hydrostatic pressure versus volumetric plastic strain, and h_{21} is the slope of shear stress versus volumetric plastic strain. Both h_{11} and h_{21} are obtained from the hydrostatic compression test and given as

$$h_{11} = \frac{\dot{\sigma}_m}{\dot{\varepsilon}_m} \tag{3.70}$$

$$h_{21} = \frac{\dot{S}}{\dot{\varepsilon}_m} \tag{3.71}$$

The differential hardening model assumes that there is a shear hardening during hydrostatic straining. For the other two parameters in $\underset{\sim}{H}$, h_{22} is the slope of shear stress versus effective plastic strain and h_{12} is the slope of hydrostatic pressure versus effective plastic strain, both are obtained from the shear test.

$$h_{22} = \frac{\dot{\sigma}_e}{\dot{\varepsilon}_e} \tag{3.72}$$

$$h_{12} = \frac{\dot{P}}{\dot{\varepsilon}_e} \tag{3.73}$$

In Eq. (3.69), $\dot{\varepsilon}$ and $\dot{\gamma}$ are the hydrostatic strain-rate and the shear strain-rate given as

$$\dot{\varepsilon} = \frac{\sigma_m}{P}\dot{\varepsilon}_m \tag{3.74}$$

$$\dot{\gamma} = \frac{\sigma_e}{S}\dot{\varepsilon}_e \tag{3.75}$$

which are the work rate conjugates of P and S, respectively. The work rate conjugate pairs are represented by

$$P\dot{\varepsilon} + S\dot{\gamma} = \sigma_m \dot{\varepsilon}_m + \sigma_e \dot{\varepsilon}_e = \sigma_{ij} \dot{\varepsilon}_{ij}^p \tag{3.76}$$

Substituting Eqs. (3.74) and (3.75) into the hardening rule (3.69), the hardening rule is written in the scalar form

$$\dot{P} = h_{11} \frac{\sigma_m}{P} \dot{\varepsilon}_m + h_{12} \frac{\sigma_e}{S} \dot{\varepsilon}_e \tag{3.77}$$

$$\dot{S} = h_{21} \frac{\sigma_m}{P} \dot{\varepsilon}_m + h_{22} \frac{\sigma_e}{S} \dot{\varepsilon}_e \tag{3.78}$$

From the associated flow rule (Eq. (3.63)), the strain-rates $\dot{\varepsilon}_m$ and $\dot{\varepsilon}_e$ can be written as

$$\dot{\varepsilon}_m = \frac{1}{H} \frac{\partial f}{\partial \sigma_m} \left(\frac{\partial f}{\partial \sigma_m} \dot{\sigma}_m + \frac{\partial f}{\partial \sigma_e} \dot{\sigma}_e \right) \tag{3.79}$$

$$\dot{\varepsilon}_e = \frac{1}{H} \frac{\partial f}{\partial \sigma_e} \left(\frac{\partial f}{\partial \sigma_m} \dot{\sigma}_m + \frac{\partial f}{\partial \sigma_e} \dot{\sigma}_e \right) \tag{3.80}$$

which are further simplified to

$$\dot{\varepsilon}_m = \frac{4\sigma_m}{HP^2} \left(\frac{\sigma_e \dot{\sigma}_e}{S^2} + \frac{\sigma_m \dot{\sigma}_m}{P^2} \right) \tag{3.81}$$

$$\dot{\varepsilon}_e = \frac{4\sigma_e}{HP^2} \left(\frac{\sigma_e \dot{\sigma}_e}{S^2} + \frac{\sigma_m \dot{\sigma}_m}{P^2} \right) \tag{3.82}$$

The consistency condition is written as

$$\dot{f} = \frac{\partial f}{\partial \sigma_{kl}} \hat{\sigma}_{kl} + \frac{\partial f}{\partial S} \dot{S} + \frac{\partial f}{\partial P} \dot{P} = 0 \tag{3.83}$$

Substituting Eqs. (3.77), (3.78), (3.81), (3.82) into Eq. (3.83), the hardening modulus H can be obtained. The differential hardening model assumes that there is hydrostatic stress

hardening during von Mises strain accumulation. Due to the complexity of this model, it is difficult to determine the model parameters (e.g., the hardening matrix) using experimental data and, further, to efficiently implement it in FE codes.

3.4.2 The New Foam Model

3.4.2.1 Evolution of the yield surface

The Deshpande and Fleck model implemented in LS-DYNA (MAT 154) uses a constant value of α to specify the shape of the initial yield surface and assumes no shape change throughout the deformation process. However, the shape of the yield surface, which is related to material compressibility, does not retain its original shape for foam materials. High density or compressed foams are less compressible than low density or uncompressed foams due to foam densification caused by yielding and collapsing of the internal cells.

FIGURES 3.8 and 3.9 include the experimental data showing the evolution of the yield surface of low and high density Alporas foams under uniaxial and hydrostatic loading. It was observed from FIGURES 3.8 and 3.9 that axial strains cause the yield surface to expand (i.e., a change of size) without significant change of its shape. By contrast, hydrostatic strains cause the yield surface to change both its size and shape.

It was further observed that the yield surface corresponding to the lower density foam has more of a shape change than that for the higher density foam. All the above observations indicate that pressure dependency and compressibility should be included in the material model in order to correctly predict the behavior of foams.

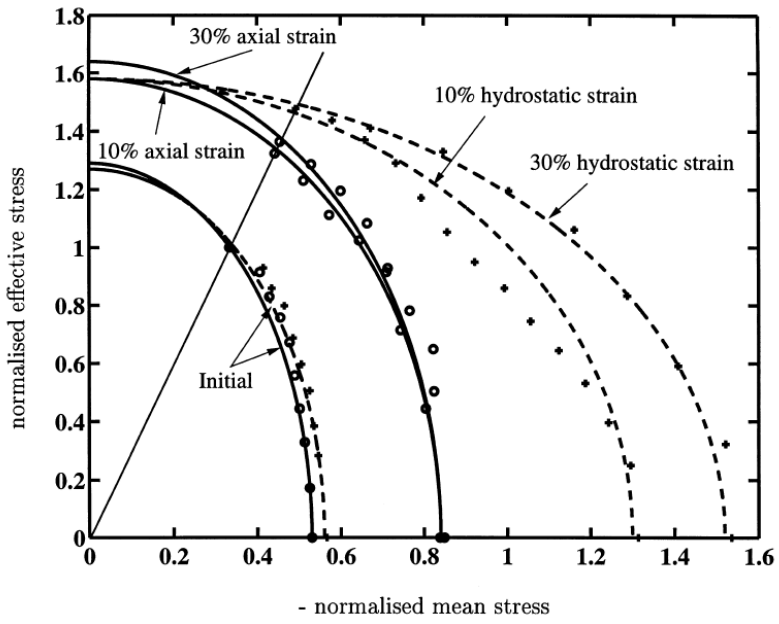

FIGURE 3.8: Evolution of the yield surface of 8.4% relative density foam (Deshpande and Fleck 2000)

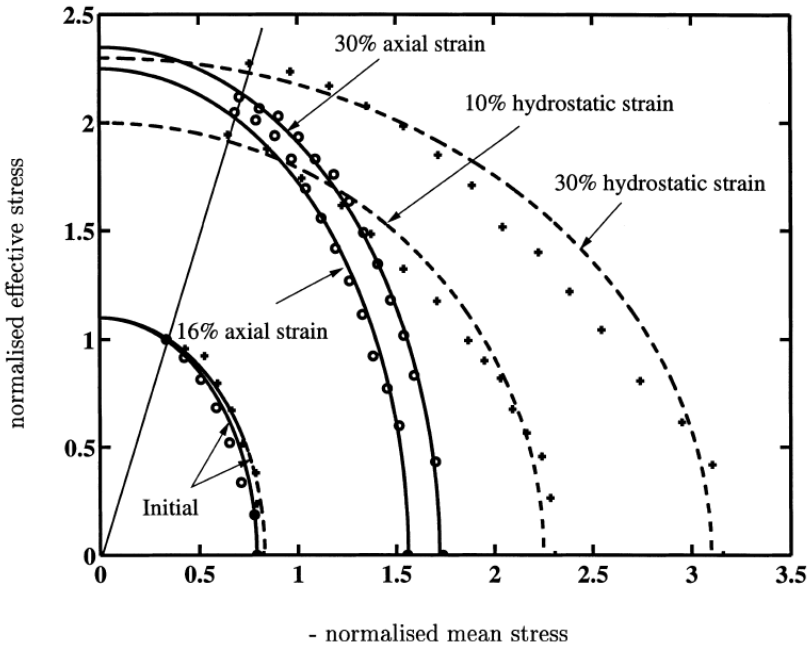

FIGURE 3.9: Evolution of the yield surface of 16% relative density foam (Deshpande and Fleck 2000)

3.4.2.2 Compressibility and plastic Poisson's ratio

In this section, the compressibility of metallic foams and the concept of the plastic Poisson's ratio are discussed. Certain materials, such as colloidal crystals and re-entrant polymer foams, have been found to exhibit negative Poisson's ratios. Greaves et al. (2011) investigated a number of modern materials and found the range of Poisson's ratio for the material examined range from -1 to 0.5. In this dissertation we only consider the metallic foam that has a positive Poisson's ratio. We start by examining the increment of the volumetric strain at time instant t

$$d\varepsilon_V = \frac{dV}{V} \tag{3.84}$$

For ease of discussion and implementation in FE codes, the incremental forms of Eq. (3.84) are used in the discussions hereafter. Let l, w and d be the length, width, and depth of a cuboid at time t; the volume of the cuboid is given by

$$V = lwd \tag{3.85}$$

Let Δl, Δw and Δd be the changes in length, breadth and depth at time instant (t+Δt), the new volume of the cuboid is then calculated by

$$\begin{aligned} V &= (l+\Delta l)(w+\Delta w)(d+\Delta d) \\ &= lwd + lw\Delta d + ld\Delta w + wd\Delta l + o(\Delta^2) \end{aligned} \tag{3.86}$$

Ignoring the second order terms in Eq. (3.86), the new volume is given by

$$V = lwd + lw\Delta d + ld\Delta w + wd\Delta l \tag{3.87}$$

and the volumetric change is

$$\Delta V = lw\Delta d + ld\Delta w + wd\Delta l \tag{3.88}$$

Using the incremental form of Eq. (3.84), the increment of volumetric strain during Δt is calculated as

$$\begin{aligned}\Delta\varepsilon_v &= \frac{\Delta V}{V} = \frac{lw\Delta d + ld\Delta w + wd\Delta l}{lwd} \\ &= \frac{\Delta l}{l} + \frac{\Delta w}{w} + \frac{\Delta d}{d} \\ &= \Delta\varepsilon_{xx} + \Delta\varepsilon_{yy} + \Delta\varepsilon_{zz}\end{aligned} \tag{3.89}$$

Deshpande and Fleck (2000) defined the plastic Poisson's ratio as

$$\nu^p = -\frac{\Delta\varepsilon_{xx}^p}{\Delta\varepsilon_{zz}^p} = -\frac{\Delta\varepsilon_{yy}^p}{\Delta\varepsilon_{zz}^p} \tag{3.90}$$

where the uniaxial loading is in the z-direction. Combining Eqs. (3.89) and (3.90), the increment of volumetric strain can be written in terms of the plastic Poisson's ratio and the plastic strain increment in the z-direction as

$$\begin{aligned}\Delta\varepsilon_v^p &= \Delta\varepsilon_{xx}^p + \Delta\varepsilon_{yy}^p + \Delta\varepsilon_{zz}^p \\ &= -\nu^p\Delta\varepsilon_{zz}^p - \nu^p\Delta\varepsilon_{zz}^p + \Delta\varepsilon_{zz}^p \\ &= (1-2\nu^p)\Delta\varepsilon_{zz}^p\end{aligned} \tag{3.91}$$

For a completely incompressible material, the increment of plastic volumetric strain is zero (i.e., no volume change). Therefore, for any values of plastic strain increment in the z-direction, Eq. (3.91) requires the following to hold

$$1-2\nu^p = 0 \tag{3.92}$$

where the plastic Poisson's ratio is found to be 0.5.

For fully compressible materials, there will be no expansion in the x- and y-direction. The increment of plastic volumetric strain is then expressed as

$$\Delta\varepsilon_v^p = \Delta\varepsilon_{xx}^p + \Delta\varepsilon_{yy}^p + \Delta\varepsilon_{zz}^p = \Delta\varepsilon_{zz}^p \tag{3.93}$$

Comparing Eq. (3.93) to Eq. (3.91), the plastic Poisson's ratio is determined to be zero. Therefore, from fully compressible to completely incompressible materials, the plastic Poisson's ratio ranges from 0 to 0.5. This suggests that, if the compressibility of the foam

changes during plastic deformation, the plastic Poisson's ratio (or a related material parameter) will also change and should be adjusted during the deformation process.

In the foregoing discussion, the second-order terms in Eq. (3.86) have been ignored in deriving the range of the plastic Poisson's ratio. To determine if the second-order terms will change the range of the plastic Poisson's ratio, the increment of volumetric strain is recalculated by including the second-order terms as

$$\begin{aligned}\Delta\varepsilon_v &= \frac{\Delta V}{V} = \frac{lw\Delta d + ld\Delta w + wd\Delta l + l\Delta w\Delta d + w\Delta l\Delta d + d\Delta l\Delta w}{lwd} \\ &= \frac{\Delta l}{l} + \frac{\Delta w}{w} + \frac{\Delta d}{d} + \frac{\Delta l}{l}\frac{\Delta w}{w} + \frac{\Delta l}{l}\frac{\Delta d}{d} + + \frac{\Delta w}{w}\frac{\Delta d}{d} \\ &= \Delta\varepsilon_{xx} + \Delta\varepsilon_{yy} + \Delta\varepsilon_{zz} + \Delta\varepsilon_{xx}\Delta\varepsilon_{yy} + \Delta\varepsilon_{xx}\Delta\varepsilon_{zz} + \Delta\varepsilon_{yy}\Delta\varepsilon_{zz}\end{aligned} \tag{3.94}$$

Substitute Eq. (3.90) into (3.94), the increment of volumetric strain can be expressed as

$$\begin{aligned}\Delta\varepsilon_v^p &= \Delta\varepsilon_{xx}^p + \Delta\varepsilon_{yy}^p + \Delta\varepsilon_{zz}^p + \Delta\varepsilon_{xx}^p\Delta\varepsilon_{yy}^p + \Delta\varepsilon_{xx}^p\Delta\varepsilon_{zz}^p + \Delta\varepsilon_{yy}^p\Delta\varepsilon_{zz}^p \\ &= (1-2\nu^p)\Delta\varepsilon_{zz}^p + \nu^p(\nu^p-2)(\Delta\varepsilon_{zz}^p)^2 + (\nu^p)^2(\Delta\varepsilon_{zz}^p)^3 \\ &= \Delta\varepsilon_{zz}^p\left\{\left[\Delta\varepsilon_{zz}^p + (\Delta\varepsilon_{zz}^p)^2\right](\nu^p)^2 - (2\Delta\varepsilon_{zz}^p + 2)\nu^p + 1\right\}\end{aligned} \tag{3.95}$$

For completely incompressible material the increment of volumetric strain is zero and the right-hand side of Eq. (3.95) becomes zero for arbitrary $\Delta\varepsilon_{zz}^p$. This leads to

$$\nu^p = \frac{(\Delta\varepsilon_{zz}^p + 1) - \sqrt{\Delta\varepsilon_{zz}^p + 1}}{\Delta\varepsilon_{zz}^p(\Delta\varepsilon_{zz}^p + 1)} \tag{3.96}$$

The characteristic strain-rates during automotive crash simulations are usually between the orders of magnitude 10^{-3} to 10^{3} sec^{-1}. This is equivalent to 10^{-9} *sec* to 10^{-3} *sec* per time-step when a simulation time-step of 10^{-6} *sec* is used. The limit of Eq. (3.96) when the strain increment goes to zero can be calculated as

$$\lim_{\Delta\varepsilon_{zz}^{p}\to 0} \nu^{p} = \lim_{\Delta\varepsilon_{zz}^{p}\to 0} \frac{(\Delta\varepsilon_{zz}^{p}+1)-\sqrt{\Delta\varepsilon_{zz}^{p}+1}}{\Delta\varepsilon_{zz}^{p}(\Delta\varepsilon_{zz}^{p}+1)}$$
$$= \lim_{\Delta\varepsilon_{zz}^{p}\to 0} \frac{1-\frac{1}{2}\left(\Delta\varepsilon_{zz}^{p}+1\right)^{-1/2}}{2\Delta\varepsilon_{zz}^{p}+1} \tag{3.97}$$
$$= 0.5$$

Eq. (3.96) is plotted in FIGURE 3.10 for strain-rates ranging from 0 to 10^3 sec^{-1} (Gassan and Harwick 2001). This figure shows the plastic Poisson's ratio as a function of the strain-rate with a simulation time-step of 10^{-6}. The plastic Poisson's ratio starts from 0.5 and slightly decreases when the strain-rate increases. However, it can be seen from FIGURE 3.10 that for characteristic strain-rate ranges, the plastic Poisson's ratio can be taken as 0.5 for completely incompressible materials.

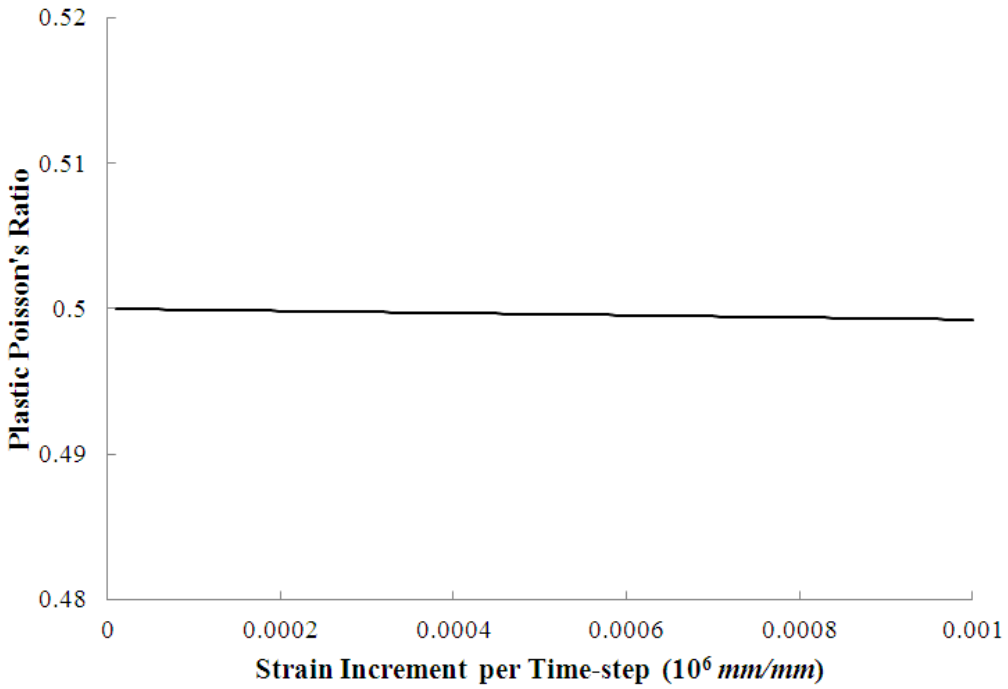

FIGURE 3.10: Plastic Poisson's ratio as a function of plastic strain increment

For fully compressible materials, the increment of plastic volumetric strain is expressed as

$$\Delta\varepsilon_v^p = \Delta\varepsilon_{zz}^p \tag{3.98}$$

Apply Eq. (3.98) to Eq. (3.95), we have

$$(1-2\nu^p)\Delta\varepsilon_{zz}^p + \nu^p(\nu^p-2)(\Delta\varepsilon_{zz}^p)^2 + (\nu^p)^2(\Delta\varepsilon_{zz}^p)^3 = \Delta\varepsilon_{zz}^p \tag{3.99}$$

where the plastic Poisson's ratio needs to be zero for arbitrary values of $\Delta\varepsilon_{zz}^p$. Therefore, the range of the plastic Poisson's ratio can be set from 0 to 0.5 in FE crash simulations, representing materials from fully compressible to fully incompressible.

3.4.2.3 Formulation of the new model

The yield function of the new form is defined as:

$$f = \hat{\sigma} - Y = \sqrt{\frac{1}{1+(\alpha/3)^2}\left(\sigma_e^2 + \alpha^2\sigma_m^2\right)} - Y = 0 \tag{3.100}$$

where $\hat{\sigma}$ is the equivalent stress, σ_e is the von Mises effective stress, and σ_m is the mean stress.

The flow potential *g* is defined to be the same as the yield function

$$g = \sqrt{\frac{1}{1+(\alpha/3)^2}\left(\sigma_e^2 + \alpha^2\sigma_m^2\right)} - Y \tag{3.101}$$

and the flow rule is given by

$$\dot{\boldsymbol{\varepsilon}}^p = \dot{\Lambda}\frac{\partial g}{\partial \boldsymbol{\sigma}} \tag{3.102}$$

where $\dot{\Lambda}$ is the plastic multiplier. Substituting Eq. (3.101) into Eq. (3.102), we obtain

$$\dot{\boldsymbol{\varepsilon}}^p = \dot{\Lambda}\frac{3}{2g}\frac{1}{1+(\alpha/3)^2}\left(\boldsymbol{\sigma}' + \frac{2\alpha^2}{9}\sigma_m\mathbf{I}\right) \tag{3.103}$$

which can be further decomposed into longitudinal and volumetric plastic strains as

$$\dot{\varepsilon}_{zz}^{p} = \dot{\Lambda}\frac{3}{2g}\frac{1}{1+(\alpha/3)^2}(\sigma_{zz}^{'} + \frac{2\alpha^2}{9}\sigma_m) \tag{3.104}$$

$$\dot{\varepsilon}_{v}^{p} = tr(\dot{\boldsymbol{\varepsilon}}^{p}) = \dot{\Lambda}\frac{1}{1+(\alpha/3)^2}\frac{\alpha^2\sigma_m}{g} \tag{3.105}$$

For uniaxial loading in z-direction, the longitudinal stress deviator can be calculated as

$$\sigma_{zz}^{'} = \sigma_{zz} - \sigma_m = 3\sigma_m - \sigma_m = 2\sigma_m \tag{3.106}$$

Now substitute Eqs. (3.104), (3.105) and (3.106) into Eq. (3.91), the shape factor of the yield surface is found to be related to the plastic Poisson's ratio

$$\alpha^2 = \frac{9(1-2\nu^p)}{2(1+\nu^p)} \tag{3.107}$$

The shape factor α^2 of the yield surface represents the material's compressibility; its value ranges from 0 to 4.5 for a feasible plastic Poisson's ratio, which ranges from 0.5 to 0. The yield surface of the new model appears similar to the Deshpande and Fleck self-similar model. However, the shape factor α^2 is no longer a constant value and changes with respect to the material's compressibility.

A relationship between the true volumetric strain and the shape factor needs to be established in order to dynamically adjust the value of α^2 based on the strain values during plastic deformation. Let A be the cross-sectional area of a prismatic block of metallic foam that has a density ρ_0 and length l_0 before deformation and a density ρ and length l after deformation. By conservation of mass and assuming no change in the cross-sectional area, we have

$$\rho_0 A l_0 = \rho A(l_0 - \Delta l) \tag{3.108}$$

or

$$\frac{\Delta l}{l_0} = \frac{\rho - \rho_0}{\rho} \tag{3.109}$$

The true volumetric strain is given by

$$\begin{aligned} \varepsilon_t &= \ln \frac{V}{V_0} \\ &= \ln \frac{l}{l_0} \\ &= \ln(1 - \frac{\Delta l}{l_0}) \end{aligned} \tag{3.110}$$

Combining Eqs. (3.109) and (3.110), we have

$$\varepsilon_t = \ln(\frac{\rho_0}{\rho}) \tag{3.111}$$

or

$$\rho = \rho_0 e^{-\varepsilon_t} \tag{3.112}$$

Equation (3.112) shows that the density grows exponentially with the true volumetric strain, as illustrated in FIGURE 3.11 for an initial material density of 0.23 g/cm^3.

Since the plastic Poisson's ratio is not a material property and is difficult to determine for its relationship to the material's compressibility, a linear relationship is assumed between the foam density and the plastic Poisson's ratio as follows:

$$\nu^p = \nu_0^p + \frac{\nu_{Al}^p - \nu_0^p}{\rho_{Al} - \rho_0}(\rho - \rho_0) \tag{3.113}$$

where ν_0^p is the initial plastic Poisson's ratio of the aluminum foam, ν_{Al}^p is the plastic Poisson's ratio of virgin aluminum, ρ_0 is the initial density of the aluminum foam, and ρ_{Al} is the density of virgin aluminum and ρ is the current foam density. Substituting Eq. (3.112) into Eq. (3.113), we obtain

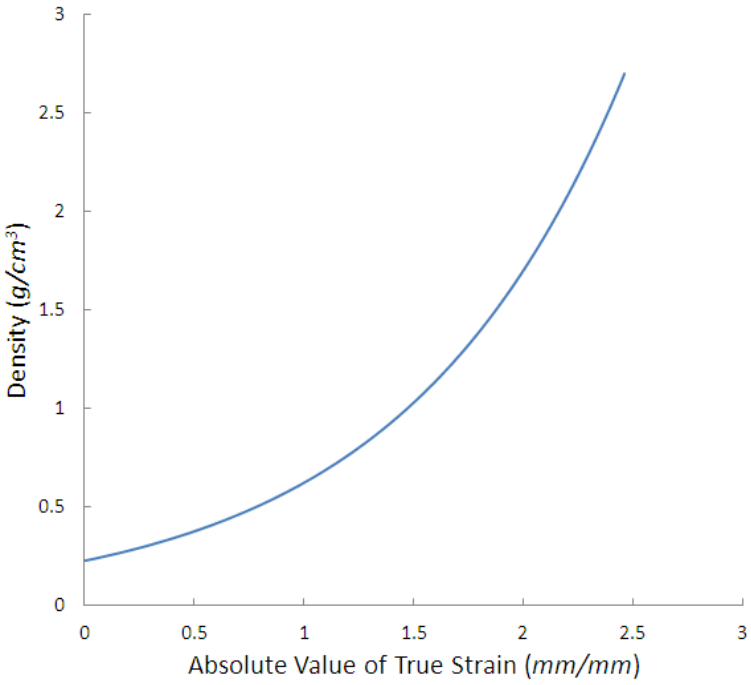

FIGURE 3.11: Density as a function of the absolute value of true strain

$$\nu^p = \nu_0^p + \frac{\nu_{Al}^p - \nu_0^p}{\rho_{Al} - \rho_0}\rho_0(e^{-\varepsilon_t} - 1) \tag{3.114}$$

which can be used in Eq. (3.107) to dynamically determine the shape factor α^2.

Assuming that a sample of aluminum foam has an initial density of 0.23 g/cm^3 and initial plastic Poisson's ratio of 0.01, and the fully densified aluminum foam has a density of 2.7 g/cm^3 (the same mechanical property as virgin aluminum) and a plastic Poisson's ratio of 0.5 (completely incompressible). The plastic Poisson's ratio of aluminum foam can then be written in terms of true strain as

$$\nu^p = 0.05e^{-\varepsilon_t} - 0.04 \tag{3.115}$$

This equation is plotted in FIGURE 3.12, and the shape factor is given by

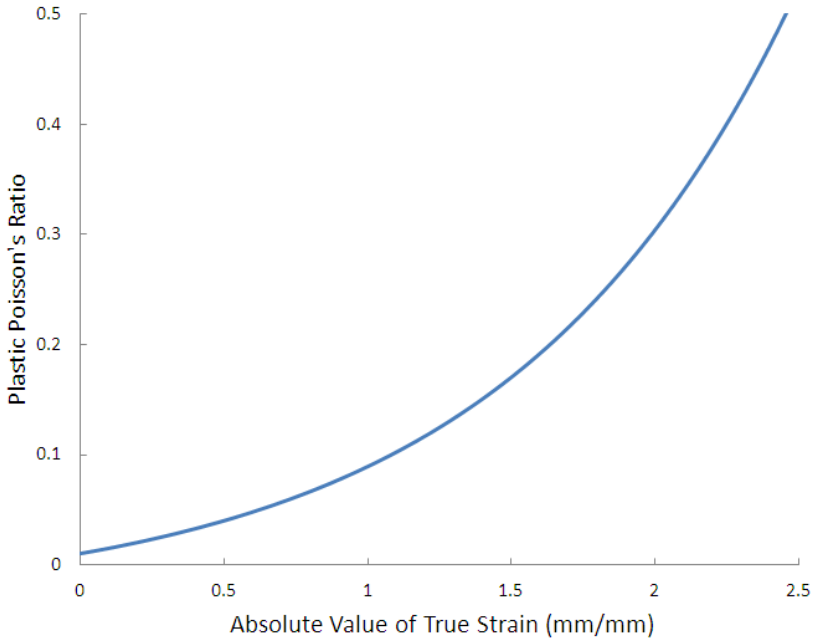

FIGURE 3.12: Exponential model of the plastic Poisson's ratio

$$\alpha^2 = \frac{9 - 18\nu_0^p - 18\rho_0 \dfrac{\nu_{Al}^p - \nu_0^p}{\rho_{Al} - \rho_0}(e^{-\varepsilon_t} - 1)}{2\nu_0^p + 2\rho_0 \dfrac{\nu_{Al}^p - \nu_0^p}{\rho_{Al} - \rho_0}(e^{-\varepsilon_t} - 1) + 2} \tag{3.116}$$

The shape factor is updated at each time-step in the FE simulations during hardening of the metallic foam. The shape of the yield surface will change with respect to material yielding and hardening.

Equation (3.114) is an exponential function with respect to the true strain. This will be referred to as the exponential model in the rest of this dissertation. For comparison purposes, a linear interpolation function of the plastic Poisson's ratio with respect to the true strain could be used to provide an alternative approximation, which will be referred to as the linear interpolation model in the rest of this dissertation. This model is given by

$$\nu^p = \nu_0^p + \frac{\nu_{Al}^p - \nu_0^p}{\ln \rho_0 - \ln \rho_{Al}} \varepsilon_t \tag{3.117}$$

With the same mechanical properties as those used to derive Eq. (3.115), the plastic Poisson's ratio of aluminum foam can be written

$$\nu^p = 0.01 - 0.20\varepsilon_t \tag{3.118}$$

This equation is plotted in FIGURE 3.13, and the shape factor is given by

$$\alpha^2 = \frac{8.82 - 3.60\varepsilon_t}{2.02 - 0.40\varepsilon_t} \tag{3.119}$$

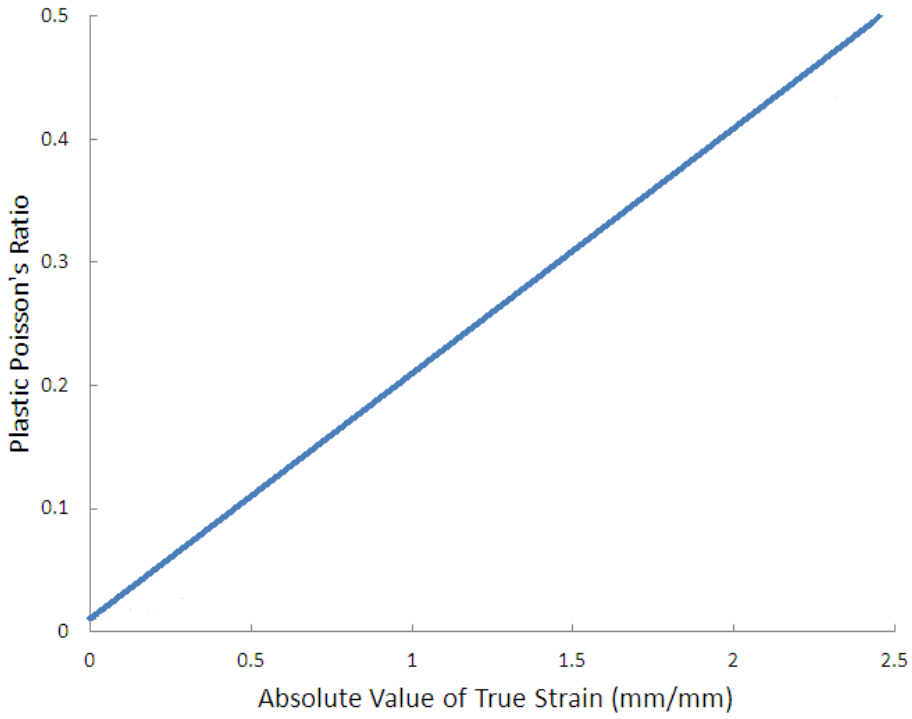

FIGURE 3.13: Linear interpolation model of the plastic Poisson's ratio

CHAPTER 4: FINITE ELEMENT IMPLEMENTATION

In nonlinear FEA, element stresses are calculated and updated incrementally in the general form of

$$\sigma_{ij}(t+dt) = \sigma_{ij}(t) + \dot{\sigma}_{ij}dt \tag{4.1}$$

where $\dot{\sigma}_{ij}$ is the derivative of the stress tensor with respect to time and is given by

$$\dot{\sigma}_{ij} = \breve{\sigma}_{ij} + \sigma_{ik}\omega_{kj} + \sigma_{jk}\omega_{ki} \tag{4.2}$$

In Eq. (4.2) $\breve{\sigma}_{ij}$ is the Jaumann (co-rotational) stress rate and ω_{ij} is the spin tensor, both given by

$$\breve{\sigma}_{ij} = C_{ijkl}\dot{\varepsilon}_{kl} \tag{4.3}$$

$$\omega_{ij} = \frac{1}{2}\left(\frac{\partial v_i}{\partial x_j} - \frac{\partial v_j}{\partial x_i}\right) \tag{4.4}$$

where C_{ijkl} is the stress-dependent constitutive matrix, v_i is the velocity vector, and $\dot{\varepsilon}_{ij}$ is the strain rate tensor given by

$$\dot{\varepsilon}_{ij} = \frac{1}{2}\left(\frac{\partial v_i}{\partial x_j} + \frac{\partial v_j}{\partial x_i}\right) \tag{4.5}$$

The numerical implementation of Eq. (4.1) can be briefly represented by the following equations:

$$\sigma_{ij}^{n+1} = \sigma_{ij}^{n} + r_{ij}^{n} + \breve{\sigma}_{ij}^{n+\frac{1}{2}}\Delta t^{n+\frac{1}{2}} \tag{4.6}$$

where

$$\breve{\sigma}_{ij}^{n+\frac{1}{2}}\Delta t^{n+\frac{1}{2}} = C_{ijkl}\Delta\varepsilon_{kl}^{n+\frac{1}{2}} \tag{4.7}$$

$$\Delta\varepsilon_{kl}^{n+\frac{1}{2}} = \dot{\varepsilon}_{ij}^{n+\frac{1}{2}}\Delta t^{n+\frac{1}{2}} \tag{4.8}$$

$$r_{ij}^{n} = (\sigma_{ip}^{n}\omega_{pj}^{n+\frac{1}{2}} + \sigma_{jp}^{n}\omega_{pi}^{n+\frac{1}{2}})\Delta t^{n+\frac{1}{2}} \tag{4.9}$$

where r_{ij}^{n} is the rotation of the stress tensor at time instant t^n.

In a user-defined material subroutine (UMAT), the stress rotation in Eq. (4.2), i.e., $\left(\sigma_{ik}\omega_{kj} + \sigma_{jk}\omega_{ki}\right)$, is first calculated by LS-DYNA in order to perform the stress update in Eq. (4.1). The UMAT, which contains the users' own constitutive models and is linked to LS-DYNA at run time, is then called to add the incremental stress components (the Jaumann stress rate $\breve{\sigma}_{ij}$).

4.1 User Material Subroutine in LS-DYNA

In LS-DYNA ver. 971, user subroutines are provided in an interface file named dyn21.f, a FORTRAN program (LSTC 2010). In LS-DYNA MPP ver. 971, which was used in the work of this dissertation, up to ten subroutines can be implemented simultaneously. A bulk modulus and shear modulus must be defined in each material subroutine; their values are used for contact interfaces, rigid body constraints and calculation of time-step sizes carried out by the LS-DYNA main program. For example, the bulk modulus must be used in the calculation of contact stiffness given by Eq. (2.4).

The new material model was implemented by modifying the source code of the standard template file provided by LSTC. The UMAT was compiled and an LS-DYNA runtime library was created with file name "libmpp971_d_7600.2.1224_usermat.so" using the 'makefile' given in Appendix A. The procedure to build and use a UMAT in

LS-DYNA is outlined below.

1. Download the required Object files from LS-DYNA ftp site (ftp://ftp.lstc.com).

   User name: Objects

   Password: computer1

2. Open the "dyn21.f" file with a text editor, search for "umat41" and comment out this subroutine.
3. Create the new subroutine with name "umat41" and save the source code in a separate file with extension of ".f". At time instant t, the six local strain increments and the six current stress components are known. By integrating the constitutive equations, the six new stress components at time instant $t+\Delta t$ will be obtained at the end of the subroutine.
4. Use the "make" command to compile and create an LS-DYNA runtime library with file name "libmpp971_d_7600.2.1224_usermat.so".
5. Change the library path of LS-DYNA to where the new library file is located.
6. Call the material ID from the keyword deck, i.e., use MAT 041 in the keyword file.

4.2 Implementation of the New Foam Model

The flow of the material subroutine includes several major steps. The shape factor and yield stress of the current yield surface are first calculated based on the current total plastic strains. Given the current stress components and increments of strain components, the material subroutine calculates a trial stress and its deviator using the elastic properties of the material. A trial value of the equivalent stress is then calculated and compared with the current yield stress. If the material has not yielded, the trial stresses are adopted to

replace the current stresses. If the material has yielded, the subroutine enters a loop to implicitly solve for the strain increments that satisfy the constitutive equations for the next time-step until the pre-defined convergence criteria are reached. The solutions are then used to update the stress components. The history variables such as the total volumetric strain, total equivalent strain, hydrostatic pressure, and von Mises stress, are all updated for use in the next time-step. The following subsections give details of how the constitutive equations are formulated and integrated.

4.2.1 Formulation of Constitutive Equations

The constitutive model includes two major equations: one for the yield surface and the other for the flow rule. This section presents how these equations are formulated, how the number of primary unknowns is reduced, and how the stresses are updated using solutions of the primary unknowns.

The equation of the yield surface is given by Eq. (3.100), which includes both the hydrostatic pressure σ_m and the von Mises stress σ_e. For ease of discussion, the hydrostatic pressure is written as p and the von Mises stress is written as q hereafter; and the yield surface in terms of p and q at time instant $t+\Delta t$ is given by

$$f(p,q)_{t+\Delta t} = \hat{\sigma}(p,q)_{t+\Delta t} - Y(p,q)_{t+\Delta t} = 0 \tag{4.10}$$

The flow rule is defined in the differential form by

$$d\boldsymbol{\varepsilon}^p = d\Lambda \frac{\partial g}{\partial \boldsymbol{\sigma}} \tag{4.11}$$

where $g = g(p,q)$ is the flow potential, $d\Lambda$ is a positive scalar standing for the magnitude of the plastic strain rate. The flow rule can be further represented using the chain rule as

$$
\begin{aligned}
d\boldsymbol{\varepsilon}^p &= d\Lambda\left(\frac{\partial g}{\partial p}\frac{\partial p}{\partial \boldsymbol{\sigma}}+\frac{\partial g}{\partial q}\frac{\partial q}{\partial \boldsymbol{\sigma}}\right) \\
&= d\Lambda\left(-\frac{1}{3}\frac{\partial g}{\partial p}\mathbf{I}+\frac{\partial g}{\partial q}\mathbf{n}\right)
\end{aligned}
\tag{4.12}
$$

The incremental form of Eq. (4.12) is given by

$$
\Delta\boldsymbol{\varepsilon}^p = \frac{1}{3}\Delta\varepsilon_p\mathbf{I}+\Delta\varepsilon_q\mathbf{n}_{t+\Delta t} \tag{4.13}
$$

where

$$
\Delta\varepsilon_p = -\Delta\Lambda\left(\frac{\partial g}{\partial p}\right)_{t+\Delta t} \tag{4.14}
$$

$$
\Delta\varepsilon_q = \Delta\Lambda\left(\frac{\partial g}{\partial q}\right)_{t+\Delta t} \tag{4.15}
$$

$$
\mathbf{n} = \frac{3}{2q}\boldsymbol{\sigma}' \tag{4.16}
$$

Combining Eqs. (4.14) and (4.15) and eliminating $\Delta\Lambda$, we obtain

$$
\Delta\varepsilon_p\left(\frac{\partial g}{\partial q}\right)_{t+\Delta t}+\Delta\varepsilon_q\left(\frac{\partial g}{\partial p}\right)_{t+\Delta t}=0 \tag{4.17}
$$

Equations (4.10) and (4.17) are the two constitutive equations to be solved at each time step. There are two primary unknowns: $\Delta\varepsilon_p$ and $\Delta\varepsilon_q$. Combining Eqs. (4.17) and (3.8), we obtain the formula for updating the stresses at the end of the subroutine using the solutions of the two primary unknowns.

$$
\boldsymbol{\sigma}_{t+\Delta t} = \sigma^e - K\Delta\varepsilon_p\mathbf{I}+-2G\Delta\varepsilon_q\mathbf{n}_{t+\Delta t} \tag{4.18}
$$

where

$$
\mathbf{n}_{t+\Delta t} = \frac{3}{2q^e}\boldsymbol{\sigma}'^e \tag{4.19}
$$

4.2.2 Integration of Constitutive Equations

In FEA, the integration of constitutive equations is carried out at the integration points at each time-step. At time instant *t*, the local strain increments are given, and the integration of the constitutive equations gives the values of the plastic strain increments which are then used to update the stresses and state variables at time instant $t+\Delta t$. The stresses are then used for the next time-step, and this procedure continues. In this dissertation, the integration of constitutive equations was carried out by the backward Euler method, which is unconditionally stable, to ensure the stability of the integration algorithm.

Using equations of the yield surface and flow potential, given by Eqs. (3.100) and (3.101), respectively, Eqs. (4.10) and (4.17) can be represented by the following system of nonlinear equations with the two renamed as F_1 and F_2, respectively.

$$F_1 = \sqrt{\frac{1}{1+(\alpha/3)^2}\left(q^2+\alpha^2 p^2\right)}_{t+\Delta t} - Y_{t+\Delta t} = 0 \tag{4.20}$$

$$F_2 = \Delta\varepsilon_p \left(\frac{1}{1+(\alpha/3)^2}\frac{q}{\hat{\sigma}}\right)_{t+\Delta t} + \Delta\varepsilon_q \left(\frac{\alpha^2}{1+(\alpha/3)^2}\frac{p}{\hat{\sigma}}\right)_{t+\Delta t} = 0 \tag{4.21}$$

In the above equations, $\Delta\varepsilon_p$ and $\Delta\varepsilon_q$ are the primary unknowns to be solved. Let *cp* and *cq* be the increments of $\Delta\varepsilon_p$ and $\Delta\varepsilon_q$; the system of equations can be linearized and solved iteratively by the Newton-Raphson Method. This method is illustrated as follows.

For a system of two nonlinear equations

$$F_i(\mathbf{x}) = 0 \qquad i = 1, 2. \tag{4.22}$$

where **x** denotes the vector of unknowns (i.e., *p* and *q* in the work of this dissertation). F_i can be expanded by Taylor series in the neighborhood of **x** as

$$F_i(\mathbf{x}+\delta\mathbf{x}) = F_i(\mathbf{x}) + \sum_{j=1}^{N} \frac{\partial F_i}{\partial x_j}\delta x_j + O(\delta\mathbf{x}^2) \tag{4.23}$$

where $\frac{\partial F_i}{\partial x_j}$ is the Jacobian matrix denoted by **J**. Equation (4.23) can be rewritten as

$$\mathbf{F}(\mathbf{x}+\delta\mathbf{x}) = \mathbf{F}(\mathbf{x}) + \mathbf{J}\cdot\delta\mathbf{x} + O(\delta\mathbf{x}^2) \tag{4.24}$$

Neglecting the high-order terms and setting $\mathbf{F}(\mathbf{x}+\delta\mathbf{x}) = 0$, the system of nonlinear equations is converted into a set of linear equations given by

$$\mathbf{J}\cdot\delta\mathbf{x} = -\mathbf{F} \tag{4.25}$$

Substituting Eqs. (4.20) and (4.21) into Eq. (4.25), we obtain the system of linear equations at the *n*-th iteration as

$$\begin{bmatrix} \frac{\partial F_1}{\partial p} & \frac{\partial F_1}{\partial q} \\ \frac{\partial F_2}{\partial p} & \frac{\partial F_2}{\partial q} \end{bmatrix}^{(n)} \cdot \begin{Bmatrix} cp \\ cq \end{Bmatrix} = - \begin{Bmatrix} F_1 \\ F_2 \end{Bmatrix}^{(n)} \tag{4.26}$$

With pre-defined initial values of p, q, $\Delta\varepsilon_p$ and $\Delta\varepsilon_q$, cp and cq can be calculated using methods such as Gaussian elimination or LU decomposition. The values of $\Delta\varepsilon_p$ and $\Delta\varepsilon_q$ are then updated by

$$\Delta\varepsilon_p^{(n+1)} = \Delta\varepsilon_p^{(n)} + cp \tag{4.27}$$

$$\Delta\varepsilon_q^{(n+1)} = \Delta\varepsilon_q^{(n)} + cq \tag{4.28}$$

The values of p and q are subsequently updated by

$$p^{(n+1)} = p^{(n)} + k\Delta\varepsilon_p \tag{4.29}$$

$$q^{(n+1)} = q^{(n)} - 3g\Delta\varepsilon_q \tag{4.30}$$

The new values of p, q, $\Delta\varepsilon_p$ and $\Delta\varepsilon_q$ are used in the next iteration to calculate the new

values of *cp* and *cq*. This procedure is repeated until the prescribed convergence criteria are reached.

4.3 Model Verification

Model verification ensures that the numerical algorithms are correctly implemented in the material subroutine, have good convergence, and produce accurate solutions of the mathematical models. In the verification process, the numerical simulation results are usually compared with analytical solutions. Due to the complexity of the constitutive model, it is very difficult to obtain an analytical solution for metallic foam, especially with complicated boundary and loading conditions. In this research, the new foam model is verified using LS-DYNA's built-in material model, MAT 154, by setting the shape factor to the same constants in both models. Verification of the user subroutine was performed using a uniaxial compression test on a single eight-node solid element as shown in FIGURE 4.1.

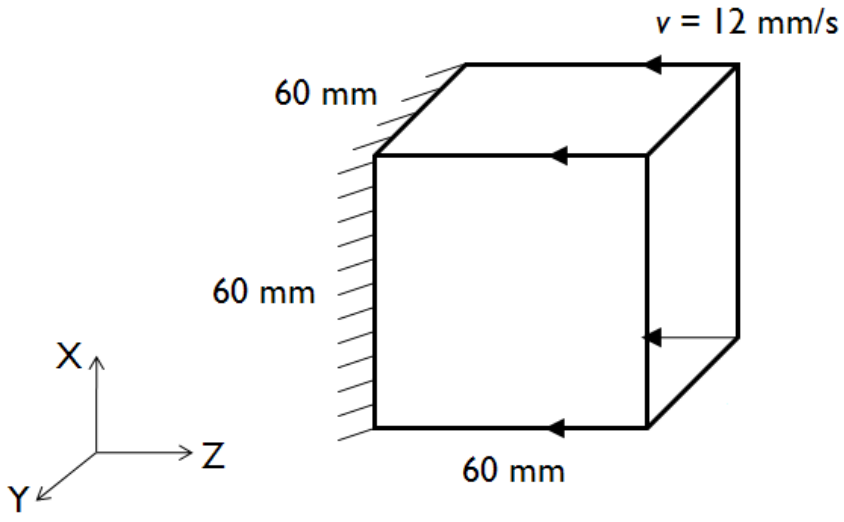

FIGURE 4.1: Boundary and loading conditions of the verification test

The solid element is used to model a 60-*mm* cube of aluminum foam. One side of the element is fixed for all three degrees of freedom, and nodes on the opposite side have a prescribed velocity of 12 *mm/s* towards the fixed side. The density of the foam is 0.47 g/cm^3. The same stress-strain curve, shown in FIGURE 4.2, is used for both the new foam model and LS-DYNA MAT 154. Two constant values of the shape factors were tested, $\alpha^2 = 0.25$ and $\alpha^2 = 4.5$, corresponding to nearly incompressible ($\nu^p \approx 0.5$) and fully compressible ($\nu^p = 0$) materials, respectively.

The solid element with selective reduced integration was used. This element formulation assumes a constant pressure through the element to avoid pressure locking during near incompressible flow. Pressure locking arises when the material is incompressible and displacements calculated by the FE method are orders of magnitude smaller than they should be. It typically occurs in lower order elements because element kinematics is not precise enough to represent the correct solution. The fully integrated element formulation was found to be unstable in simulations involving large deformations and distortions due to a negative Jacobian at one of the integration points despite of the positive volume of the entire element.

4.3.1 Nearly incompressible foam

In this test the shape factor was set to a constant value of $\alpha^2 = 0.25$, representing a nearly incompressible condition ($\nu^p \approx 0.5$) in which the foam element is expected to expand in the *x*- and *y*- directions under *z*-direction loading. The element was compressed for 54 *mm* in 4.5 seconds at a constant speed of 12 *mm/s*. FIGURE 4.2 shows the true stress-strain input for the foam in this verification test.

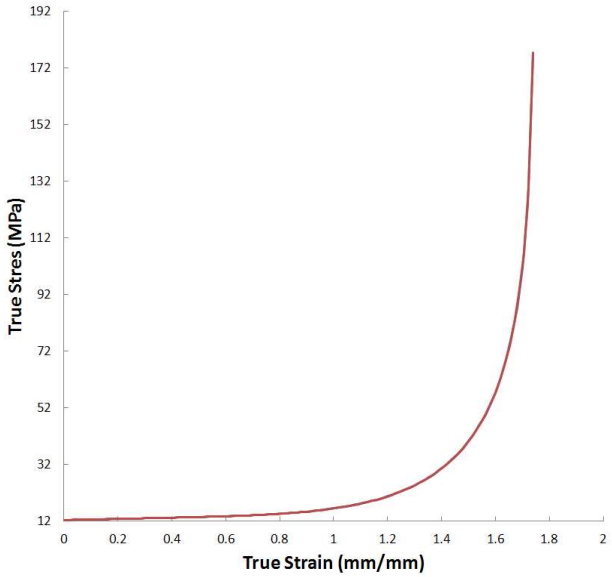

FIGURE 4.2: Stress-strain curve of the verification test

The initial and deformed shapes of the element are shown in FIGURE 4.3. The right-hand side of FIGURE 4.3 shows the compressed elements, with the four unconstrained nodes expanded to preserve the original volume of the element. FIGURES 4.4 to 4.9 show comparisons of LS-DYNA MAT 154 and the new foam model on *x*-, *y*-, *z*-direction stresses, effective plastic strain, pressure and von Mises stress. It can be seen that the results of the new foam model match those of LS-DYNA MAT 154. FIGURE 4.6 shows the time history of the *z*-direction stress (at time instant t = 3.5 *sec*) that includes the elastic, plateau, and densification regions. The plateau stress is found to be approximately 15 *MPa* and the highest stress is found to be approximately 105 *MPa*. FIGURE 4.7 shows the effective plastic strain, which accumulates during plastic deformations. The slope of the curve decreases upon entering the densification region. The rate of increase of the effective plastic strain decreases as the material densifies and the highest plastic strain is found to be 1.67.

a. Initial shape (MAT 154)

b. Deformed shape (MAT 154)

c. Initial shape (new model)

d. Deformed shape (new model)

FIGURE 4.3: Initial and deformed shapes of the verification test ($\alpha^2 = 0.25$)

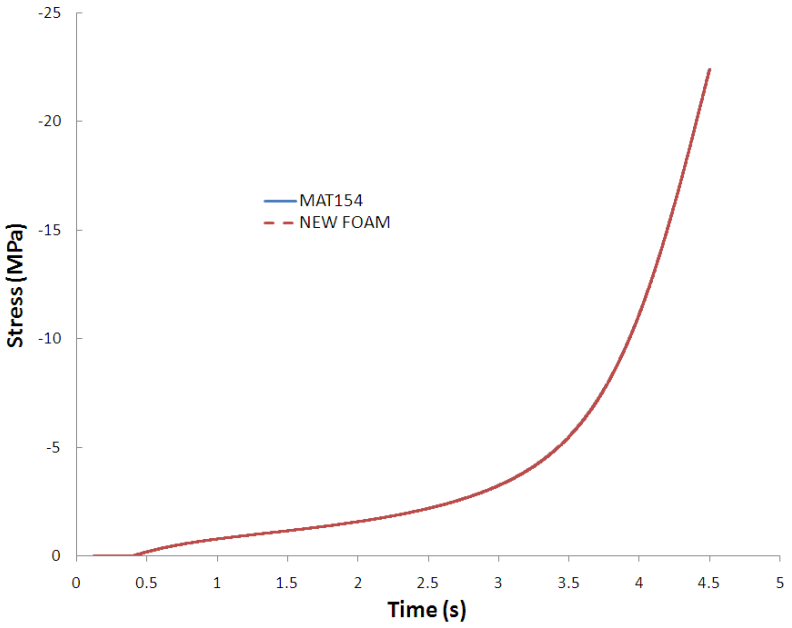

FIGURE 4.4: Time history of x-direction stress ($\alpha^2 = 0.25$)

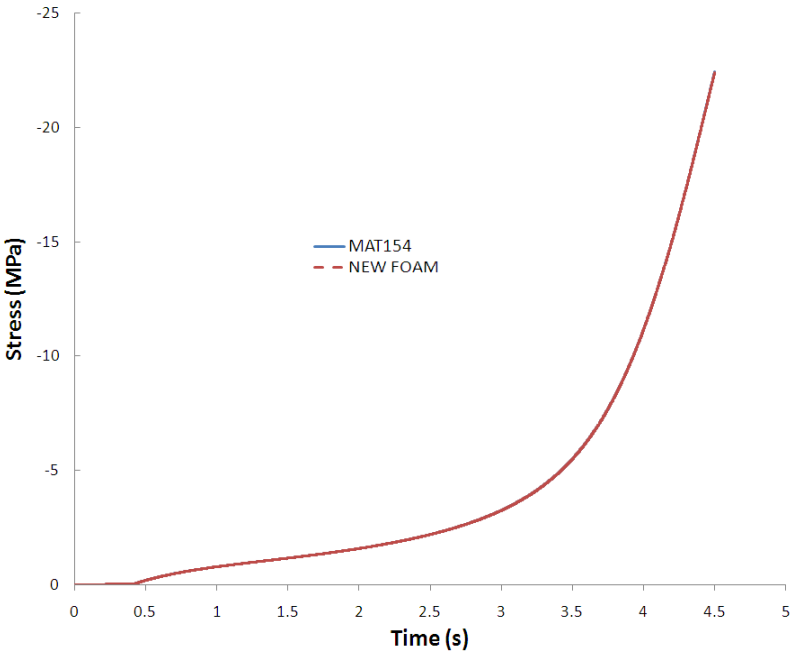

FIGURE 4.5: Time history of y-direction stress ($\alpha^2 = 0.25$)

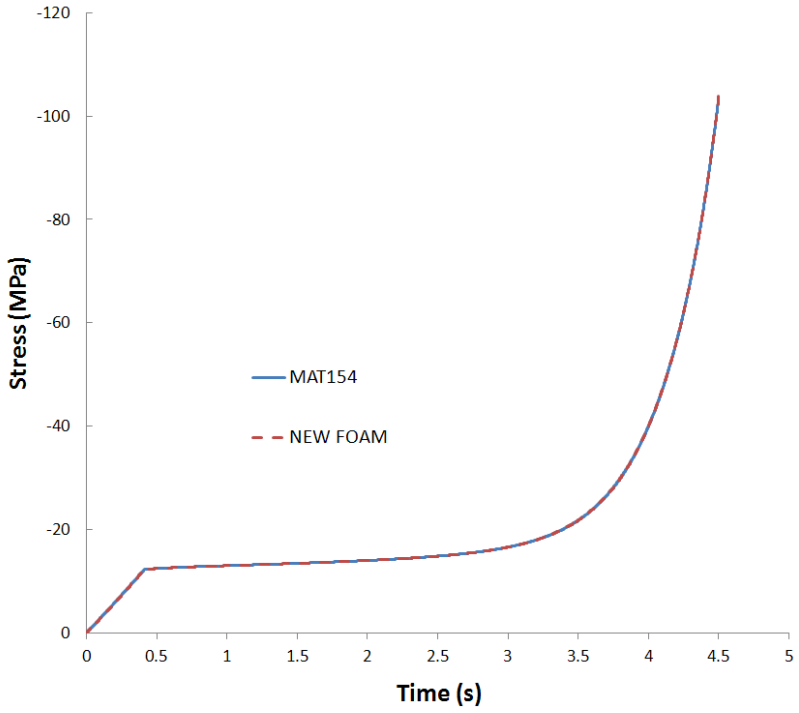

FIGURE 4.6: Time history of z-direction stress ($\alpha^2 = 0.25$)

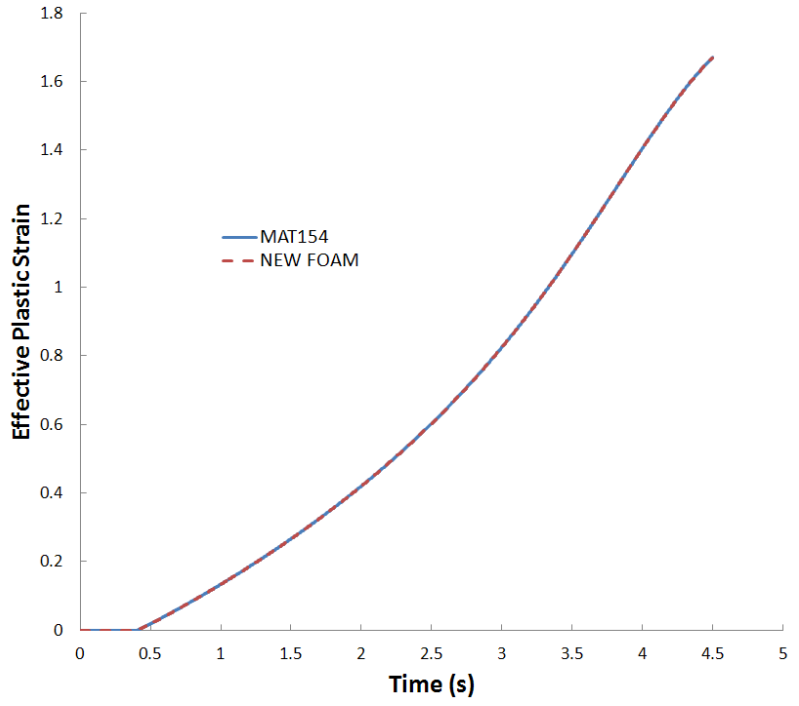

FIGURE 4.7: Time history of effective plastic strain ($\alpha^2 = 0.25$)

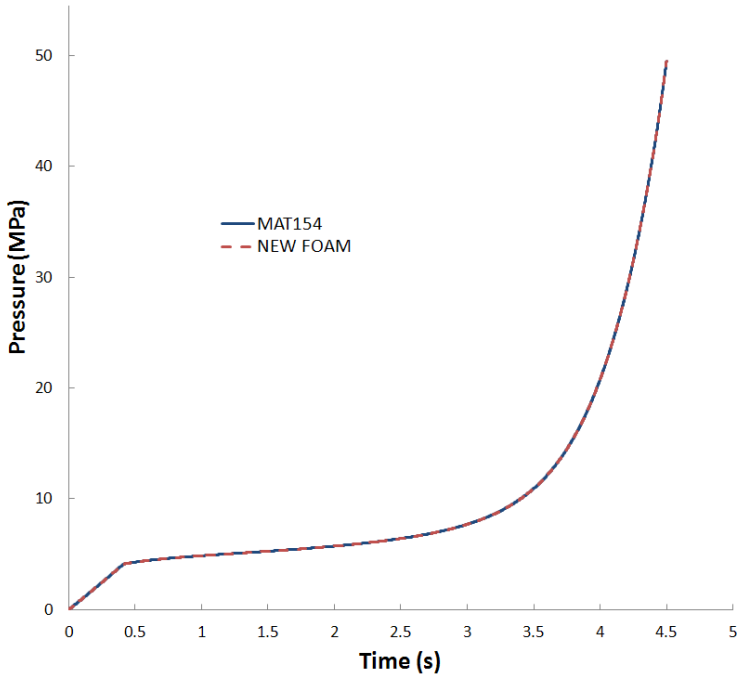

FIGURE 4.8: Time history of hydrostatic pressure ($\alpha^2 = 0.25$)

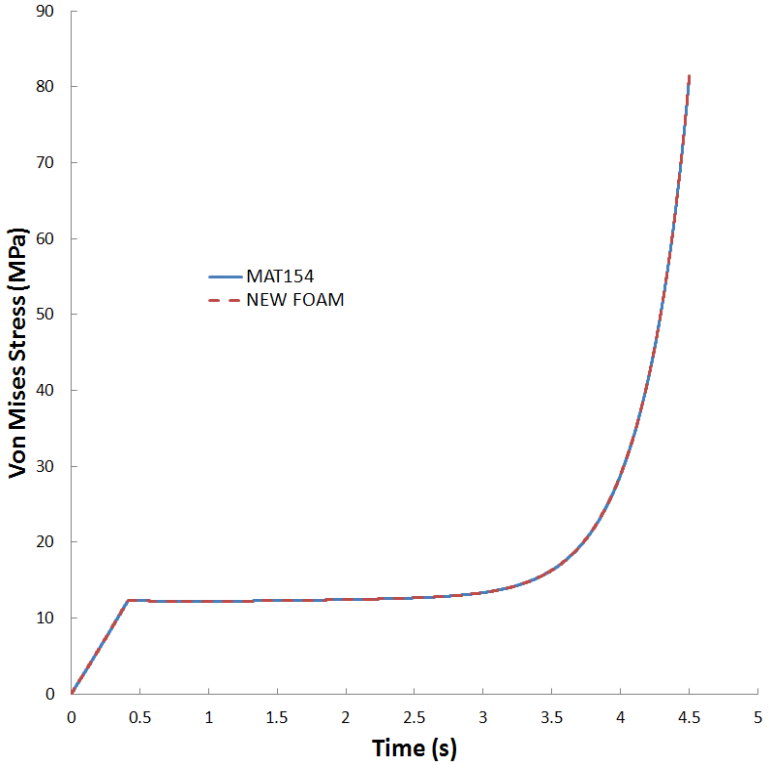

FIGURE 4.9: Time history of von Mises stress ($\alpha^2 = 0.25$)

4.3.2 Fully compressible foam

In this test the shape factor was set to a constant value of $\alpha^2 = 4.5$, representing the fully compressible condition ($\nu^p = 0$) in which the foam element will not expand in the *x*- and *y*-directions when loaded in the *z*-direction. The element was compressed for 54 *mm* in 4.5 *sec* at a constant speed of 12 *mm/s*.

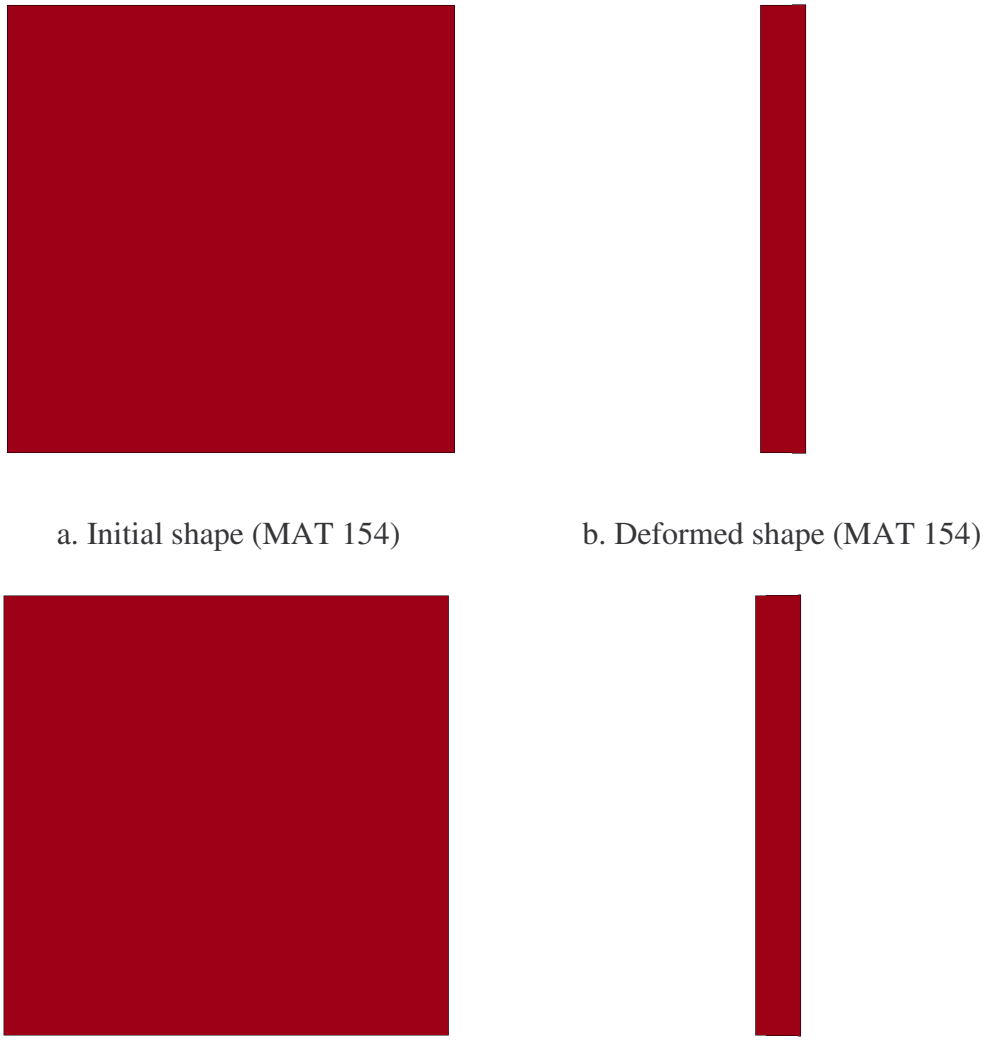

a. Initial shape (MAT 154)

b. Deformed shape (MAT 154)

c. Initial shape (new model)

d. Deformed shape (new model)

FIGURE 4.10: Initial and deformed shapes of the verification test ($\alpha^2 = 4.5$)

The initial and deformed shapes of the element are shown in FIGURE 4.10 with the right-hand side showing the compressed element. It can be seen that the element did not expand in the x- and y-directions as expected. Consequently, the volume of the element is not preserved. FIGURES 4.11 to 4.13 show comparisons of the new foam model and LS-DYNA MAT 154 on x-, y-, and z-direction stresses. In the time history of the z-direction stress shown in FIGURE 4.13, the elastic region is observed first followed by the plateau region. The densification starts at time instant t = 3.5 *sec*. The plateau stress is found to be 15 *MPa* and the highest stress is found to be 90 *MPa*. It can be seen from the time histories of stresses that the new foam model matches well to LS-DYNA MAT 154. All shear stresses were found to be zero for both the new foam model and LS-DYNA MAT 154 from the time history data.

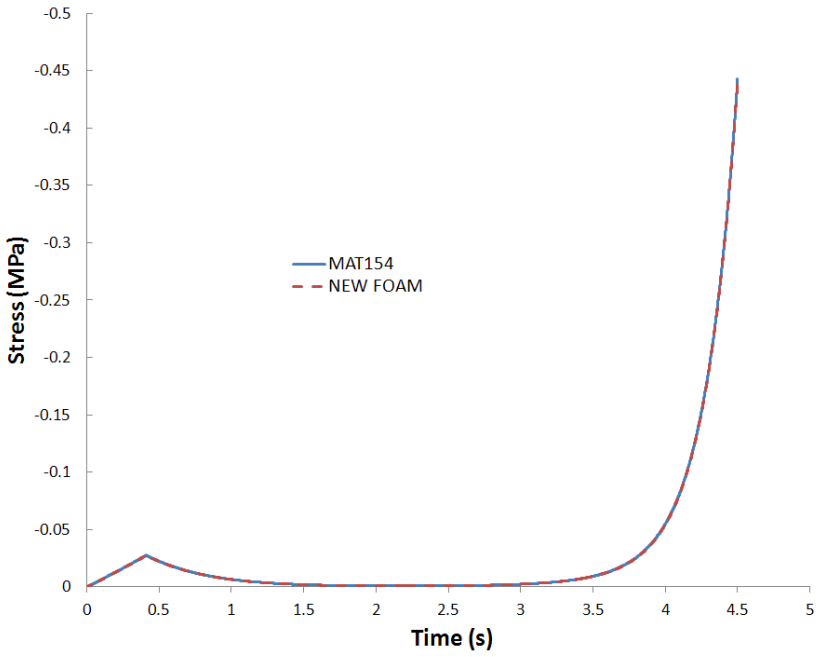

FIGURE 4.11: Time history of x-direction stress ($\alpha^2 = 4.5$)

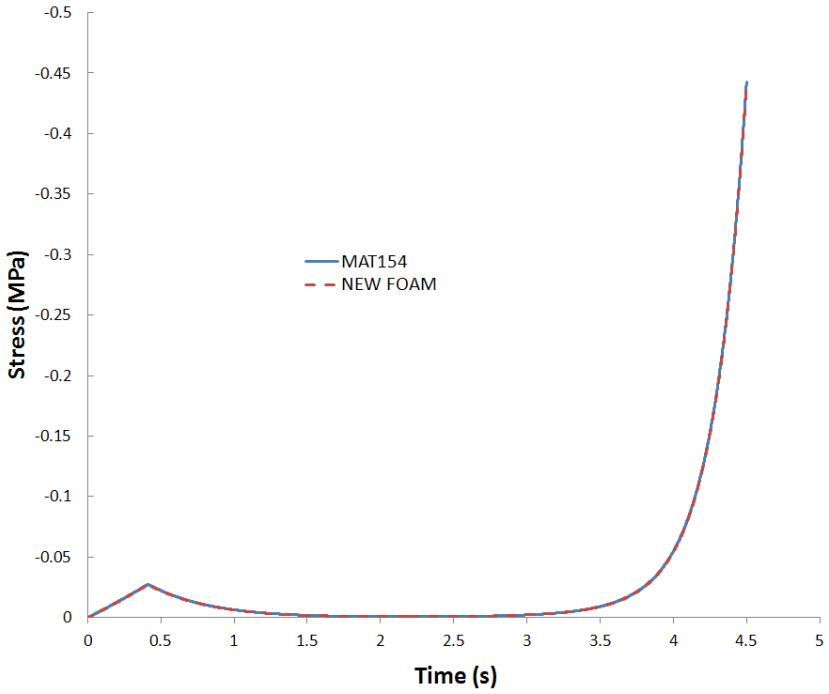

FIGURE 4.12: Time history of y-direction stress ($\alpha^2 = 4.5$)

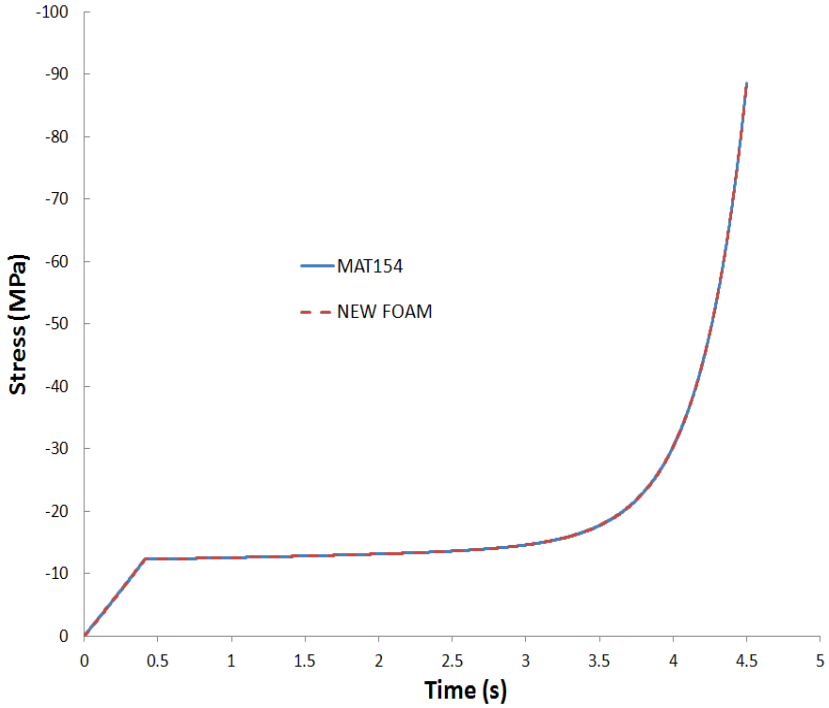

FIGURE 4.13: Time history of z-direction stress ($\alpha^2 = 4.5$)

FIGURES 4.14 to 4.16 show comparison of the two models on the effective plastic strain, pressure and von Mises stress. It can be seen from FIGURE 4.14 that the effective plastic strain remains zero in the elastic region. It then keeps increasing during plastic deformation. Upon entering the densification region, the slope of the curve decreases. The rate of increase of the effective plastic strain decreases as the material densifies. The highest plastic strain is found to be 1.68. It can be seen from the time histories of the pressure and von Mises stress that the new foam model generates the same behavior as LS-DYNA MAT 154 under the fully compressible condition.

In both tests, the constitutive equations of the new foam model showed good convergence on solutions that match those of LS-DYNA MAT 154 using constant shape factors. The element deforms in a predictable and stable manner. With predefined values

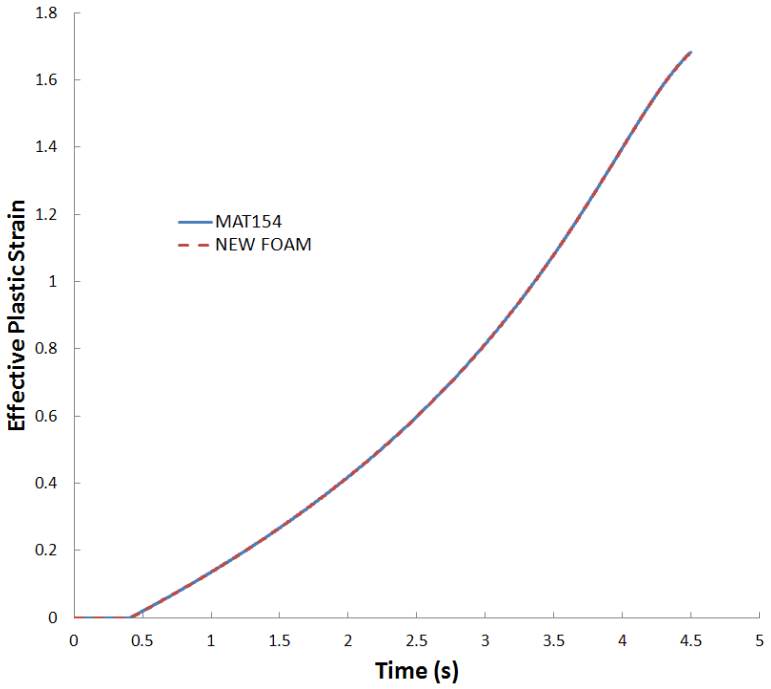

FIGURE 4.14: Time history of effective plastic strain ($\alpha^2 = 4.5$)

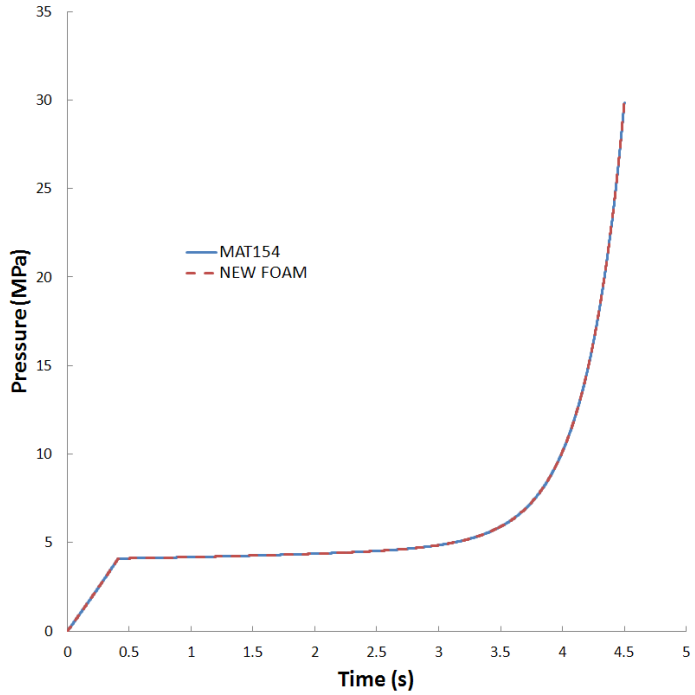

FIGURE 4.15: Time history of hydrostatic pressure ($\alpha^2 = 4.5$)

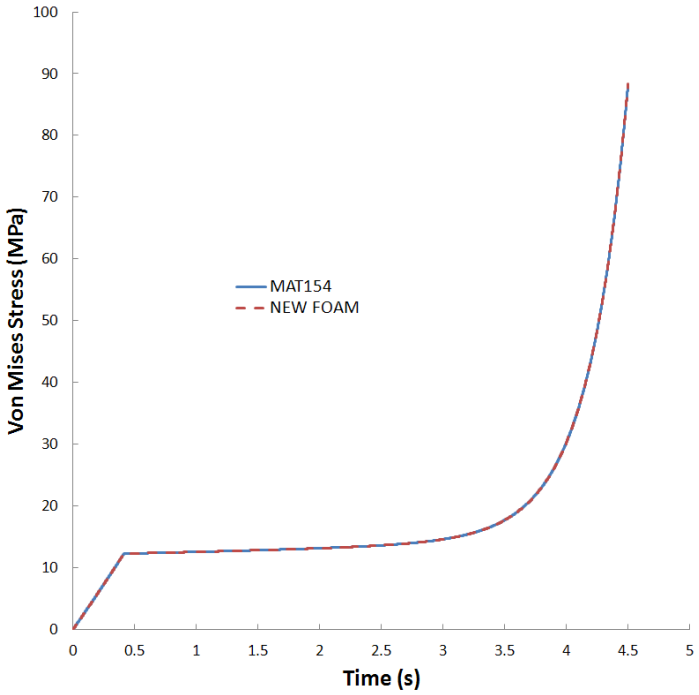

FIGURE 4.16: Time history of von Mises stress ($\alpha^2 = 4.5$)

of the shape factor, the material exhibits proper responses under both incompressible and compressible conditions. This indicates the effectiveness of the new foam model. It is therefore concluded that the material subroutine was coded correctly. Before the new foam model can be applied to crash simulations, however, comparisons against experimental data are needed to demonstrate the accuracy of the new material model. This will be discussed in the next sub-section.

4.4 Model Validation

The new foam model was validated with two experimental tests, a uniaxial compression test and a diagonal loading test, both using 70-*mm* cubic specimens. Based on a convergence study, the mesh size was determined to be 4 *mm* using constant stress solid elements. To evenly divide the 70-*mm* side of the cube, a mesh size of 3.89 *mm* was actually used. Type 6 hourglass control was applied to the foam to improve the numerical stability of the simulations. The foam model of the 70-*mm* cube had 5832 nodes and 4913 elements.

Simulation results using the new model were compared to experimental data as well as to results using four LS-DYNA built-in material models. Two different densities were analyzed: $\rho = 0.34\ g/cm^3$ for low-density foam and $\rho = 0.51 g/cm^3$ for high-density foam. For ease of discussion, the uniaxial compression tests were named U1 and U2 for the low- and high-density foams, respectively. Similarly, the diagonal loading tests were named D1 and D2 for the low- and high-density foams, respectively.

4.4.1 Uniaxial loading test

FIGURE 4.17 shows the configuration of the uniaxial compression test. The bottom surface of the cube is constrained in the loading direction. The node at the center

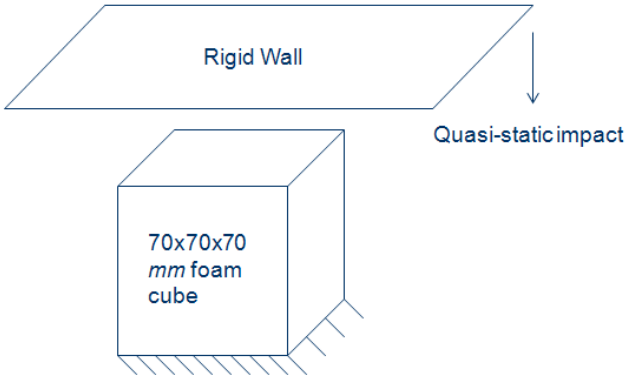

FIGURE 4.17: Model for the uniaxial loading test

of the bottom surface is constrained for all three degrees of freedom to prevent rigid body motion. The top surface of the cube is quasi-statically impacted by a rigid wall.

This uniaxial loading test was simulated using the new foam model and four LS-DYNA built-in models. FIGURE 4.18 shows the deformed shapes of the low-density foam (0.34 g/cm^3) using the new model after being crushed for 27 and 54 *mm*, respectively. It can be seen that the foam expands in both the *x*- and *y*-directions as the foam densifies.

FIGURES 4.19 to 4.22 show the simulation results of the deformed foams using LS-DYNA built-in models, MAT 5, 63, 75, and 154. The model using MAT 5 terminated

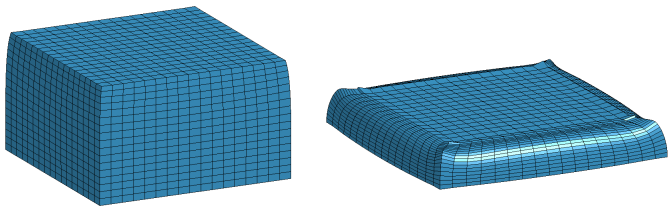

FIGURE 4.18: Deformed shapes for Case U1 using the new foam model

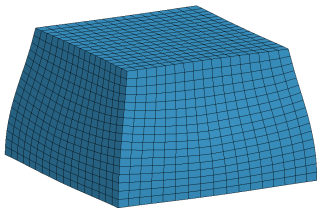

FIGURE 4.19: Deformed shapes for Case U1 using MAT 5

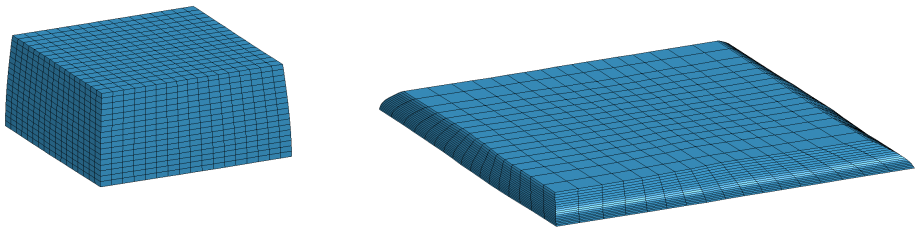

FIGURE 4.20: Deformed shapes for Case U1 using MAT 63

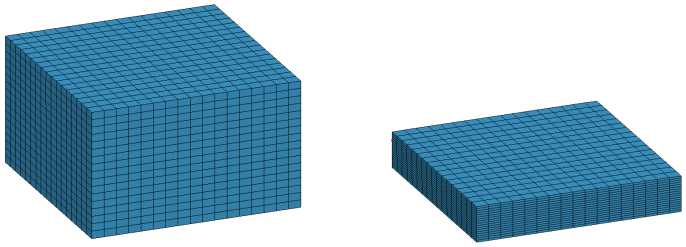

FIGURE 4.21: Deformed shapes for of Case U1 using MAT 75

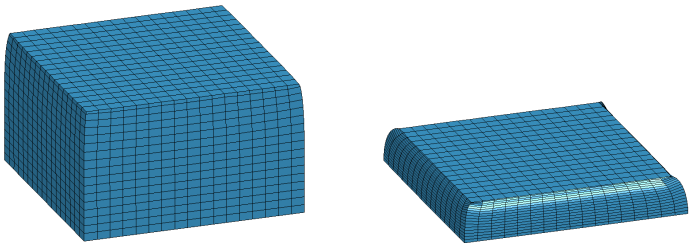

FIGURE 4.22: Deformed shapes for Case U1 using MAT 154

prematurely due to negative volumes of the foam elements. The model using MAT 63 showed no resistance to the axial load. The model using MAT 75 was shown to be fully compressible and had no expansion in *x*- and *y*-directions. The model using MAT 154 with a shape factor (α^2) of 3.7 behaved similarly to the new model but showed less traversal expansions due to the constant value of the shape factor (i.e., constant material compressibility even after the foam is densified).

The simulation results were compared with experimental measurements. FIGURES 4.23 and 4.24 are force-displacement curves for Cases U1 and U2, respectively. The instability of MAT 5 can be seen from the drop in force at a displacement of 21 *mm* for low density foam (FIGURE 4.23) as well as the oscillating force-displacement curve for high density foam (FIGURE 4.24). The crushing forces using MAT 63 show zero in both cases. This is consistent with the deformation pattern observed in FIGURE 4.20. The foam fails to provide resistance to the impact loading. MAT 75 provides a more stable and reasonable estimate of crushing force than MAT 5 and MAT 63. However, the force level during the plateau region is underestimated compared to the experimental curves for both low and high density foams. MAT 154 outperforms all other LS-DYNA built-in material models. The crushing force history for the low density foam is reasonably accurate. However, for the high density foam, MAT 154 significantly overestimated the crushing forces after the crushing distance reached 30 *mm*. The material routine fails to converge at certain time instants, and the densification region comes earlier than that shown in the experiment. For the low density foam, the new foam model matches very well with experimental data. For the high-density foam, the new foam model also shows a mismatch of densification compared to experimental

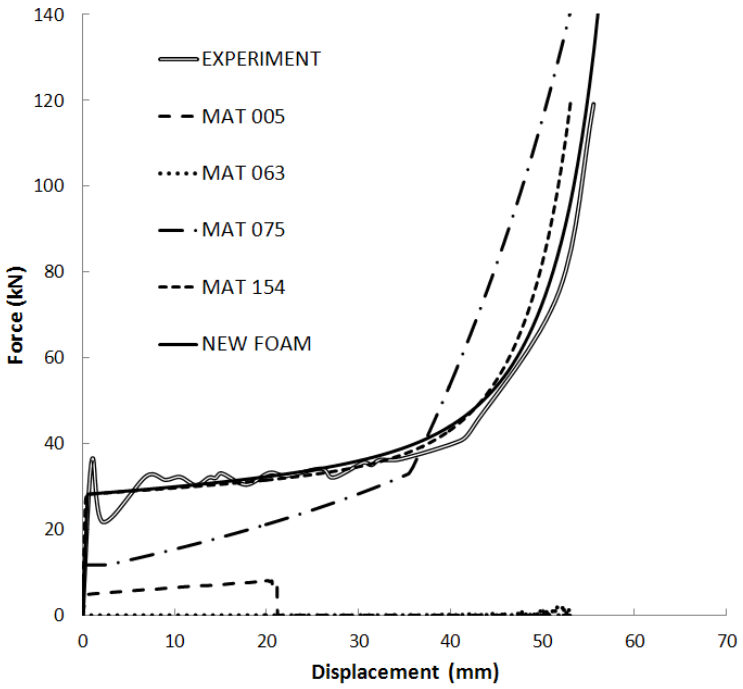

FIGURE 4.23: Comparison of force-displacement responses for Case U1

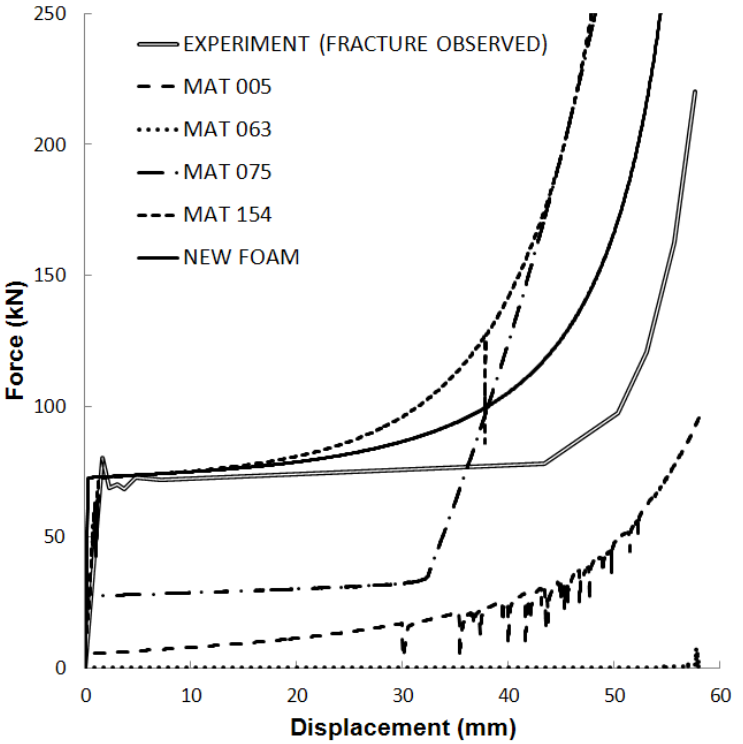

FIGURE 4.24: Comparison of force-displacement responses for Case U2

data, but it still outperforms all LS-DYNA built-in models. It should be pointed out that fractures of high-density foam were observed in experiments but are not considered in all simulation models. This could be part of the reason of the mismatch between simulation results and experimental data. Nevertheless, the new foam model is shown to provide the most accurate estimate of the crushing force histories compared to LS-DYNA built-in material models for foams of different densities.

4.4.2 Diagonal loading test

FIGURE 4.25 shows the configuration of the diagonal loading test of a 70-*mm* foam cube whose top corner was impacted quasi-statically by a rigid plate. The bottom two sides of the foam were embedded in a fixed holder and were free to displace only in the direction perpendicular to the figure.

The initial and final shapes of the FE simulation using the new foam model are shown in FIGURE 4.26. It can be seen that the new foam model matches very well with experimental measurements (FIGURE 4.25). The side view (FIGURE 4.26d) shows the

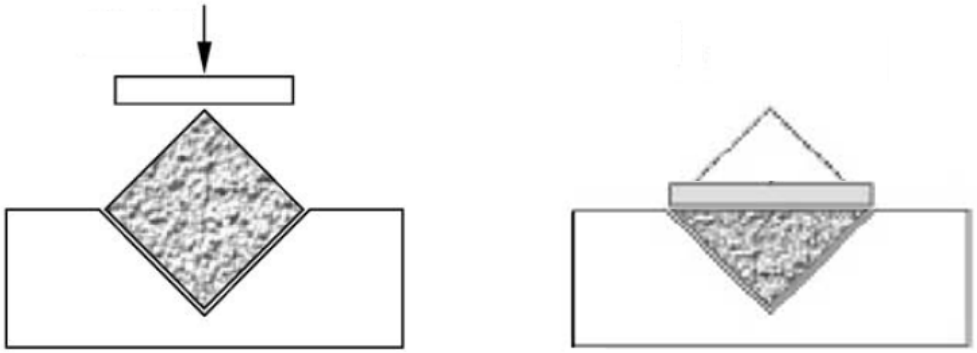

a. Initial configuration b. Final configuration

FIGURE 4.25: Experimental configuration of the diagonal loading test (Reyes et al. 2004)

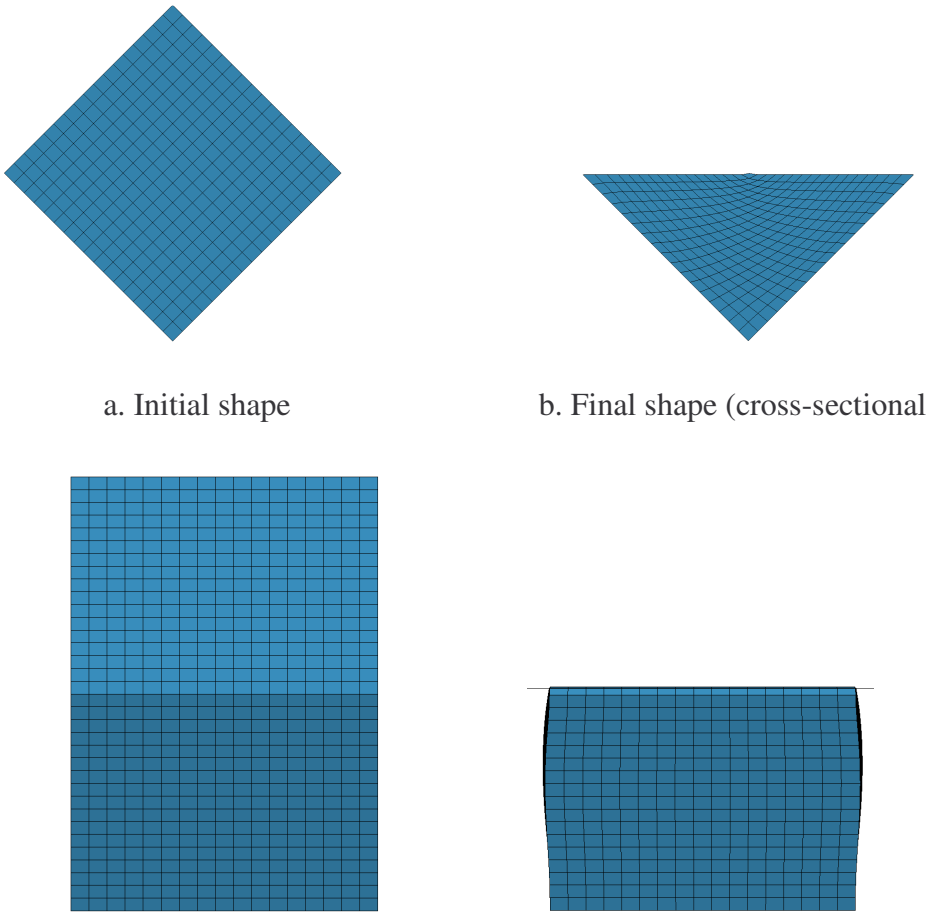

a. Initial shape

b. Final shape (cross-sectional view)

c. Initial shape (side view)

d. Final shape (side view)

FIGURE 4.26: Initial and deformed shapes for Case D1 using the new foam model

horizontal expansion of the foam. The deformed shape of the foam using MAT 5 is shown in FIGURE 4.27. The cross-sectional view of the deformed foam matches that of experimental data. However, the side view (FIGURE 4.27b) shows unrealistic expansion due to numerical instabilities. The FE simulation using MAT 63 terminated prematurely due to negative volumes in foam elements. The final shape is shown in FIGURE 4.28 in which the side view (FIGURE 4.28b) reveals the lack of resistance to the impact loading and unrealistic horizontal expansion. The FE simulation of MAT 75 completed without

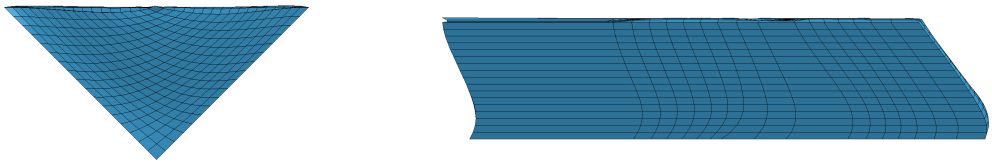

a. Final shape b. Final shape (side view)

FIGURE 4.27: Deformed shapes for Case D1 using MAT 5

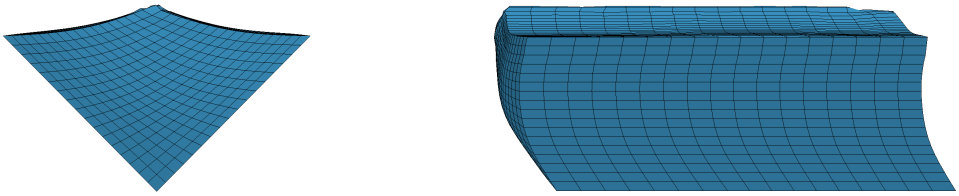

a. Final shape b. Final shape (side view)

FIGURE 4.28: Deformed shapes for Case D1 using MAT 63

a. Final shape b. Final shape (side view)

FIGURE 4.29: Deformed shapes for Case D1 using MAT 75

numerical issues, and the cross-sectional view of the deformed foam matched that of the experiment data. The side view (FIGURE 4.29b) shows no horizontal expansion of the foam, which appears to be fully compressible throughout the entire crushing process. The simulations using MAT 154 terminated at the initial stage of loading, due to failure of convergence when the edge of the foam was impacted.

FIGURES 4.30 and 4.31 show the simulation results of force-displacement responses compared to experimental data for the low- and high-density foams, respectively. The simulation results using MAT 5 was shown to underestimate the

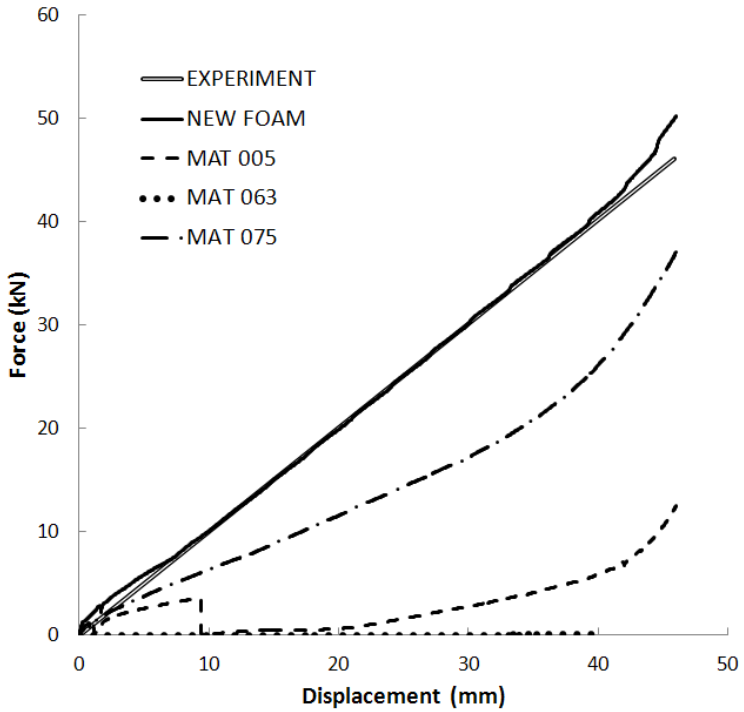

FIGURE 4.30: Comparison of force-displacement responses for Case D1

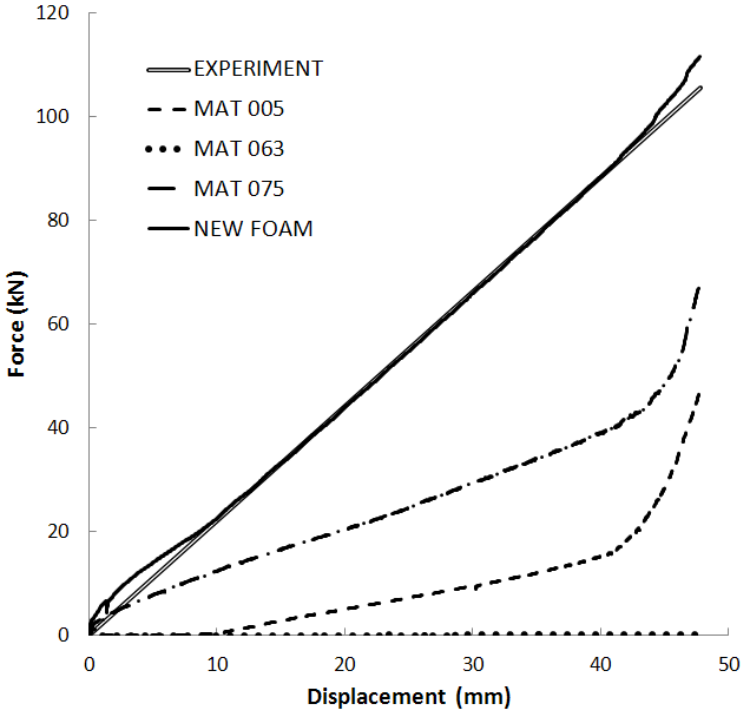

FIGURE 4.31: Comparison of force-displacement responses for Case D2

crushing forces for both Cases D1 and D2, and exhibited instability at 9 *mm* displacement for Case D1. The foam using MAT 63 showed no resistance to impact loading, similar to the case of uniaxial compression test. The simulations using MAT 75 provided better predictions of the crushing forces than MAT 7 and MAT63, but still underestimated the crushing forces compared to experimental data. The new foam model was shown to match well to experiment data for the cases of both low- and high-density foams.

To summarize, the new model was validated against experiments by the uniaxial compression test and diagonal loading test. In both tests, the new foam model provided more accurate predictions than those from the LS-DYNA built-in models. In addition, the new foam model was shown to have good numerical stability. The constitutive equations in the new foam model were solved implicitly, and convergence was reached before the internal stresses were updated. The new foam model used stable and accurate integration algorithms to solve the constitutive equations and allowed for shape changes of the yield surface. Consequently, the new foam model outperforms those LS-DYNA built-in models in the validation tests. In addition, the new material subroutine allows for close control and monitoring of the integration process of the constitutive equations. The convergence criteria can also be changed easily.

CHAPTER 5: APPLICATION IN CRASH SIMULATIONS

Seitzberger (2000) performed a series of experimental investigations on empty and foam-filled steel columns with different materials, dimensions and cross-sectional shapes. Aluminum foam was used as the filler material in the quasi-static axial crushing tests. Two experimental tests, ZM44 and ZM64 of Seitzberger's work, were chosen to further evaluate the new foam model in crash simulations. TABLE 5.1 gives the cross-sections, column material and foam density of the test specimens.

TABLE 5.1: Selected test specimens from Seitzberger's experiments

Test No.	Cross-section	Steel Tube	Foam Density $\rho_f\ (g/cm^3)$
ZM44	Square	ZstE340	0.47
ZM64	Hexagonal	ZstE340	0.47

The tubes in both tests, ZM44 and ZM64, were made of ZStE340 steel, a commonly used material in the automotive industry. The ZStE340 steel has a density of 7.89 g/cm^3 and a yield stress of 340 MPa. The stress-strain curve of ZStE340 steel from a uniaxial tensile test is shown in FIGURE 5.1. The aluminum foam used in both tests had a density of 0.47 g/cm^3. FIGURE 5.2 shows the true stress-strain curve of the aluminum foam from a uniaxial compressive test. The geometries of the square tubes used in Tests ZM44 and ZM64 are given in TABLE 5.2.

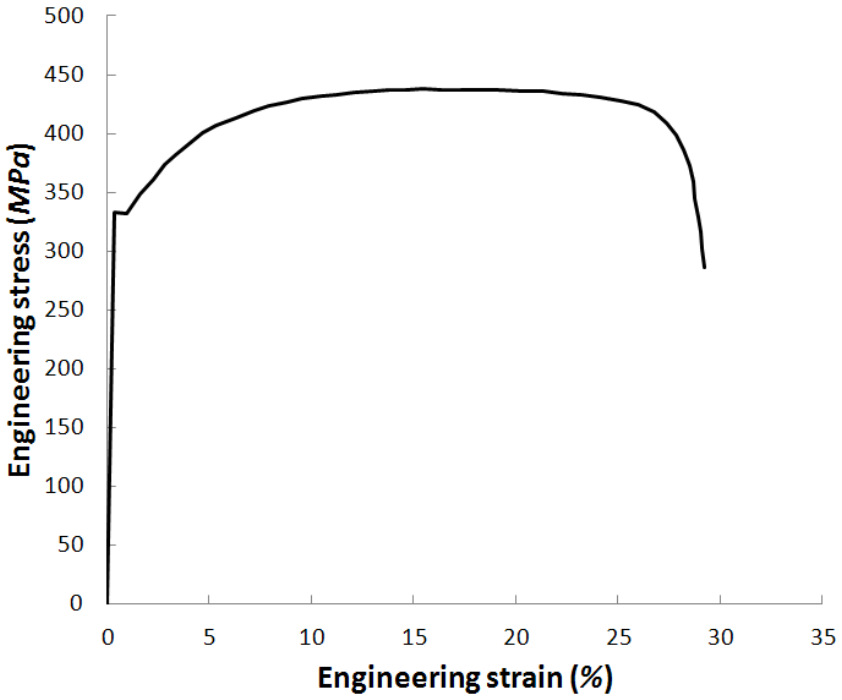

FIGURE 5.1: Engineering stress-strain curve of steel ZStE340

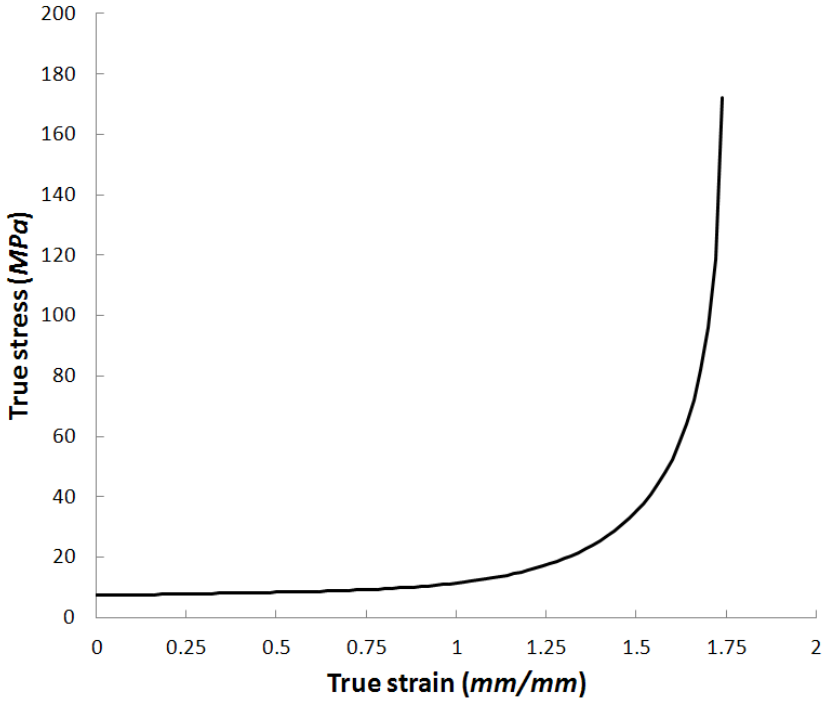

FIGURE 5.2: True stress-strain curve of aluminum foam ($\rho = 0.47$ g/mm^3)

TABLE 5.2: Tube geometries for Tests ZM44 and ZM64

Test No.	Length (*mm*)	Thickness (*mm*)	Side length (*mm*)
ZM44	250	1.5	64.5
ZM64	250	1.5	40.0

5.1 Closed-Form Solution of Mean Crushing Force

Chen (2001) developed a closed-form solution for MCF of a foam-filled square column under quasi-static loading based on the super-fold element theory developed by Wierzbicki and Abranowicz (1983). The MCF was decomposed into two parts, one from the steel tube and the other from the foam, expressed as

$$P_{mf} = P_m + \Delta P_m \tag{5.1}$$

where P_{mf} is the total MCF of the foam-filled column, P_m is the MCF of the tube without foam, and ΔP_m is the elevated force by adding the foam filler.

Assuming the compressed fold has a height of $2H$, total width of b, wall thickness of t and is crushed by a distance of δ. The principle of virtual velocities is expressed as

$$P\dot{\delta} = \dot{E} \tag{5.2}$$

where $P\dot{\delta}$ is the rate of work done by the resultant crushing force and $\dot{E}$ is the rate of energy dissipation. Eq. (5.2) is integrated into the following form with details given in the work of Wierzbicki and Abranowicz (1983)

$$\frac{P_m}{M_0} = A_1 \frac{r}{t} + A_2 \frac{b}{H} + A_3 \frac{H}{r} \tag{5.3}$$

where M_0 is the plastic bending moment, r is the radius of a deformed toroidal surface and A_1, A_2 and A_3 are coefficients to be determined from the following equation based on an assumption that the collapse mechanism leads to the smallest MCF.

$$P_m = \frac{3}{4}\sqrt[3]{A_1 A_2 A_3}\,\sigma_0 b^{1/3} t^{5/3} \tag{5.4}$$

For a square tube (without the foam filler), the MCF is given by

$$P_m = 13.06\sigma_0 b^{1/3} t^{5/3} \tag{5.5}$$

and for a hexagonal tube, the MCF is expressed as

$$P_m = 20.23\sigma_0 b^{1/3} t^{5/3} \tag{5.6}$$

For columns with foam filler, the force elevation ΔP_m is expressed as a function of material properties and geometries of the tube and foam as

$$\Delta P_m = f(\sigma_0, \sigma_f, b, t) \tag{5.7}$$

where σ_0 is the yield stress of the tube, σ_f is the plateau stress of the foam, b is the side length of the tube, and t is the wall thickness of the tube. Based on dimensional analysis and curve fitting of experimental data, Chen (2001) developed the following equations for calculating force elevations caused by the foam filler:

$$\Delta P_m = 1.8 b^2 \sigma_f \tag{5.8}$$

for square columns, and

$$\Delta P_m = 4.68 b^2 \sigma_f \tag{5.9}$$

for hexagonal columns. Therefore, the total MCFs of foam-filled columns can be expressed as

$$P_{mf} = 13.06\sigma_0 b^{1/3} t^{5/3} + 1.8 b^2 \sigma_f \tag{5.10}$$

for square columns, and

$$P_{mf} = 20.23\sigma_0 b^{1/3} t^{5/3} + 4.68 b^2 \sigma_f \tag{5.11}$$

for hexagonal columns.

Using Eqs. (5.10) and (5.11), the estimated MCFs for the two experimental tests are obtained and given as

$$P_{mf} = 13.06 \times 340 \times 64.5^{1/3} \times 1.5^{5/3} + 1.8 \times 64.5^{2} \times 7.286 = 89.56 \ kN \qquad (5.12)$$

for the square column (ZM44) and

$$P_{mf} = 20.23 \times 340 \times 64.5^{1/3} \times 1.5^{5/3} + 4.68 \times 64.5^{2} \times 7.286 = 100.79 \ kN \qquad (5.13)$$

for the hexagonal column (ZM64). Closed form solutions provide simple and quick estimates for assessing the soundness of numerical solutions, such as FE simulation results.

5.2 Finite Element Simulation Setup

The crash simulation models for square and hexagonal columns are shown in FIGURES 5.3 and 5.4, respectively. In both cases, the columns rest on a rigid wall with all degrees of freedom fixed and are impacted from the top by another rigid wall travelling at a constant velocity of 1 *mm/s*, the same impact speed used in the experiments. Based on mesh convergence studies, the mesh sizes used for the tube and the foam were chosen as 3 *mm* and 4 *mm*, respectively.

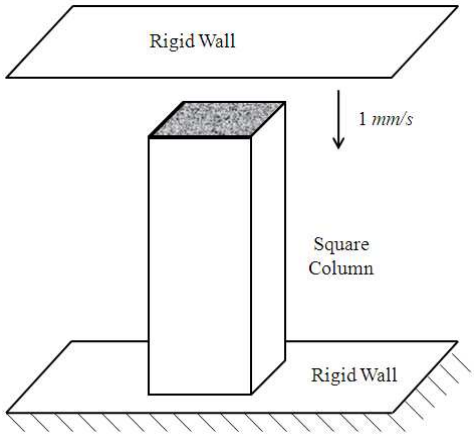

FIGURE 5.3: Model of crash simulation of square column

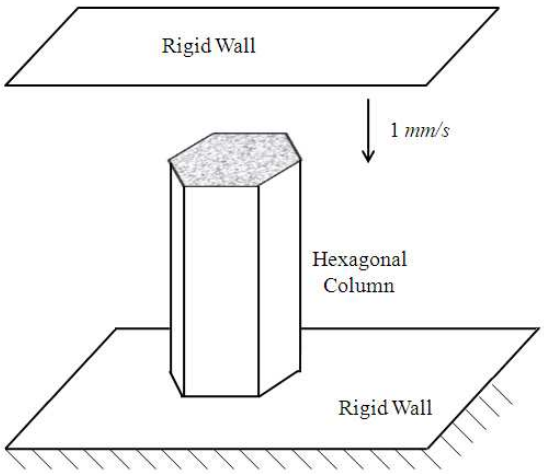

FIGURE 5.4: Model of crash simulation of hexagonal column

Nodes-to-surface contacts were defined between the foam and the two rigid walls as well as between the tube and the rigid walls. The foam and tube were defined as the slave parts and the two rigid walls were defined as the master parts. The rigid walls were modeled by shell elements with a mesh size of 100 *mm*, much larger than the cross-sectional sizes of the two columns to ensure no penetration. The simple nodes-to-surface contact performs stably since there is no deformation of the rigid walls and the master normal projections remain unchanged throughout the crushing process. Automatic-single-surface contact was used between the foam and the tube. Potential penetrations between any surfaces of the two parts are checked, including self-contacts that may occur on the same part. For example, when the tube folds progressively during the crash, adjacent surfaces around the folds may be in contact and must be considered to prevent unrealistic penetrations. Interior contact check was also adopted for the foam to account for contacts between the layers of the 8-noded solid elements to prevent element inversion.

The piecewise-linear plasticity model was adopted for the tube, which has a density of 7.89 *g/cm*^{3}, Young's modulus of 210 *GPa*, Poisson's ratio of 0.3, and yield stress of 340 *MPa.* The stress-strain curve of this model is shown in FIGURE 5.1. The Cowper and Symonds model was used to account for the strain rate effect of the steel column's wall. This is shown in Eq. (5.14). The constants D and q were set as 424 and 4.73, respectively (Cunat 2000).

$$\sigma_y = \sigma_y^0 \left[1 + \left(\frac{\dot{\varepsilon}}{D} \right)^{1/q} \right] \tag{5.14}$$

The time-step in a simulation is determined by the minimum value of the time-steps of all elements expressed as

$$\Delta t = a \cdot \min\left\{ \Delta t_1, \Delta t_2, \Delta t_3, ..., \Delta t_N \right\} \tag{5.15}$$

where N is the number of the elements in the simulation and a is a scale factor. For 8-node solid elements, the following equation is used to calculate the time-step size.

$$\Delta t_e = \frac{L_e}{Q + \left(Q^2 + c^2 \right)^{\frac{1}{2}}} \tag{5.16}$$

where L_e is the characteristic length of the element. This is usually calculated using the element volume divided by the largest side area of the element given by

$$L_e = \frac{V_e}{A_{\max}} \tag{5.17}$$

In Eq. (5.16), Q is a function of the linear and quadratic bulk viscosity coefficients C_0 and C_1 given by

$$Q = \begin{cases} C_1 c + C_0 L_e \left| \dot{\varepsilon}_{kk} \right| & for\ \dot{\varepsilon}_{kk} < 0 \\ 0 & for\ \dot{\varepsilon}_{kk} > 0 \end{cases} \tag{5.18}$$

where c is the adiabatic sound speed; and $\dot{\varepsilon}_{kk}$ is the sum of the three normal strain rates expressed as

$$\dot{\varepsilon}_{kk} = \dot{\varepsilon}_{11} + \dot{\varepsilon}_{22} + \dot{\varepsilon}_{33} \tag{5.19}$$

Mass scaling is used in the simulations of this dissertation in order to achieve a larger explicit time-step. The mass scaling algorithm is processed at the beginning of each simulation. The time-step for each element is calculated first. If the time-step of an element is smaller than the given mass scaling time-step, LS-DYNA modifies the mass density of the element so that the time-step of this element equals that of the mass scaling time-step. Although mass scaling can significantly increase the mass during an FE simulation, it is particularly useful for quasi-static analyses and simulations with varied mesh sizes. The effect of added mass is insignificant for a quasi-static analysis due to the low velocity and small kinetic energy relative to the peak internal energy.

The hourglass-mode deformation of solid elements can swamp the results of a simulation. Hourglass-mode deformations are usually resisted by viscosity. Hourglass control adds stiffness to the system to prevent materials that undergo extremely large deformation, such as foams, from distorting and creating negative volumes. When no adaptive re-meshing is used, there is a limit to how much deformation the Lagrangian mesh can accommodate. A negative volume calculation will cause the LS-DYNA simulation to terminate prematurely. In this research Type 6 hourglass control with a coefficient of 0.1 was applied to all solid elements of the metallic foam for the low velocity impacts. The hourglass energy was checked to ensure that it did not affect the overall energy absorption of the metallic foam.

5.3 Analysis of Simulation Results

Simulation results on the deformation pattern, first peak load, crushing force history, and energy absorption are presented and compared to experimental data from literature. The MCFs of FE solutions are also compared with closed form solutions developed by Chen (2001). FE simulations for the square column are also carried out using four of the LS-DYNA built-in material models for the foams. Results are presented and the accuracy and stability of each of the models are evaluated. Based on these FE simulations, the relative merits of the new foam model are discussed. The new foam model is then applied to the crushing of the hexagonal column filled with foam. The deformation pattern, crushing force history, and energy absorption characteristics are described.

5.3.1 Square column filled with foam

FIGURE 5.5 shows the deformed shape of a square column from an FE simulation using the new foam material model. The column deformed in a stable and progressive folding pattern. The aluminum foam was pushed towards the center of the column due to the inward folding of the column wall. In the highly densified area where the column wall folds out, the foam elements tend to preserve their dimensions in the horizontal direction by extending towards the external column wall.

Higher densification was observed on foam elements in the outer region between the progressive folds of the column due to multi-axial compressions. In both the experiment and FE simulation, combinations of asymmetric and symmetric folding modes were observed. The asymmetric and symmetric folding modes are schematically illustrated in FIGURE 5.6. In an asymmetric folding mode, the sides around the

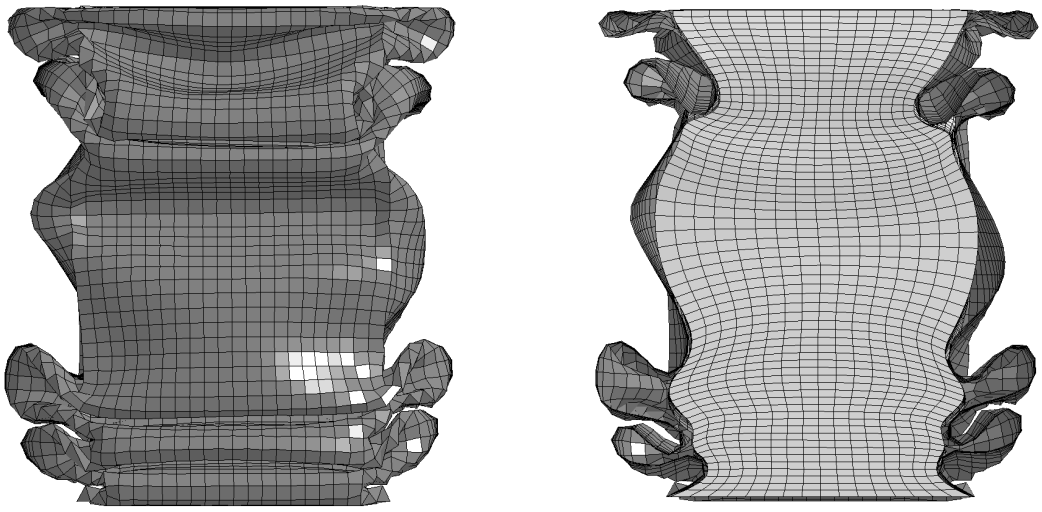

a. Deformed shape of tube

b. Cross-sectional view of deformed foam and tube

FIGURE 5.5: Deformed shapes of the FE simulation using the new foam model

circumference of the column fold alternately inward and outward. In a symmetric folding mode, all the sides around the circumference of the column extend outward. In the crushing of the square foam-filled column, the highest layer of folding showed a symmetric/extensional folding mode and the rest of the column exhibited asymmetric folding modes. Seitzberger et al. (2000) explained that asymmetric folding modes are more likely to form for columns of simple geometry (e.g., square columns) while symmetric/extensional folding modes are more likely to form for more complicated columns such as octagonal columns.

FIGURE 5.7 shows the deformed shapes of the square foam-filled column from FE simulation compared to experimental data from the work by Seitzberger et al. (2000). It can be seen that the deformation pattern from FE simulation does not completely match the pattern observed in the experiment. For example, the folding length of the column

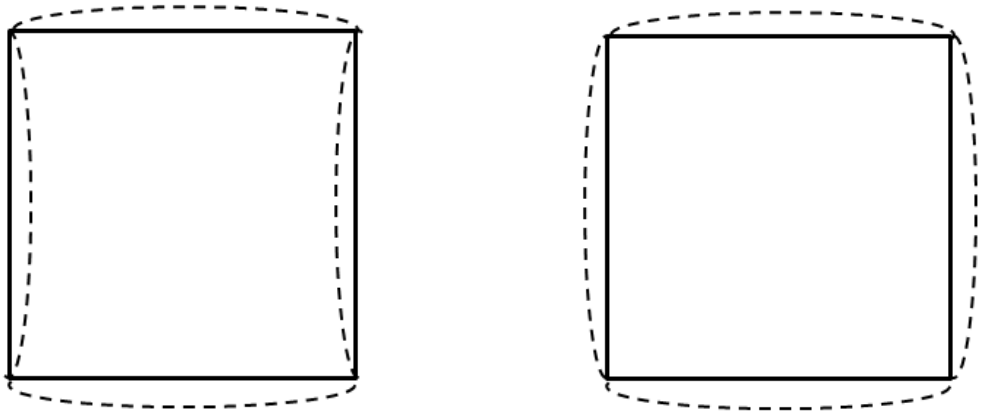

a. Asymmetric folding mode b. Symmetric/extensional folding mode

FIGURE 5.6: Folding modes of square columns

a. FE simulation with new foam model b. Experiment (Seitzberger et al. 2000)

FIGURE 5.7: Comparison of simulation results with experimental data on crushed column

wall was slightly lower than that observed in the experiment. However, both the FE simulation and the experiment showed asymmetric folding modes and five layers of

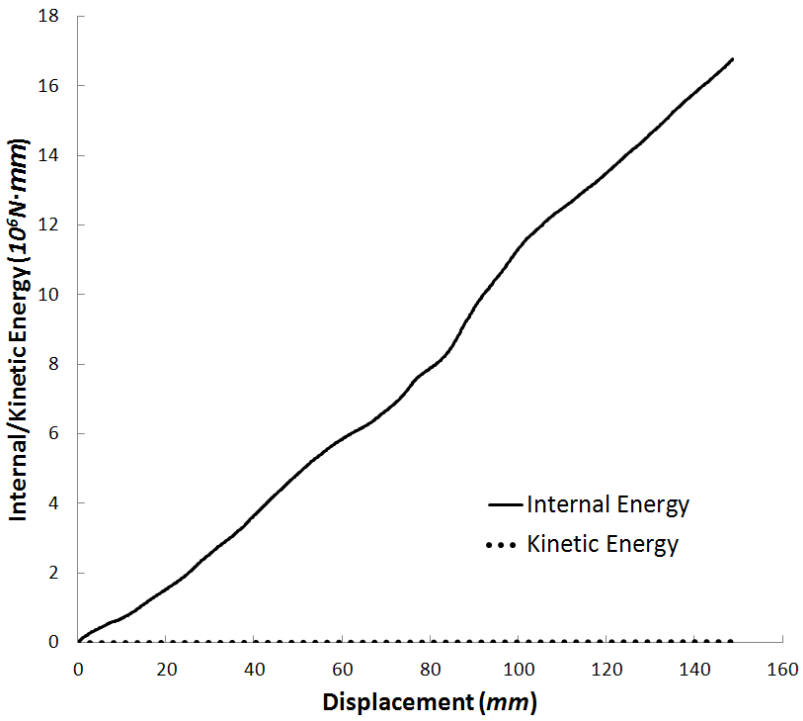

FIGURE 5.8: Internal and kinetic energy of the square column from FE simulation using the new foam model

successive folds (nine lobes) developed in the final deformed shapes. Furthermore, the FE simulation was stable and successfully finished with a total crushing distance equal to 150 *mm* (60% of its initial length). FIGURE 5.8 shows the internal energy absorption and kinetic energy curves obtained from the FE simulation. The energy absorption (i.e., internal energy) at the end of the simulation was 1.68×10^{7} $N{\cdot}mm$. The kinetic energy was in order of 10^{-1} $N{\cdot}mm$, which is less than 0.01% of the total internal energy and is considered to be negligible. This negligible kinetic energy found in the FE simulation also conforms with the simulation setting of the quasi-static condition.

The crushing force history from the FE simulation was compared to that measured from the experiment. This is shown in FIGURE 5.9. The first maximum peak load was

predicted to be 145 *kN* by FE simulation, while the peak load was found to be 137 *kN* in the experiment. The first peak load was captured in the FE simulation with an error of less than 6%. The first peak in the simulation occurred 0.1 seconds before this peak in the experiment. This could be due to imperfections in the experimental specimen that caused local plastic deformations during testing.

The MCF obtained from the FE simulation was 87.50 *kN*, which represents a 2% error compared to the closed form solution (89.56 *kN*) and a 7% error compared to experimental data (81.70 *kN*). Thus, one can see from the crushing force history in FIGURE 5.9 that the resultant crushing forces were captured relatively well. The

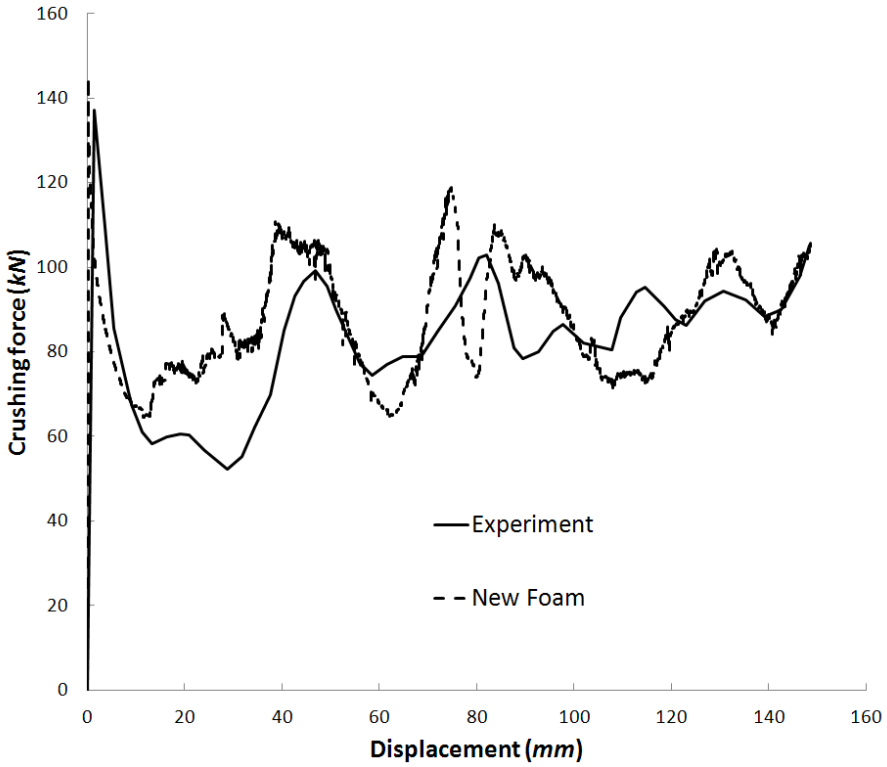

FIGURE 5.9: Force-displacement curves: new foam model vs. experimental results

aluminum foam acted as a foundation for the column wall and elevated the resultant crushing forces as the column was crushed.

For comparison purposes, the same experiment was simulated using four of the LS-DYNA built-in material models (MAT 5, MAT 63, MAT 75 and MAT 154). The same impact conditions and simulation setup (boundary conditions, time-step, contact formulations, mass scaling, etc.) were used. Among these four models, the simulations using MAT 5, MAT 63 and MAT 154 did not successfully finish.

The FE simulation using MAT 5 terminated at a displacement of 18 *mm* due to negative volumes occurred in foam elements. A plastic strain of 2.95 *mm/mm* was reached in a solid element just before the negative volume occurred in this element, and the FE simulation terminated at 18 *sec* (FIGURE 5.10). The negative volume problem could not be eliminated by decreasing the time-step of simulation. A potential weakness of this material model lies in its inability to adequately handle multi-axial

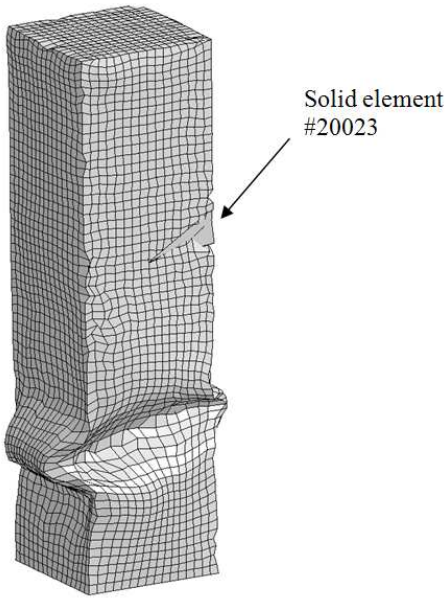

FIGURE 5.10: Foam elements after deformation (MAT 5)

compression in conjunction with large deformations. FIGURE 5.11 shows the crushing force history of the FE simulation using MAT 5. It can be seen that the first peak load and the subsequent levels of crushing force were significantly underestimated. This quantitatively shows that MAT 5 was unable to estimate the resultant crushing force including the force elevated from the non-filled column. Although MAT 5 may be suitable for FE simulations of soils and certain foams with carefully chosen material parameters, it is not appropriate for metallic foams used in crash simulations when multi-axial compression and large deformations are expected.

The FE simulation using MAT 63 also exhibited premature termination at a displacement of 20 *mm*. An erroneous strain value of 3.56 *mm/mm* was found in a solid element just before negative volumes were found in this element and adjacent elements (FIGURE 5.12). The time history of crushing force versus displacement is shown in FIGURE 5.13. It can be seen that MAT 63 underestimated the force levels, largely due to the inaccurate calculation of internal stresses.

The deformed shapes of the FE simulation using MAT 75 are shown in FIGURE 5.14. The column wall exhibited a symmetric/extensional folding mode. This is because the foam failed to expand horizontally into the folds of the column walls. This non-expandable behavior was possibly the cause of the mismatch on the deformed shapes between simulation results and experimental observation. The crushing force history is shown in FIGURE 5.15. It can be seen that the first predicted peak load was 130 *kN*, showing a good match to the 137 *kN* from the experiment. Subsequent crushing force levels, however, were significantly overestimated and accompanied with significantly larger fluctuations than those in the experiment due to the symmetric folding mode. This

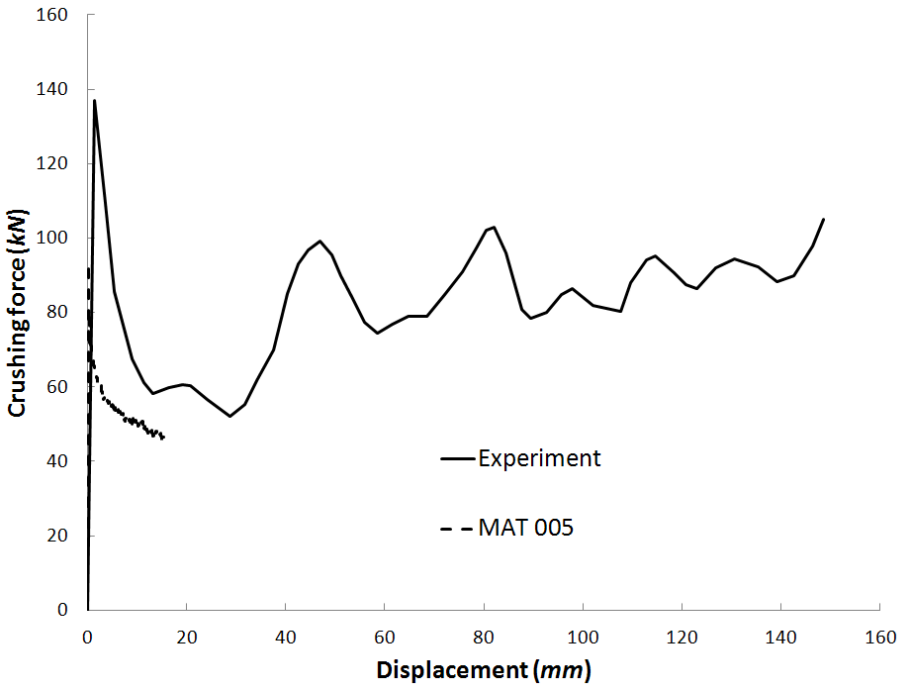

FIGURE 5.11: Force-displacement curves: MAT 5 vs. experimental results

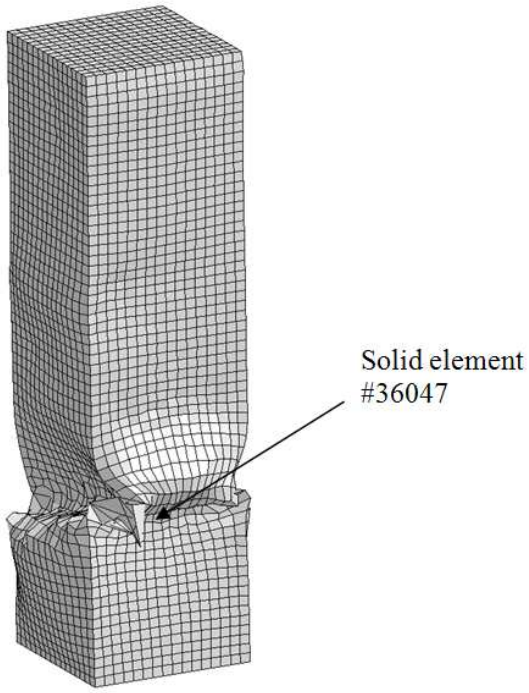

FIGURE 5.12: Foam elements after deformation (MAT 63)

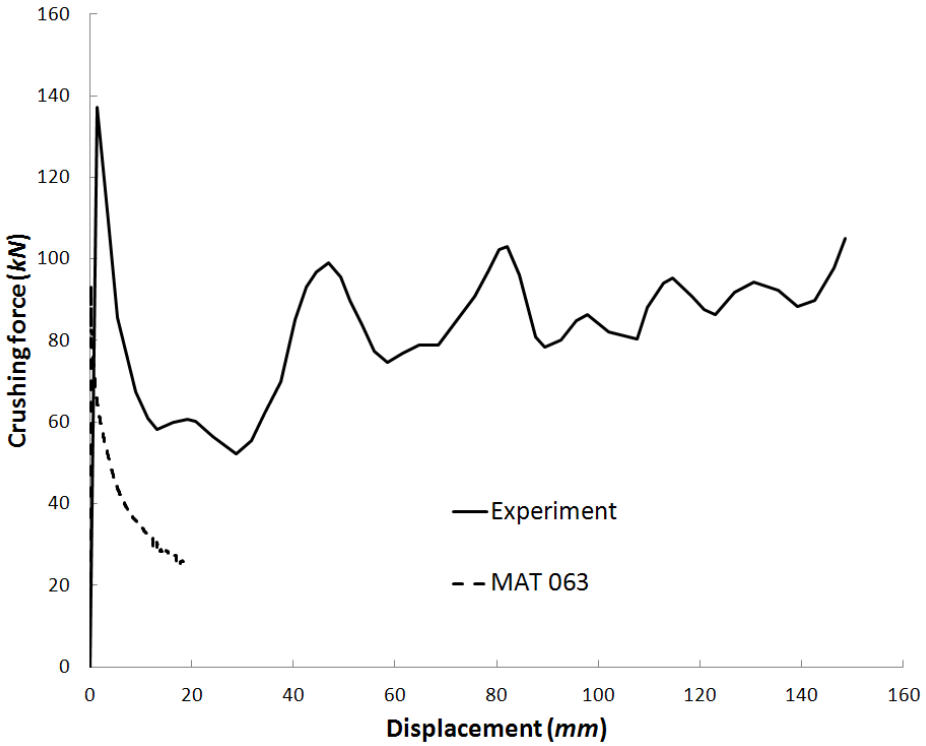

FIGURE 5.13: Force-displacement curves: MAT 63 vs. experimental results

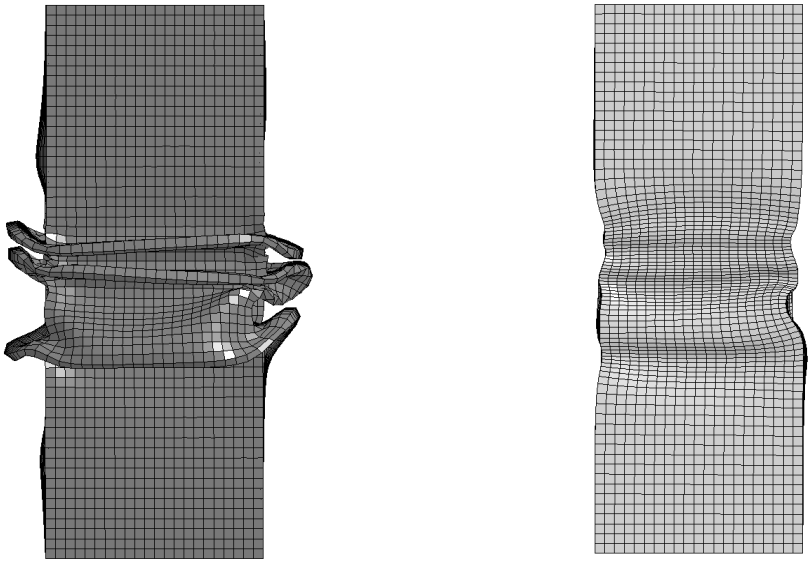

a. Deformed shape of column wall b. Deformed shape of foam

FIGURE 5.14: Deformed shapes of the FE simulation using MAT 75

observation is consistent with the experimental findings of Setzberger et al. (2000). The simulation using MAT 75 was expensive due to the low convergence rate during integration of the constitutive equations. For this reason the crushing was only simulated for an 85 *mm* crush distance.

The FE simulation using MAT 154 exhibited premature termination. A global bending was observed to be the dominant deformation mode, as shown in FIGURE 5.16. When reached a displacement of 30 *mm*, the material subroutine stopped converging, and the simulation finally terminated at a displacement of 85 *mm* due to out-of-range velocities. FIGURE 5.17 shows the crushing force history predicated by MAT 154. The first peak load was not captured due to a lag in the elevated force provided by the foam. The force elevation occurred at a later time, approximately at 15 *sec* and produced the second peak load at a displacement of 15 *mm*. Although the MCF from simulation using MAT 154 was similar to the experimental data, the significant difference in the deformation patterns indicated that it was less accurate than the new foam model, not to mention the instability of MAT 154 for its premature termination of the simulation.

For comparison purposes, the linear interpolation model of the plastic Poisson's ratio with respect to the true strain, given by Eq. (3.116), was also implemented and tested. FIGURE 5.18 shows the deformed shapes of the FE simulation using the linear interpolation model. The column wall folded progressively for the first three layers with an asymmetric folding mode. However, global buckling was formed afterwards as shown in FIGURE 5.19. The use of a linear interpolation formulation maintained a constant rate of increase on the shape factor even after the foam became densified and thus resulted in a global buckling deformation mode.

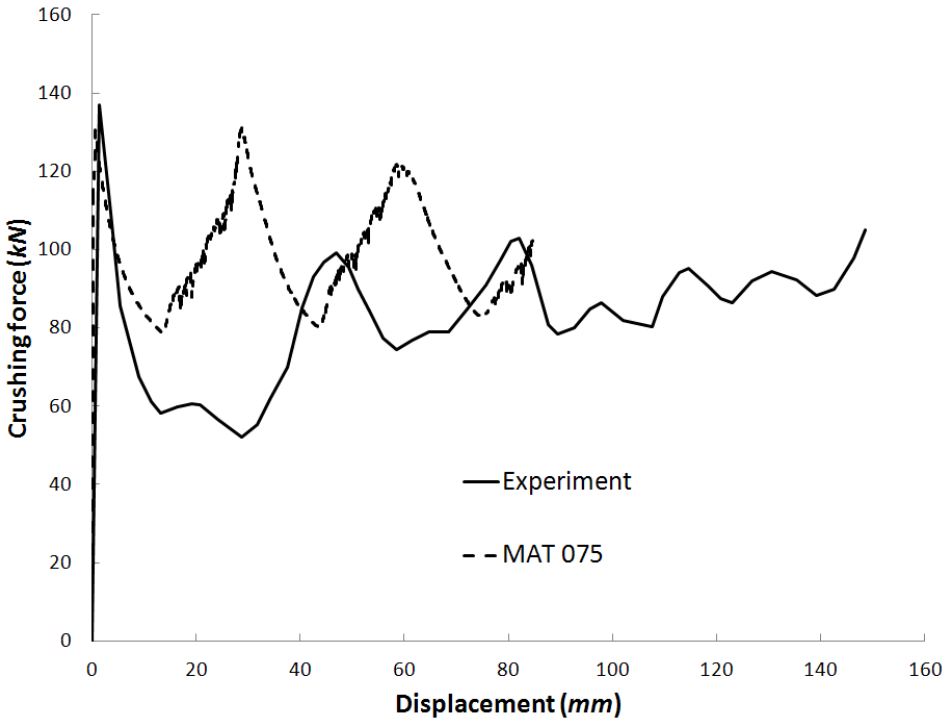

FIGURE 5.15: Force-displacement curves: MAT 75 vs. experimental results

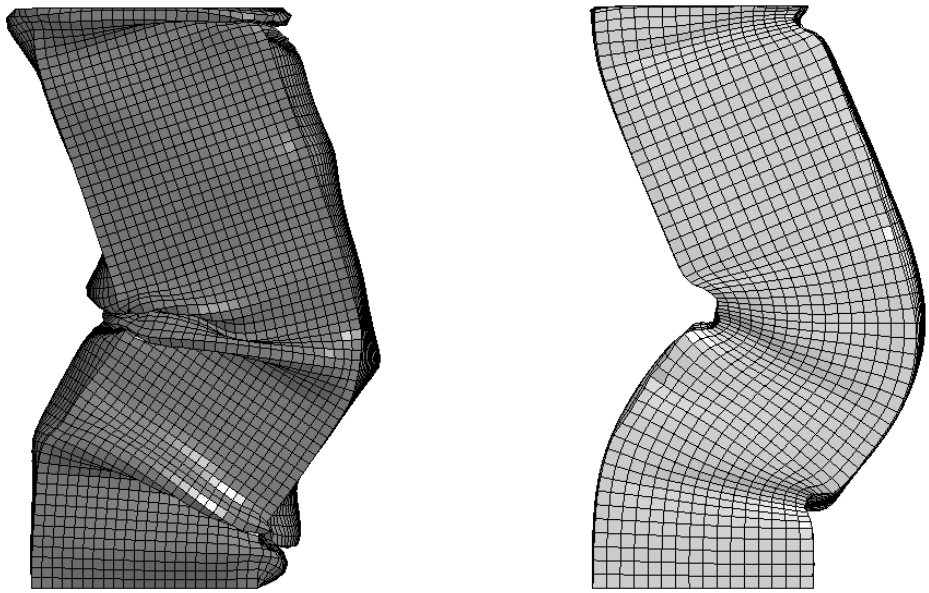

a. Deformed shape of column wall b. Deformed shape of foam

FIGURE 5.16: Deformed shapes of the FE simulation using MAT 154

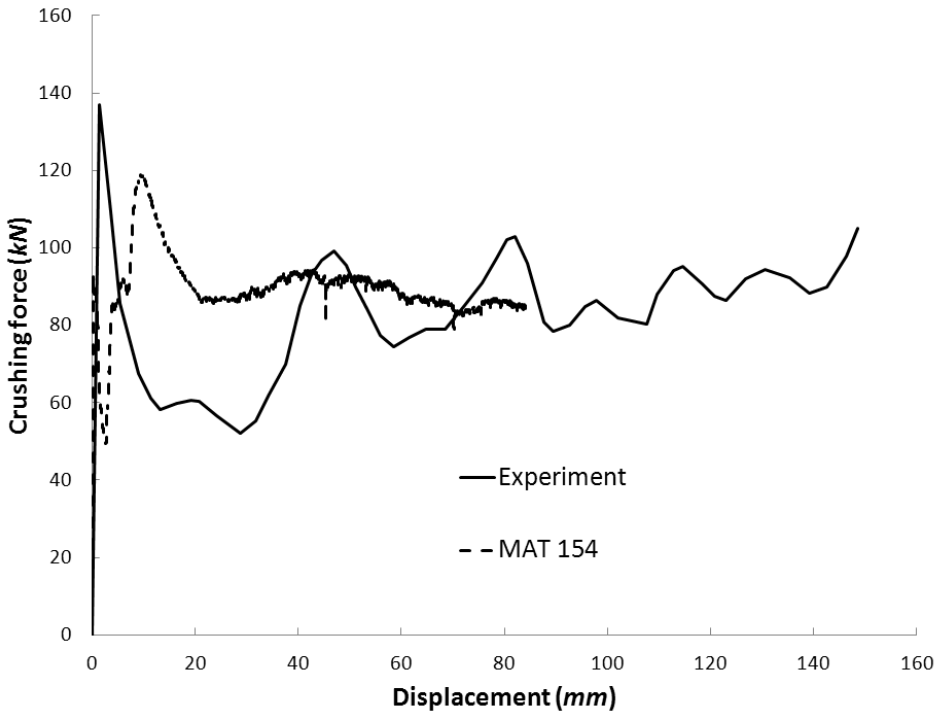

FIGURE 5.17: Force-displacement curves: MAT 154 vs. experimental results

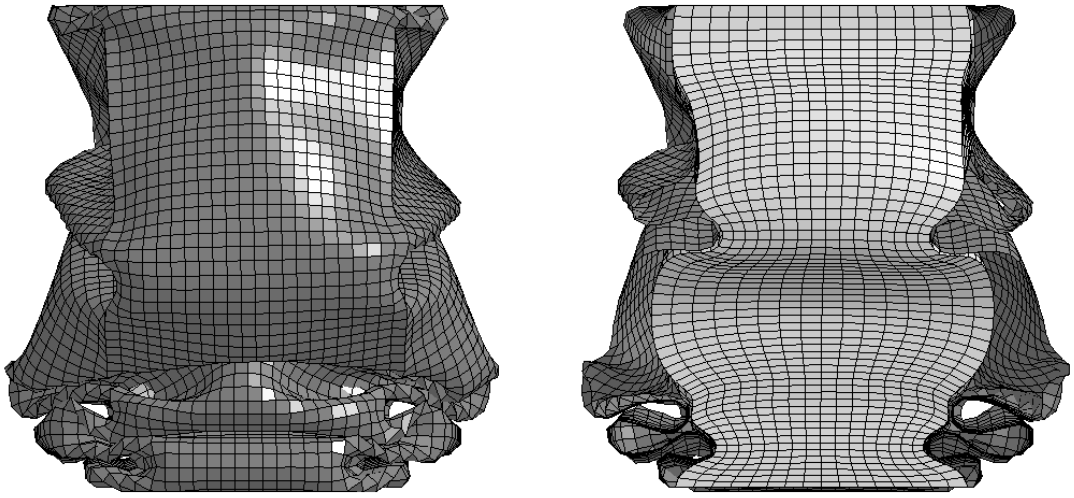

a. Deformed shape of tube b. Cross-section view of deformed foam and tube

FIGURE 5.18: Deformed shapes of the FE simulation using linear interpolation model

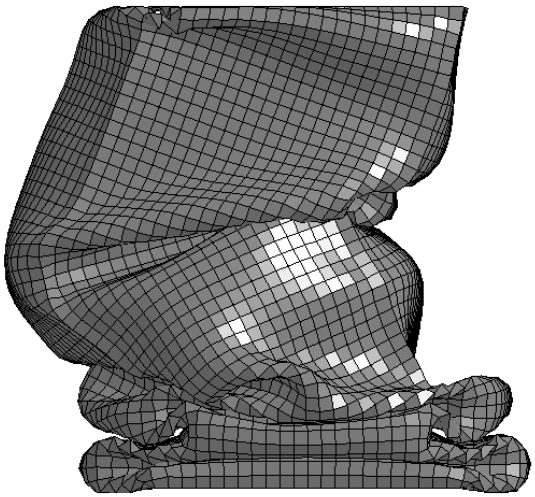

FIGURE 5.19: Global buckling mode of the square column

The crushing force history of the FE simulation using the linear interpolation function was compared to results using the exponential model and experiment data, as shown in FIGURE 5.20. The simplified linear interpolation model provided a similar prediction on crushing forces to that of the more precise exponential model. The first peak load was predicted to be 145 *kN* (same as the value obtained from the exponential model), while the experiment data showed the peak load to be 137 *kN*. The first peak load was captured in the FE simulation with an error less than 6%. The occurrence of the first peak in the simulation was 0.1 seconds before the peak load in the experiment. This could be due to imperfections in the experimental specimen that caused local plastic deformations during testing.

A mismatch of the resultant crushing force was found at displacements of 40 *mm* and 70 *mm*. This could be due to the occurrence of the global buckling. However, the MCF was captured well. The MCF obtained from the FE simulation was 86.50 *kN*. This

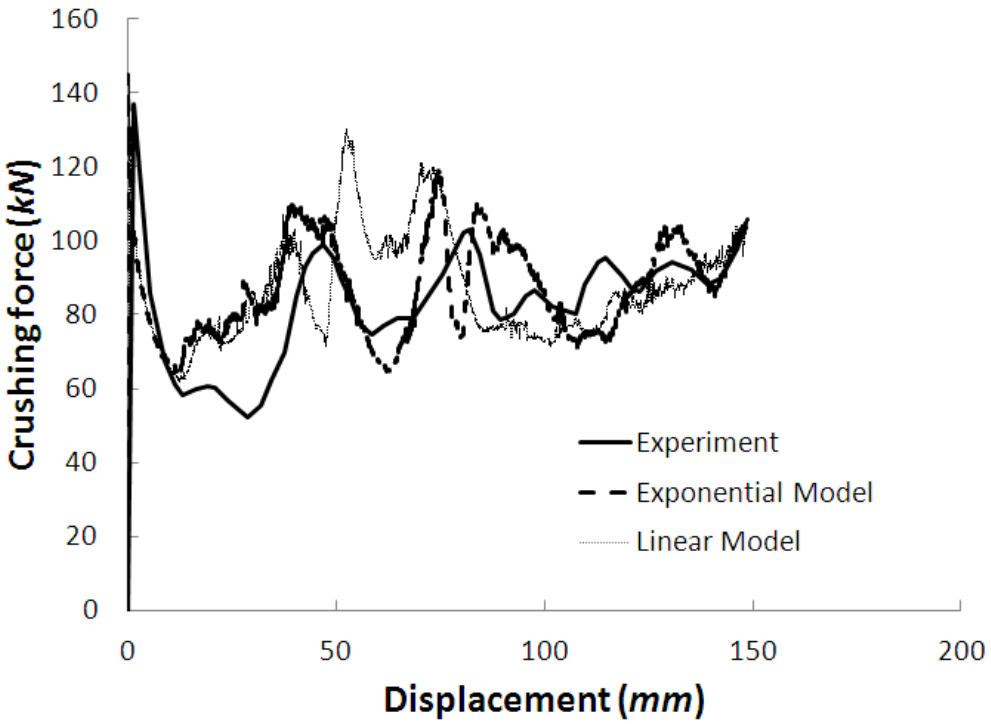

FIGURE 5.20: Force-displacement curves: new foam models vs. experimental results

represents a 1% error compared to the closed form solution of 87.04 *kN* and a 5.88% error compared to the experimental data of 81.70 *kN*.

5.3.2 Hexagonal column filled with foam

As shown in the case of the square column, the new foam model, particularly the one with exponential plastic Poisson's ratio, provides the most stable and accurate solutions for crash simulations compared to the LS-DYNA's built-in material models. In this section the new foam model is used to simulate crushing of a hexagonal foam-filled column.

FIGURE 5.21 shows the deformed shape of the hexagonal column with the symmetric/extensional folding mode. This can be identified from the more pronounced oscillations in the crushing force curve shown in FIGURE 5.22. In the

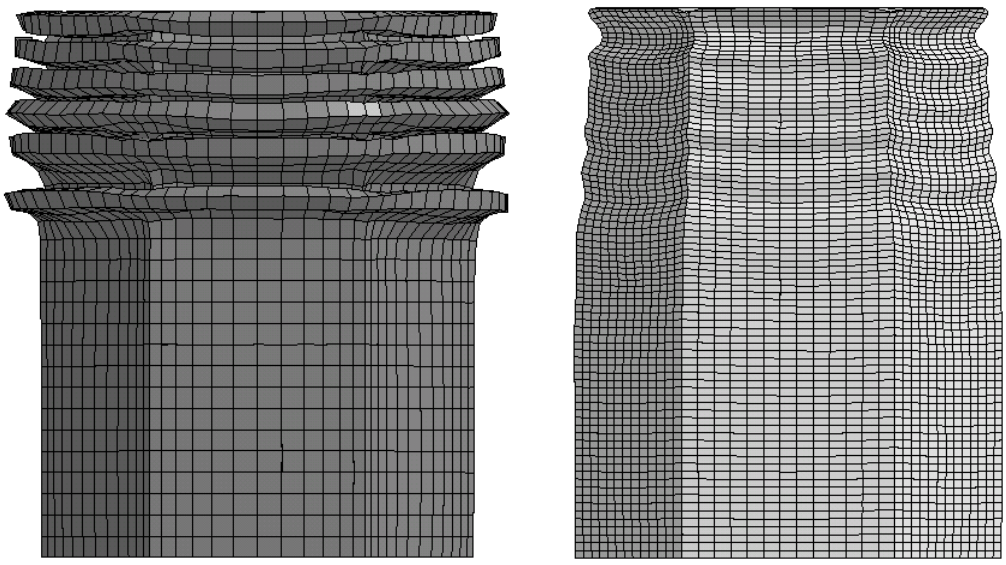

a. Deformed shape of column wall b. Deformed shape of foam

FIGURE 5.21: Deformed shapes of the FE simulation using the new foam model

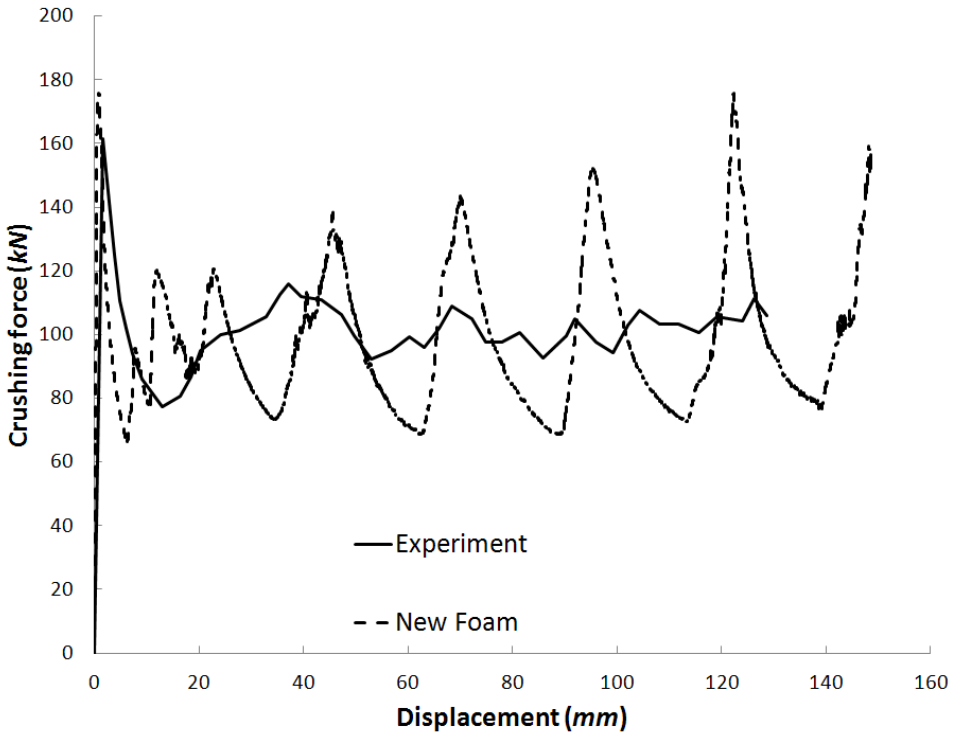

FIGURE 5.22: Force-displacement curves: new foam model vs. experimental results

experiment, however, the asymmetric folding was observed to be the dominant deformation mode and thus resulted in a relatively flat crushing force curve. This is due to the lower horizontal strength of the column wall when asymmetric folding occurs (Seitzberger et al. 2000).

It can be seen from FIGURE 5.21 that the foam was pushed towards the center of the column. No foam extended into the folds formed by the column wall, likely due to the more complex geometry of the cross-section. As mentioned in the work of Seitzberger et al. (2000), more symmetric folding modes were observed in experiments when the cross-sectional geometry became more complicated. For example, asymmetric folding modes were observed for all the tested square columns, but symmetric folding modes were observed for all the tested octagonal columns. The tested hexagonal column, which is the same one as that studied in this work, deformed in an asymmetric manner induced/triggered by material imperfections in the specimen. However, since no triggering mechanism was used in the FE simulation conducted for this dissertation, a symmetric folding mode was obtained.

FIGURE 5.22 shows the crushing force history of the hexagonal column. The experimental data was unavailable beyond 125 *mm* crushing distance. The first peak load in the FE simulation was found to be 175 *kN*; this represented an 8% error compared to the experimental measurement of 162.00 *kN*. Due to the symmetric folding mode in the simulation, the subsequent crushing forces in the simulation exhibited larger fluctuations than those observed in the experiment. However, the mean value of the fluctuating forces in the simulation was similar to the mean value of the experimental curve. The MCF was found to be 99 *kN* in the FE simulation. This is only a 2% error when

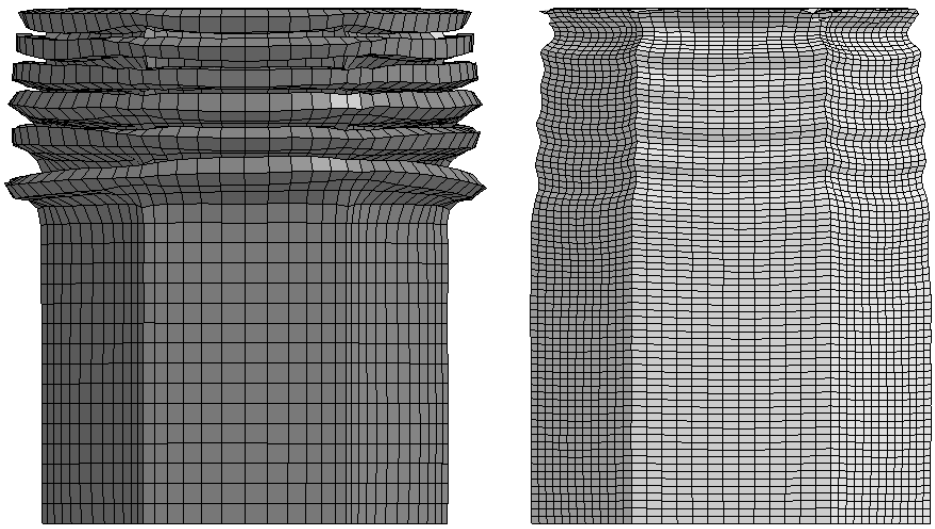

a. Deformed column wall b. Deformed foam

FIGURE 5.23: Deformed shapes of the FE simulation using linear interpolation model

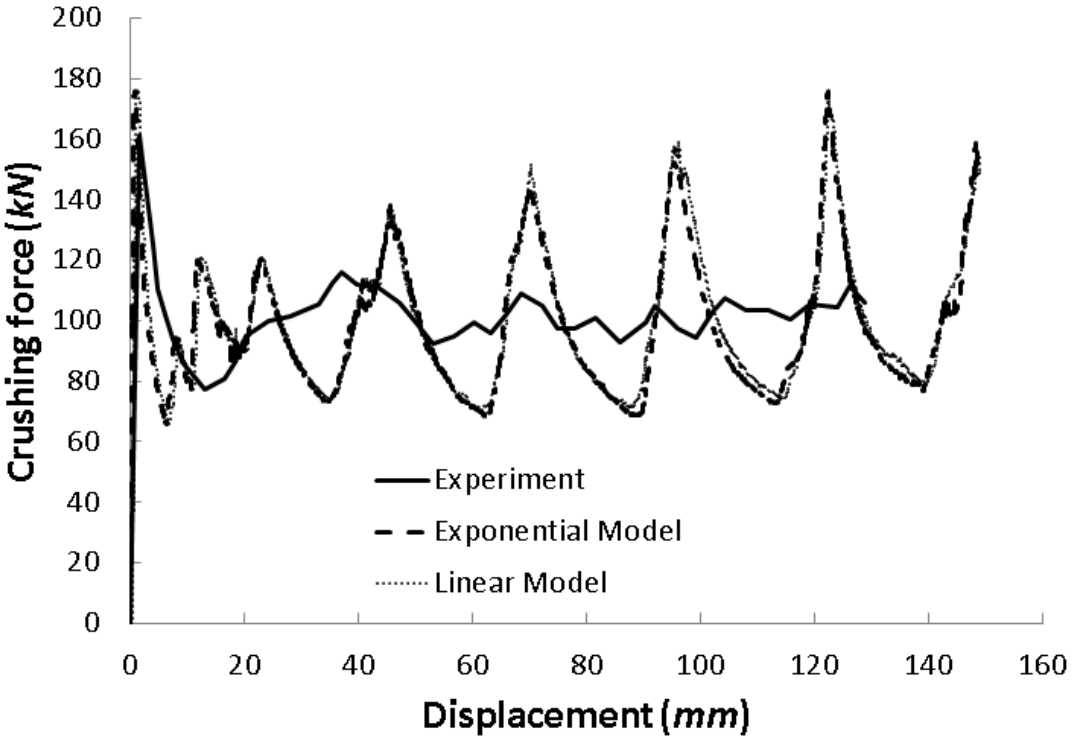

FIGURE 5.24: Force-displacement curves: new foam models vs. experimental results

compared to the experimental value of 101.20 *kN* and also a 2% error when compared to the closed form solution of 100.79 *kN*.

The foam model using a linear interpolation function for the plastic Poisson's ratio was also tested using the hexagonal column. FIGURE 5.23 shows the deformed shapes of the column from FE simulation using the linear model. It can be seen from FIGURE 5.23 that the foam was pushed towards the center of the column, similar to the results using the exponential model. In addition, the symmetric/extensional folding mode was also observed. This can be explained by the pronounced oscillations in the crushing force history, as shown in FIGURE 5.24. For the hexagonal column, the first peak load from the FE simulation was found to be 176 *kN*, giving a 9% error compared to the experimental measurement of 162 *kN*. The subsequent crushing forces were very similar to those from the exponential model; and the mean value of the fluctuating forces in the simulation was similar to the mean value calculated using experimental data. The MCF was found to be 99.56 *kN* in the FE simulation. This only gives a 2% error when compared to the experimental value of 101.20 *kN* and a 1% error when compared to the closed form solution of 100.79 *kN*.

CHAPTER 6: CONCLUSIONS

In this dissertation, a new constitutive model for metallic foams was developed to improve the accuracy and numerical stability of crash simulations. Metallic foams are porous materials that are commonly used in crashworthiness designs to increase energy absorption; however, they are difficult to model in numerical simulations such as finite element (FE) analysis. In the commercial FE code LS-DYNA, six material models (MAT 5, 26, 63, 75, 154, and 193) can be used to model foams, but none of them adequately captures the pressure-dependency and compressibility of foams. For example, MAT 75 considers pressure dependency, but the compressibility of the foam was not included. Although MAT 154 has a parameter for the material's compressibility, it does not allow for the change of this parameter with the progress of plastic deformations.

In the new constitutive model developed in this dissertation, both pressure-dependency and compressibility of the metallic foam were accounted for and related to material deformations. To achieve this, a yield function was defined to include both the von Mises stress and the hydrostatic pressure. To dynamically change the foam's compressibility based on deformation, the plastic Poisson's ratio was taken to be an exponential function of the strain so as to reduce the compressibility with increased material densification. A simplified linear function of strains was also tested for the plastic Poisson's ratio in an effort of reducing the computational time while maintain accuracy. In the new foam model the constitutive equations are solved implicitly using

the backward Euler integration method to ensure numerical stability and accuracy of the model.

The new foam model was implemented in LS-DYNA as a material subroutine and verified using a one-element model to confirm its correctness and convergence. In the two test cases, one with a nearly incompressible foam (plastic Poisson's ratio $\nu^p \approx 0.5$) and the other with a fully compressible foam (plastic Poisson's ratio $\nu^p = 0$), the element was compressed by an axial displacement of 54 *mm*. The simulation results showed that the new model could adequately capture the foam's compressibility: exhibiting a large transverse expansion for nearly incompressible foams and no transverse expansion for fully compressible foams. The new foam model was compared to LS-DYNA MAT 154 using a constant plastic Poisson's ratio. The results of both models matched well on normal stresses, effective plastic strains, hydrostatic pressures, and von Mises stresses.

To validate the new constitutive model, simulations of a uniaxial loading and a diagonal loading test of a cubical foam specimen were performed. The simulation results were compared to experimental measurements of force-displacement history and were shown to match the experimental data. It was observed that the largest discrepancy occurred on the high-density foam under uniaxial loading. This could be due to the fact that the new foam model did not capture fracture of foam cells that were observed in the experiments. Simulations of these two tests were also performed using four LS-DYNA's built-in foam models (MAT 5, 63, 75, and 154) to compare with the new model. Simulations with these four models were either numerically unstable or produced results that did not match the experimental data.

The new foam model was also compared to four LS-DYNA models using quasi-

static crushing tests of foam-filled, thin-walled columns with square and hexagonal cross-sections. For the square columns, the FE simulation using the new foam model was stable and the crushed tube showed progressive folding patterns. The aluminum foam acted as a foundation and increased the crushing forces of the column compared to a non-filled column, as observed in experiments. The time history of the crushing force from the simulation was found to match the experimental data. For example, the first peak crushing force from the simulation was 145 *kN*, which was 5.84% higher than the experimental measurement (137 *kN*). The mean crushing force was found to be 87.50 *kN* for the simulation, which was comparable to the experimental result (81.70 *kN*). The simulation using the linear model of the plastic Poisson's ratio exhibited global buckling deformation mode due to a higher rate of change of the shape factor then reality. The first peak crushing force was captured with an error of less than 6%. The mean crushing force was obtained at 86.50 *kN*, which was a 5.88% error relative to the experimental value (81.70 *kN*). For the same square column using LS-DYNA models (MAT 5, 63, 75 and 154), the simulations either converged very slowly on solving the constitutive equations or encountered premature terminations due to numerical instabilities, such as negative volumes or out-of-range velocities for highly compressed elements of the foam. In addition, the crushing forces and/or folding patterns from these simulations did not match well with experimental measurements.

For the hexagonal column, the FE simulation using the new foam model was stable, and the crushed tube showed progressive folding patterns. The aluminum foam acted as a foundation and increased the crushing forces of the column compared to a non-filled hexagonal column, as observed in experiments. The first peak crushing force from

the simulation was 175 *kN*, which was 8% higher than the experimental measurement (162 *kN*). The time history of the simulation crushing force was found to exhibit stronger fluctuations than in the experimental time history due to the symmetric folding mode in the simulation. The difference of the folding modes of the experiment versus the simulation (and thus crushing forces) could be due to the lack of a proper triggering mechanism in the FE simulation and the complicated geometry of the hexagonal cross-section. However, the mean crushing force was found to be 99 *kN* from the simulation, which was comparable to the experimental result (101.20 *kN*). The simulation using the linear model of the plastic Poisson's ratio exhibited similar folding patterns compared to those using the exponential model. The first peak force was found at 176 *kN*, which was a 9% error relative to the experimental result. The mean crushing force was captured with 2% error when compared to the experimental value (101.20 *kN*).

In summary, the new constitutive model for metallic foams developed in this dissertation was shown to outperform existing models implemented in the commercial FE code, LS-DYNA. This is mainly attributed to the consideration of both hydrostatic pressure and von Mises stress during the entire process of plastic deformation. The method of dynamically changing the foam's compressibility based on its plastic deformation was not found in any of the existing LS-DYNA foam models. The FE simulations using the new foam model were found to be stable and efficient, even for large deformations at a crushing distance of 60% of the original column length. For future investigations, element failures, (i.e., fractures of the foam cells), should be considered and incorporated into the foam model to reduce the small discrepancy between the current model and the experimental results.

REFERENCES

Abaqus (2007). *Abaqus 6.7 User Documentation*, Dassault Systèmes, Lowell, MA.

Abramowicz, W., and Jones, N. (1984). "Dynamic axial crushing of square columns." *International Journal of Impact Engineering,* 2(2), 179-208.

Abramowicz, W., and Wierzbicki, T. (1989). "Axial crushing of multicorner sheet metal columns." *Journal of Applied Mechanics,* 56(1), 113-120.

Allen, P. A. (2000). "Hydrostatic stress effects in metal plasticity." Master's Thesis, Tennessee Technological University.

Allen, P. A. (2002). "Hydrostatic stress effects in low cycle fatigue." Doctoral Dissertation, Tennessee Technological University.

Allen, P. A. and Wilson, C. D. (2004). "Development of a pressure-dependent constitutive model with combined multilinear kinematic and isotropic hardening." *2004 Abaqus Users' Conference*, Boston MA.

Alexander, J. M. (1960). "An approximate analysis of the collapse of thin cylindrical shells under axial loading." *The Quarterly Journal of Mechanics and Applied Mathematics,* 13(1), 10-15.

ANSYS (2004). *ANSYS, Inc. Theory Reference*, ANSYS Release 9.0, ANSYS, Inc. Southpointe, PA.

Aravas, N. (1987). "On the numerical integration of a class of pressure-dependent plasticity models." *International Journal for Numerical Methods in Engineering*, 24(7), 1395-1416.

Argyris, J., Balmer, H. A., Doltsinis, J. S., and Kurz, A. (1986). "Computer simulation of crash phenomena." *International Journal for Numerical Methods in Engineering*, 22(3), 497-519.

Avalle, M., Chiandussi, G., and Belingardi, G. (2002). "Design optimization by response surface methodology: Application to crashworthiness design of vehicle structures." *Structural and Multidisciplinary Optimization,* 24(4), 325-332.

Banhart, J. (2001). "Manufacture, characterisation and application of cellular metals and metal foams." *Progress in Material Science,* 46(6), 559-632.

Baumeister, J., Banhart, J. and Weber, M. (1997). "Aluminium foams for transport industry." *Materials and Design*, 18(4-6), 217-220.

Bi, J., Fang, H., Wang, Q., and Ren, X. (2010a). "Modeling and optimization of foam-filled thin-walled columns for crashworthiness designs." *Finite Elements in Analysis and Design*, 46(9), 398-709.

Bi, J., Fang, H., and Weggel, D. C. (2010b). "Finite element modelling of cable median barriers under vehicular impacts." *11th International Conference on Structures Under Shock and Impact*, July 28-30, 2010, Tallinn, Estonia.

Borovinsek, M., Vasenjak, M., Ulbin, M., and Ren, Z. (2007). "Simulation of crash tests for high containment levels of road safety barriers." *Engineering Failure Analysis*, 14(8), 1711-1718.

Bridgman, P. W. (1947). "The effect of hydrostatic pressure on the fracture of brittle substances." *Journal of Applied Physics*, 18(2), 246-258.

Chen, W. (2001). "Crashworthiness optimization of ultralight metal structures." PhD dissertation, February, 2001, Massachusetts Institutive of Technology, Cambridge MA.

Chen, W., and Wierzbicki, T. (2001). "Relative merits of single-celled, multi-cell and foam-filled thin-walled structures in energy absorption." *Thin-walled Structures,* 39(4), 287-306.

Chu, C. C., and Needleman, A. (1980). "Void nucleation effects in biaxially stretched sheets." *Journal of Engineering Materials and Technology-Transactions of the ASME*, 102(3), 249-256.

Cunat, P. J. (2000). "Stainless steel properties for structural automotive applications." *Metal Bulletin-International Automotive Materials Conference*, June 21-23, Cologne.

Daxner, T., Bohm, H. J., and Rammerstorfer, F. G. (1999). "Mesoscopic simulation of inhomogeneous metallic foams with respect to energy absorption." *Computational Materials Science*, 16(1-4), 61-69.

Deshpande, V. S., and Fleck, N. A. (2000). "Isotropic constitutive models for metallic foams." *Journal of the Mechanics and Physics of Solids*, 48(6-7), 1253-1283.

Drucker, D. C. and Prager, W. (1952). "Soil mechanics and plastic analysis or limit design." *Quarterly of Applied Mathematics*, 10(2), 157-165.

Dunne, F. and Petrinic, N. (2005). *Introduction to Computational Plasticity*. Oxford University Press.

Eby, D. J., Averill, R. C., Goodman, E. D., and Sidhu, R. S. (2002). "Shape optimization of crashworthy structures." *The 7th International LS-DYNA Users Conference*.

Elmarakbi, A., Sennah, K., Samaan, M., and Siriya, P. (2006). "Crashworthiness of motor vehicle and traffic light pole in frontal collisions." *Journal of Transportation Engineering - ASCE*, 132(9), 722-733.

El-Tawil, S., Severino, E., and Fonseca, P. (2005). "Vehicle collision with bridge piers." *Journal of Bridge Engineering*, 10(3), 345-353.

ESI (2008). *PAM-CRASH Solver Notes*, 2008, ESI Group.

Fang, H., Rais-Rohani, M., Liu, Z., and Horstemeyer, M. F. (2005a). "A comparative study of metamodeling methods for multi-objective crashworthiness optimization." *Composite Structures,* 83(25-26), 2121-2136.

Fang, H., Solanki, K., and Horstemeyer, M. F. (2005b). "Numerical simulations of multiple vehicle crashes and multidisciplinary crashworthiness optimization." *International Journal of Crashworthiness*, 10(2), 161-171.

FMVSS (1998). *Federal Motor Vehicle Safety Standard No. 208*, Occupant Crash Protection, Code of Federal Regulations, Title 49, Part 571, S208, Washington D. C.

Gassan. J. and Harwick, W. (2001). "Behavior of aluminum foams under quasi-static and crash loadings." *Journal of Material Science Letters*, 20(11), 1047-1048.

Gibson, L. J., Ashby, M. F., Zhang, J., and Triantafillou, T. C. (1989). "Failure surfaces for cellular materials under multiaxial loads. 1. modeling." *International Journal of Mechanical Sciences*, 31(9), 635-663.

Gradinger, R., and Rammerstorfer, F. G. (1998). "On the influence of meso-inhomogeneities on the crush worthiness of metal foams." *Acta Materialia*, 47(1), 143-148.

Greaves, G. N., Greer, A. L., Lakes, R. S., and Rouxel, T. (2011). "Poisson's ratio and modern materials." *Nature Materials*, 10(11), 823-837.

Gursel, K. T., and Nane, S. N. (2010). "Non-linear finite element analyses of automobiles and their elements in crashes." *International Journal of Crashworthiness*, 15(6), 667-692.

Gurson, A. L. (1977). "Continuum theory of ductile rupture by void nucleation and growth. 1. Yield criteria and flow rules for porous ductile media." *Journal of Engineering Materials and Technology-Transactions of the ASME*, 99(1), 2-15.

Hallquist, J. O. (2006). *LS-DYNA Theory Manual*. Livermore Software Technology Corporation, Livermore, CA.

Hanssen, A. G., Hopperstad, O. S., Langseth, M., and Ilstad, H. (2002). "Validation of constitutive models applicable to aluminium foams." *International Journal of Mechanical Sciences*, 44(2), 359-406.

Haug, E., Arnadeau, F., Dubois, J., and Rouvray, A. (1983). "Static and dynamic finite element analysis of structural crashworthiness in the automotive and aerospace industries." *Structural Crashworthiness* - N. Jones, T. Wierzbicki, Butterworths Publisher, 175-218.

Hill, R. (1950). *The Mathematical Theory of Plasticity*. Clarendon Press, Oxford.

Hou, S., Li, Q., Long, S., Yang, X., and Li, W. (2007). "Design optimization of regular hexagonal thin-walled columns with crashworthiness criteria." *Finite Elements in Analysis and Design,* 43(6-7), 555-565.

Hou, S., Li, Q., Long, S., Yang, X., and Li, W. (2009). "Crashworthiness design for foam thin-wall structures." *Materials and Design,* 30(6), 2024-2032.

IIHS (2010). Insurance Institute for Highway Safety, Arlington, VA. www.iihs.org

Kanahashi, H., Mukai, T., Yamada, Y., Shimojima, K., Mabuchi, M., Nieh, T. G., and Higashi, K. (2000). "Dynamic compression of an ultra-low density aluminum foam." *Material Science and Engineering A,* 280, 349-353.

Kim, H. S., Chen, W., and Wierzbicki, T. (2002). "Weight and crash optimization of foam-filled three-dimensional ''S'' frame." *Computational Mechanics,* 28, 417-424.

Krieg, R. D. (1972). "A simple constitutive description for cellular concrete." Sandia National Laboratories, Albuquerque, NM, Rept. SC-DR-72-0883.

Kurtaran, H., Eskandarian, A., Kurtanran, H., Marzougui, D., and Bedewi, N. E. (2002). "Crashworthiness design optimization using successive response surface approximations." *Computational Mechanics,* 29(4), 409-421.

Lanzi, L., Castelletti, L. M. L., and Anghileri, M. (2004). "Multi-objective optimization of composite absorber shape under crashworthiness requirements." *Composite Structures,* 65(3-4), 433-441.

Laursen, T. A. (2003). *Computational Contact and Impact Mechanics,* Springer, New York, NY.

Lee, S. H., Kim, H. Y., and Oh, S. I. (2002). "Cylindrical column optimization using response surface method based on stochastic process." *Journal of Materials Processing Technology,* 130, 490-496.

Liu, Y. (2008). "Crashworthiness design of multi-corner thin-walled columns." *Thin-walled Structures,* 46(12), 1329-1337.

Lopatnikov, S. L., Gama, B. A., Haque, M. J., Krauthauser, C., and Gillespie, J. W. Jr. (2004). "High-velocity plate impact of metal foams." *International Journal of Impact Engineering,* 30(4), 421-445.

Lopatnikov, S. L., Gama, B. A., Haque, M. J., Krauthauser, C., Gillespie, J. W. Jr., Guden, M., and Hall, I. W. (2003). "Dynamics of metal foam deformation during Taylor cylinder-Hopkinson bar impact experiment." *Composite Structures,* 61(1-2), 61-71.

LSTC (2010). *LS-DYNA Keyword User's Manual, Volume I, Version 971 / Rev 5 (Beta)*. Livermore Software Technology Corporation, Livermore, CA.

Mamalis, A. G., Manolakos, D. E., Loannidis, M. B., Spentzas, K. N., and Koutroubakis, S. (2008). "Static axial collapse of foam-filled steel thin-walled rectangular tubes: experimental and numerical simulation." *International Journal of Crashworthiness,* 13(2), 117-126.

Mao, M., Chirwa, E. C., Chen, T., Latchford, J., and Wang, W. (2005). "Numerical analysis of a small European vehicle under rollover condition." *Proceedings of the Institution of Mechanical Engineers Part D - Journal of Automobile Engineering*, 219(D12), 1369-1379.

Meguid, S. A., Cheon, S. S., and El-Abbasi, N. (2002). "FE modelling of deformation localization in metallic foams." *Finite Elements in Analysis and Design*, 38(7), 631-643.

Miller, R. E. (2000). "A continuum plasticity model for constitutive and indentation behaviour of foamed metals." *International Journal for Mechanical Sciences*, 42(4), 729-754.

Miyoshi, T., Itoh, M., Mukai, T., Kanahashi, H., Kohzu, H., Tanabe, S., and Higashi, K. (1999). "Enhancement of energy absorption in a closed-cell aluminum by the modification of cellular structures." *Scripta Materialia,* 41(10), 1055-1060.

Monchiet, V., Cazacu, O., Charkaluk, E., and Kondo, D. (2008). "Macroscopic yield criteria for plastic anisotropic materials containing spheroidal voids." *International Journal of Plasticity*, 24(7), 1158-1189.

MSC (2004). *Nastran Reference Manual*, MSC Software Corporation, Santa Ana, CA.

Muhlich, U. and Brocks W. (2003). "On the numerical integration of a class of pressure-dependent plasticity models including kinematic hardening." *Computational Mechanics*, 31(6), 479-488.

Nagtegaal, J. C. and De Jong, J. E. (1981). "Some computational aspects of elastic-plastic large strain analysis." *International Journal for Numerical Methods in Engineering*, 17(1), 15-41.

NCAC (2008). "Finite element model of Ford Taurus." Version 3, National Crash Analysis Center, Ashburn, VA.

NHTSA (2006). *NHTSA Test Reference Guides, 5th version*. National Highway Traffic Safety Administration, Washington D.C.

Paul, A. and Ramamurty, U. (2000). "Strain rate sensitivity of a closed-cell aluminum foam." *Material Science and Engineering A,* 281(1-2), 1-7.

Pifko, A. B., and Winter, R. (1981). "Theory and application of finite element analysis to structural crash simulation." *Computers and Structures*, 13(1-3), 277-285.

Rabbani, K., Daniels, M., Walker, N., and Shirvani, B. (2009). "Material behavior modelling for finite element vehicle crash simulation." *Key Engineering Materials*, 410-411, 521-532.

Ragab, A. R., and Saleh, C. A. R. (1999). "Evaluation of constitutive models for voided solids." *International Journal of Plasticity*, 15(10), 1041-1065.

Redhe, M., Giger, M., and Nilsson, L. (2004). "An investigation of structural optimization in crashworthiness design using a stochastic approach." *Structural and Multidisciplinary Optimization*, 27(6), 446-459.

Reyes, A., Hopperstad, O. S., Berstad T. and Langseth M. (2004). "Implementation of a constitutive model for aluminum foam including fracture and statistical variation of density." *8th International LS-DYNA Users Conference*, Detroit, MI.

Richmond, O. and Spitzig, W. A. (1980). "Pressure dependence and dilatancy of plastic flow." *Theoretical and Applied Mechanics; Proceedings of the Fifteenth International Congress*, Toronto, Canada.

Santosa, S. P., Wierzbicki, T., Hanssen, A. G., and Langseth, M. (2000). "Experimental and numerical studies of foam-filled sections." *International Journal of Impact Engineering,* 24(5), 509-534.

Schreyer, H. L., Zuo, Q. H., and Maji, A. K. (1994). "Anisotropic plasticity model for foams and honeycombs." *Journal of Engineering Mechanics - ASCE*, 120(9), 1913-1930.

Seitzberger, M., Rammerstorfer, F. G., Gradinger, R., Degischer, H. P., Blaimschein, M. and Walch, C. (2000). "Experimental studies on the quasi-static axial crushing of steel columns filled with aluminium foam." *International Journal of Solids and Structures*, 37(30), 4125-4147.

Shaw, M.C. and Sata T. (1966). "The plastic behavior of cellular materials." *International Journal of Mechanical Sciences*, 8(7), 469-472.

Simo, J. C., and Ortiz, M. (1985). "A unified approach to finite deformation elastoplastic analysis based on the use of hyperelastic constitutive-equqations." *Computer Methods in Applied Mechanics and Engineering*, 49(2), 221-245.

Song, H. W., Fan, Z. J., Yu, G., Wang, Q. C., and Tobota, A. (2005). "Partition energy absorption of axially crushed aluminum foam-filled hat sections." *International Journal of Solids and Structures,* 42(9-10), 2575-2600.

Spitzig, W. A., Sober, R. J. and Richmond O. (1975). "Pressure dependence of yielding and associated volume expansion in tempered martensite." *Acta Metallurgica*, 23(7), 885-893.

Spitzig, W. A., Sober, R. J. and Richmond O. (1976). "The effect of hydrostatic pressure on the deformation behavior of maraging and HY-80 steels and its implications for plasticity theory." *Metallurgica Transactions A-Physical Metallurgy and Materials Science*, 7(11), 1703-1710.

Spitzig, W. A. and Richmond O. (1984). "The effect of pressure on the flow stress of metals." *Acta Metallurgica*, 32(3), 457-463.

Tan, P. J., Reid, S. R., Harrigan, J. J., Zou, Z., and Li, S. (2005a). "Dynamic compressive strength properties of aluminum foams. Part I - experimental data and observations." *Journal of the Mechanics and Physics of Solids,* 53(10), 2174-2205.

Tan, P. J., Reid, S. R., Harrigan, J. J., Zou, Z., and Li, S. (2005b). "Dynamic compressive strength properties of aluminum foams. Part II - 'shock' theory and comparison with experimental data and numerical models." *Journal of the Mechanics and Physics of Solids,* 53(10), 2206-2230.

Thacker, J. G., Reagan, S. W., Pellettiere, J. A., Pilkey, W. D., Crandall, J. R., and Sieveka, E. M. (1998). "Experiences during development of a dynamic crash response automobile model." *Finite Elements in Analysis and Design*, 30(4), 279-295.

Triantafillou, T. C., and Gibson, L. J. (1990). "Constitutive modeling of elastic-plastic open-cell foams." *Journal of Engineering Mechanics-ASCE*, 116(12), 2772-2776.

Tvergaard, V., and Needleman, A. (1984). "Analysis of the cup-cone fracture in a round tensile bar." *Acta Metallurgica*, 32(1), 157-169.

Ulker, M. B. C., and Rahman, M. S. (2008). "Traffic barriers under vehicular impact: from computer simulation to design guidelines." *Computer-Aided Civil and Infrastructure Engineering,* 23(6), 465-480.

Wen, J., Huang, Y., Hwang, K. C., Liu, C., and Li, M. (2005). "The modified Gurson model accounting for the void size effect." *International Journal of Plasticity*, 21(2), 381-395.

Wierzbicki, T., and Abramowicz, W. (1983). "On the crushing mechanics of thin-walled structures." *Journal of Applied Mechanics*, 50(4a), 727-739.

Williams, T. D., de Pennington, A., and Barton, D. C. (2000). "Frontal impact response of a spaceframe chassis sportscar." *Proceedings of the Institution of Mechanical Engineers Part D - Journal of Automobile Engineering*, 214(8), 865-873.

Wilson, C. D. (2002). "A critical reexamination of classical metal plasticity." *Journal of Applied Mechanics – Transactions of the ASME*, 69(1), 63-68.

White, M. D., and Jones, N. (1999). "Experimental quasi-static axial crushing of tophat and double-hat thin-walled sections." *International Journal of Mechanical Sciences,* 41(2), 179-208.

Xiang, Y., Wang, Q., Fan, Z., and Fang, H. (2006). "Optimal crashworthiness design of a spot-welded thin-walled hat section." *Finite Elements in Analysis and Design,* 42(10), 846-855.

Yamazaki, K., and Han, J. (1998). "Maximization of the crushing energy absorption of columns." *Structural and Multidisciplinary Optimization,* 16(1), 37-46.

Yamazaki, K., and Han, J. (2000). "Maximization of the crushing energy absorption of cylindrical shells." *Advances in Engineering Software,* 31(6), 425-432.

Zarei, H. R., and Kroger, M. (2008a). "Bending behavior of empty and foam-filled beams: Structural optimization." *International Journal of Impact Engineering,* 35(6), 521-529.

Zarei, H. R., and Kroger, M. (2008b). "Optimization of the foam-filled aluminum tubes for crush box application." *Thin-walled Structures,* 46(2), 214-221.

Zhao, H., and Abdennadher, S. (2004). "On the strength enhancement under impact loading of square tubes made from rate insensitive metals." *International Journal of Solids and Structures,* 41(24-25), 6677-6697.

Zhang, J., Lin, Z., and Wong, A. (1997). "Constitutive modeling and material characterization of polymeric foams." *Journal of Engineering Materials and Technology - Transactions of the ASME*, 119(3), 284-291.

Zhang, X., Cheng, G., Wang, B., and Zhang, H. (2008). "Optimum design for energy absorption of bitubal hexagonal columns with honeycomb core." *International Journal of Crashworthiness,* 13(1), 99-107.

Zhang, Z. L. (1994). "Explicit consistent tangent moduli with a return mapping algorithm for pressure-dependent elastoplasticity models." *Computer Methods in Applied Mechanics and Engineering*, 121(1-4), 29-44.

APPENDIX A: MAKEFILE FOR BUILDING LS-DYNA DYNAMIC LIBRARY

```
# Makefile for building mpp971 dynamic lib
#
MODEL = NF
OBJS = $(MODEL).o dyn21.o dyn21b.o
OPTIONS = -c -w95 -W0 -zero -safe_cray_ptr -assume byterecl,buffered_io -
mP2OPT_hlo_fusion = F -save -traceback -save -pad -nodps -DLINUX -
DNET_SECURITY -DADDR64 -DINTEL -DXEON64 -DFCC80 -DMPP -DMPICH -
DHPMPI -DAUTODOUBLE -DNEWIO -i8 -r8 -xW -fpic  -O2 -I.
mpp971: $(OBJS)
        mpif90 -shared -o libmpp971_d_7600.2.1224_usermat.so $(OBJS)
$(MODEL).o: $(MODEL).f
        mpif90 $(OPTIONS) $(MODEL).f
dyn21.o: dyn21.f
        mpif90 $(OPTIONS) dyn21.f
dyn21b.o: dyn21b.f
        mpif90 $(OPTIONS) dyn21b.f
#
# End of file
```